THE BELL SYSTEM TECHNICAL JOURNAL
Vol. 58, No. 6, July–August 1979
Printed in U.S.A.

Current-Access Magnetic Bubble Circuits

By A. H. BOBECK, S. L. BLANK, A. D. BUTHERUS, F. J. CIAK, and W. STRAUSS

(Manuscript received March 9, 1979)

Experimental and theoretical results from our work on current-access technology show promise for high-density, ~10^7 bits/cm^2, and high-frequency, $f > 1$ MHz, bubble devices. We have operated current-access devices where the bubble-driving fields derive from two patterned conducting sheets instead of orthogonal field coils. Margins for generation, propagation, and transfer were studied on 8-μm periods at 1 MHz. These 8-μm period structures typically required 1.5 mA/μm per conducting sheet and dissipated 14 μW/bit. Single conducting-sheet, current-access circuitry also propagates bubbles but offers less design flexibility. We present design criteria, magnetic field equations, and design curves. Implementation of these devices required new magnetic materials with quality factor Q comparable to available garnets, yet higher mobility and lower dynamic coercivity. Of the three systems, $(YLuSmCa)_3(FeGe)_5O_{12}$, $(LaLuSmCa)_3(FeGe)_5O_{12}$, *and* $(LaLuSm)_3(FeGa)_5O_{12}$, *the last appears best suited; some room temperature characteristics of the composition* $La_{0.6}Lu_{2.1}Sm_{0.3}Ga_{0.9}Fe_{4.1}O_{12}$ *are* $4\pi M_s = 470G$, $\mu = 750\ cmS^{-1}\text{-}Oe^{-1}$, $d = 1.6\ \mu m$, *and* $\Delta H_c = 2$ *Oe across a bubble for the threshold of motion. Necessary improvements in processing were made with a radio-frequency, chlorine-containing plasma etch which produced metal patterns identical to those of the etch mask. We anticipate that current-access devices, when compared to conventional field-access devices, will achieve higher data rates, lower power consumption per bit, and greater storage densities with existing processing technologies.*

I. INTRODUCTION

We have been investigating the potential of conductor-access bubble circuitry[1] to meet the need for a high-density, high-capacity, low-cost, nonvolatile memory device. There are two basic ways to move bubbles: field-access[2] and current-access (conductor-access). Field-access de-

vices, the only type in use at this time, require a pair of orthogonal drive coils to provide an in-plane magnetic field which, coupled to a bubble data stream via structured permalloy or ion-implanted features,[3] provides the necessary bubble drive forces.

It is difficult, however, to take advantage of the data rates intrinsic in field-access bubble devices as they are scaled down in size. In particular, the volt-ampere product increases with increasing frequency, making economical coil drive circuits difficult to design. Present field-access devices are limited to about a 250-kHz rotating field rate and are thus too slow for applications such as television frame storage. A bit rate per chip of 1 Mb/s or greater would make bubbles attractive to a wider range of potential customers.

In traditional current-access bubble circuitry, meandering conductor strips of relatively high resistance, rather than drive coils, make it possible to provide the necessary currents to move bubbles at stepping rates of 1 MHz and greater with relative ease but give rise to a concern that current-access chips would dissipate excessive power, especially at the higher bit storage densities such as 10^7 b/cm^2.

The disadvantage of the current-access circuits disclosed to date has been the complexity of the conductor patterns themselves. We have developed new configurations, however, that use rather simple apertured sheet geometries and which should dissipate less power as well. Bubble circuits with an 8-μm period, a four-times improvement in storage density over present circuits, are expected to be achieved while maintaining the same design rules of the 16-μm period field-access circuits now in manufacture at Western Electric, Reading.[4]

II. HISTORY OF CURRENT ACCESS DEVELOPMENT

It is not surprising that the very first experiments to control bubble movement used conductor drive. In these first experiments, adjacent posts of a "waffle-iron" ferrite base plate were looped by conductors as shown in Fig. 1.[1] Conductors ϕ_1, ϕ_2, and ϕ_3 driven by unipolar current pulses produced bubble motion with the direction determined by the pulse sequence. Bubble domains had to overlap from one post to another before proper operation could be obtained.

A continued evolution in circuit design next led to the single conductor design of Copeland et al.,[5] shown in Fig. 2. Note the conductor which meanders back and forth across a groove which has been etched into the surface of the epitaxial garnet layer. Undulations in the width of the groove define preferred bubble rest positions which supplement a bipolar current drive to produce bubble motion. It is a basic requirement of this design, however, that a rather precise geometrical fit be maintained between the bubble and the groove pattern. The ideal bubble diameter is, in fact, one-half of the conductor period making

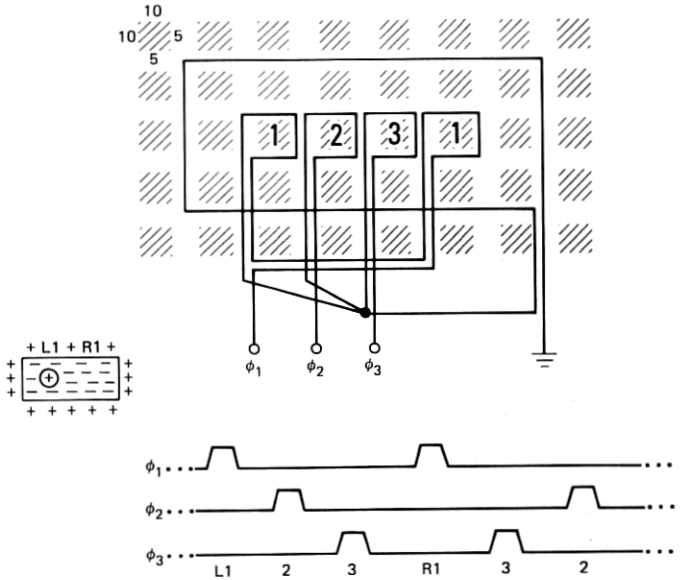

Fig. 1—Schematic of the first bubble shift register circuit. Bubbles in orthoferrites were moved three steps with a waffle-iron base plate.

bubble-to-bubble interactions prohibitive at the maximum storage density and hence the circuit could only be operated with data in every other position. A variation in which grooved tracks were replaced by ion-implanted tracks of similar shape was also operated.[3] About this time, effort in conductor propagation was terminated in favor of "field-access" propagation.

Conductor propagation re-emerged in 1974 when Walsh and Charap[6] proposed a perforated conducting sheet driven by either a rotating or oscillating current as a novel bubble drive. Their computer simulation indicated that operation comparable to that of field-access devices could be accomplished. Their paper went unnoticed.

In 1975, the bubble lattice storage device was announced by Voegeli et al.[7] Conductors were used to move bubbles in the main storage area, the entrance-exit line, and the detector. In the most recent paper on the bubble lattice, Hu et al.[8] state "Ironically, the "simple" shift register propagation of an isolated-bubble has one of the smallest margins in the chip." Hu et al. were somewhat handicapped in their design since bias field compatibility had to be maintained with the main storage area. Nonetheless, their report was not encouraging.

Then in 1977, Dekker et al.,[9] Phillips Research Labs, introduced a design which combined conductor and field access on a major-minor chip. They replaced the usually field-driven major track by a conductor-driven track that operated at a ten-times-higher stepping rate. In

this way, they achieved a fivefold reduction in access time. Typical of the Dekker designs is that illustrated in Fig. 3. The "conductor" is in reality a dual-layer, permalloy-gold sandwich in which the gold layer has been included to lower the sheet resistance and, consequently, the

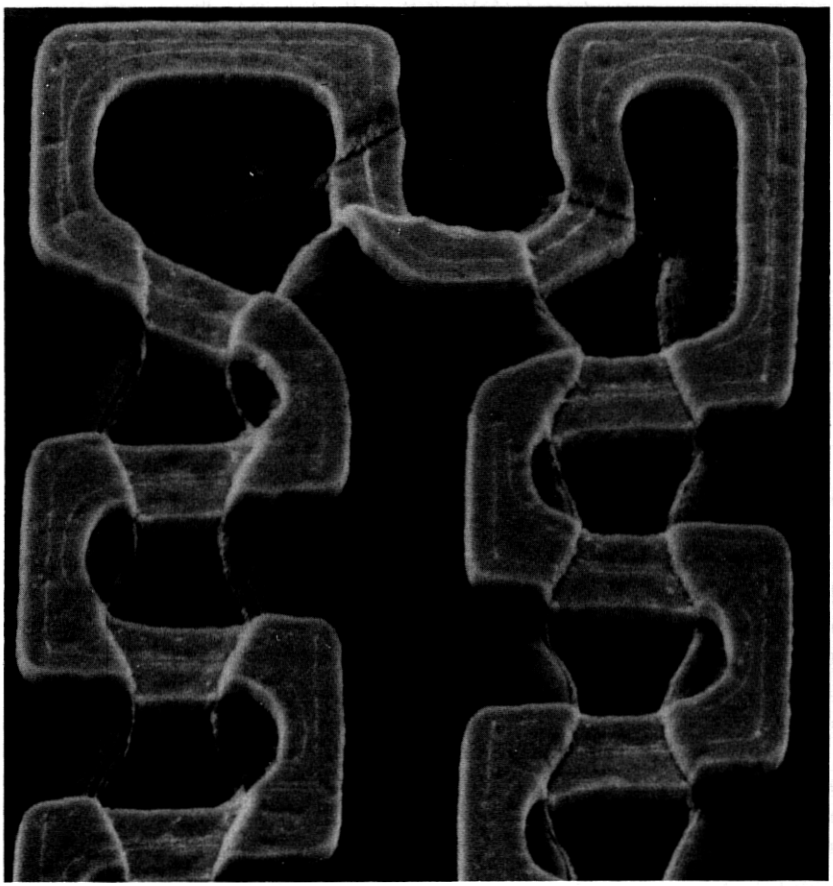

Fig. 2—An SEM of a turn of a conductor-groove circuit. The circuit period is 16 μm.

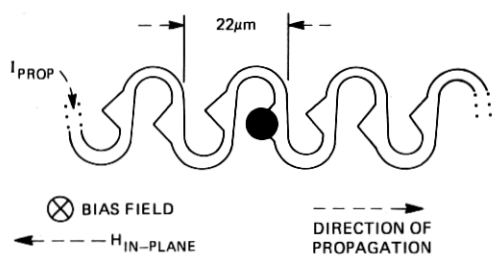

Fig. 3—A current-driven major track. An in-plane field generates poles at points of the "conductor," which is in reality a conductor-permalloy sandwich.

drive dissipation. A nonrotating in-plane field, supplied by the very coils that operate the field-access portion of the chip, magnetizes the triangular permalloy points, converting them to low energy resting positions for bubbles. The primary drive for bubbles comes from areas defined by the conductor loops driven by a bi-polar current to alternately attract and repel bubbles. As a result, bubbles step from loop to loop but always move to the right because of the directionality induced by the triangular points described above. Bubbles attracted to these points offset to the right from their otherwise neutral position within a loop.

Dekker reported a power dissipation of 0.6 mW/b for this structure. It is thus difficult to conceive that their design could be used in an all-conductor chip, since the power dissipation for even a 100-kb chip would be 60 watts. We see in Section VII that chip partitioning can be used to reduce the dissipation considerably, but unlikely, in this case, to a useful level. Copeland's design, on the other hand, did operate at very low power per bit, but it was both wasteful of storage area and difficult to process. It was difficult to process because its minimum feature dimension was a very small portion of the circuit period.

This, then, was the reported status of current access bubble circuits. The expected advantages of higher data rates, ease of driving, and simple package design had not been realized.

III. APERTURED SHEET FUNDAMENTALS

It will be helpful to the understanding of the device structures covered later if we digress at this point to some design considerations peculiar to apertured sheet devices. First, let us consider some analogies that exist between the more familiar permalloy structures and the conductor structures that we introduce in this and the following sections.

An analogy exists between the stray field of an isolated permalloy bar immersed in a uniform magnetic field H and the stray field generated by the distortion of an otherwise uniform current I in a sheet conductor with a slot.[6] In either case, an isolated magnetic dipole is formed. This situation is shown in Fig. 4, where it can be seen that a "plus"-pole-seeking bubble would be attracted to the upper opening of the slot just as it would be attracted to the upper end of the permalloy bar. Note also that the directions of the magnetic field H and the current I are at right angles while producing identically oriented dipoles. We must be careful not to carry this equivalence too far, since the field H is applied over a volume, whereas the current I is confined to a plane. The practical significance is that a slot can completely block a current whereas a permalloy bar cannot completely shunt an applied field.

Next, it is useful to define a sheet current density $J(\text{mA}/\mu\text{m}) = I/\text{W}$,

where I(mA) is the current applied to a sheet of width W(μm). We can relate current density in conductor devices to inplane field intensity in permalloy devices by observing that an infinitely wide conductor carrying a current density $J = 1$ mA/μm supports an in-plane field of 6.3 Oe. This is illustrated in Fig. 5.

There are, of course, an infinite variety of aperture profiles that can replace the slot of Fig. 4. A number that we have considered are shown in Fig. 6. By fabricating large-scale models, energizing these in a left-to-right direction from a 30-kHz current source and then measuring the signals induced in a uniformly wound single-layer coil scaled in dimension to that of a hypothetical bubble, we obtained the z-field contours also included in the figure. The z-component is that field

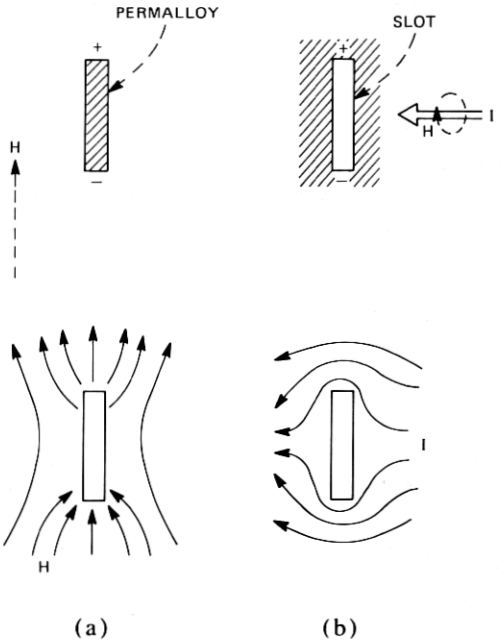

Fig. 4—Magnetic field H applied to a permalloy bar results in a dipole field. Current I applied to a conducting sheet produces a similar field.

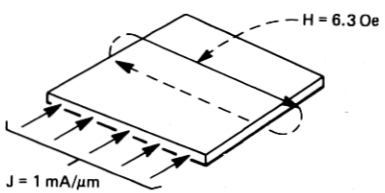

Fig. 5—A conducting sheet, infinite in extent, develops a 6.3-Oe surface field when driven at $J = 1$ mA/μm.

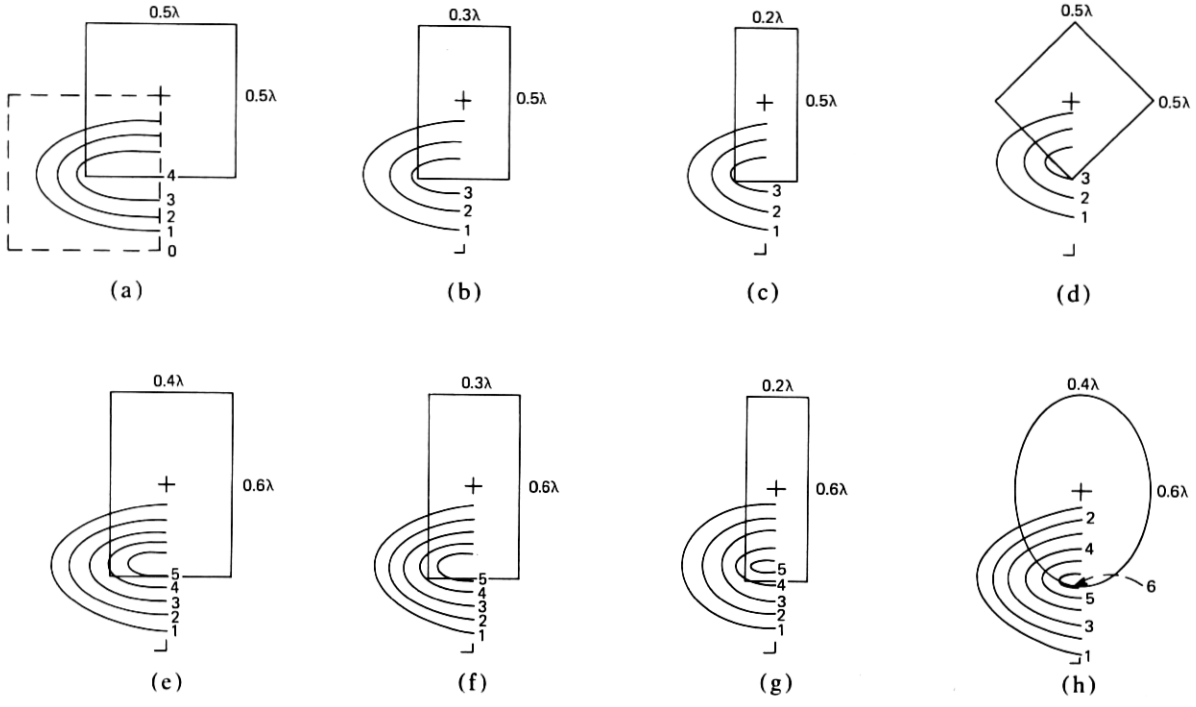

Fig. 6—Contours proportional to the z-component of field measured on scale models are given for apertures (a) through (h). Current flow was from left to right.

component normal to the sheet itself. The results actually apply to a square array of identical apertures positioned at center-to-center separations of λ. Only one quadrant of field is shown, as the others follow by symmetry considerations. Especially note how closely the field peaks and valleys are confined to the vicinity of the apertures. The oversized elements in the lower row give rise to larger fields than the shorter elements of the upper row, but at the expense of a higher power dissipation. We find the shapes "*b*," "*f*," and "*h*" optimal when items such as the ease of fabrication are also considered. Further details on this technique are given in Section X.

Similar results can also be obtained analytically and we have, in fact, devoted most of Section X to this end. One advantage of current-access bubble propagation is that they can be given a more precise mathematical treatment than is possible with field-access devices. Non-linear, permalloy-to-bubble interactions are not involved except, perhaps, in the detector itself. For example, we have calculated the field contours caused by current flow past a circular hole in an otherwise continuous infinite sheet. Two of the resultant design curves are given in Fig. 7, where h is the garnet thickness, a is the hole diameter, and Z_s is the elevation of the conductor sheet above the upper surface of the garnet. These contours give the average field in the garnet for an applied current density of 1 mA/μm. Conceptually, the role of the hole can be viewed as converting an otherwise uniform in-plane field (Fig. 5) into a bipolar field at about a 50-percent efficiency. This compares favorably to the conversion efficiency of a well-designed permalloy feature, which is also approximately 50 percent.

Next we consider the properties of an array of parallel conductor strips such as we encounter when detectors are discussed. The analytical results shown in Fig. 8 have been derived from design curves located in Section X. The parameters apply to a circuit period of 8 μm. For J = 1 mA/μm, the peak-to-peak bias field modulation is 9 Oe, meaning that a bubble "riding" in the field trough will have its bubble-to-strip transition field increased by 4.5 Oe. In an expander-type detector, it will be desirable to increase this transition field to at least 15 Oe so we can conclude that the current density in the detector will be increased to ~4 mA/μm. In conductor circuits, there is ample opportunity to do this.

We now present a problem peculiar to the apertured sheet geometry. Current in the conductor sheet not only generates the local field inhomogenities due to the apertures and an overall inplane field, but it also generates a gross z-field. The situation is shown in Fig. 9, where the field values pertain to J = 1 mA/μm. As might be expected, this field peaks at the edge of the conductor. As a consequence, any bubble located near the edge of a driven conductor sheet experiences a wide

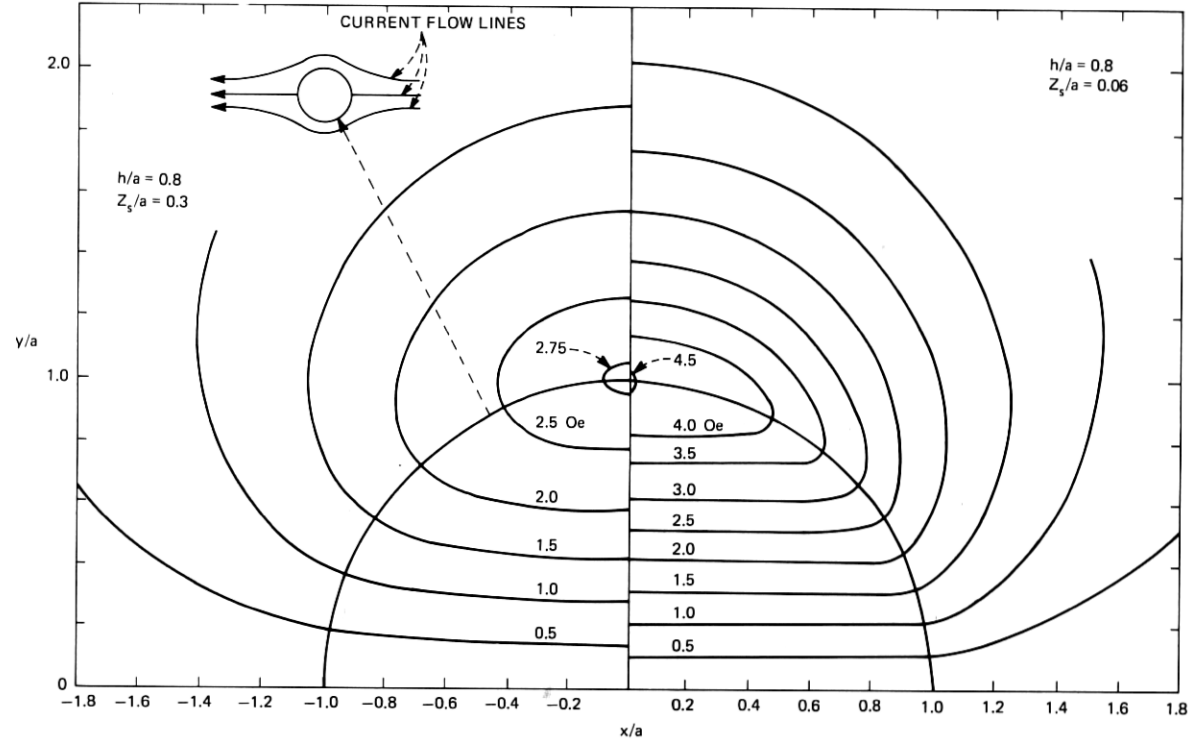

Fig. 7—Calculated z-field contours in the vicinity of a circular hole for a current density $J = 1$ mA/μm.

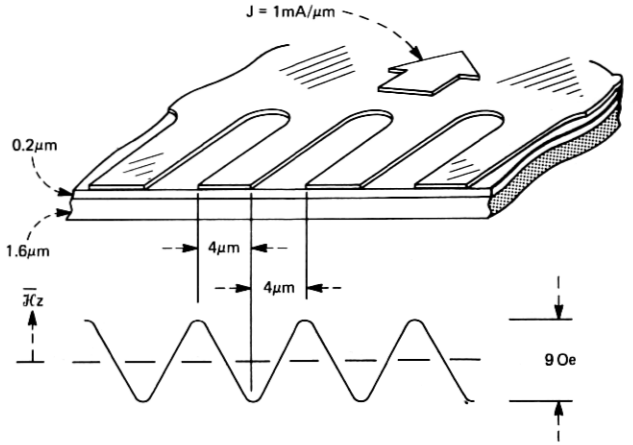

Fig. 8—$\bar{H}z$ variation generated by an array of parallel conducting strips. The dimensions are typical of an 8-μm period expander detector.

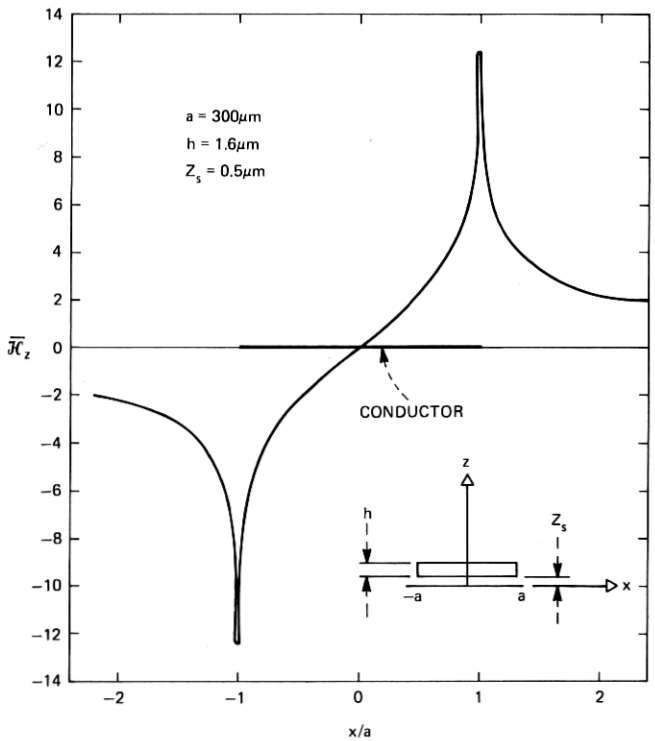

Fig. 9—Curve of the z-field due to a uniform current density $J = 1$ mA/μm flowing in a conducting sheet of width 2a.

bias change. This problem is substantially alleviated if active bubble circuits are confined to the central 80 percent of a sheet. Other solutions such as the use of a return conductor can also be employed.

Finally, let us contrast the performance of apertures and meandering conductors with respect to field localization and power efficiency. A comparison between the field contour of the undulating conductor given in Fig. 10 and those of Fig. 6 reveal that the fields of the latter more closely resemble those of a dipole. Furthermore, the fields produced by neighboring apertures are seen to be distinct and separate. Such is not the case for the former and, in fact, the edges of the conductor are biased to nearly one-half the peak field.

The structure of Fig. 10 requires one-third the current/cell to produce the same peak field as that of Fig. 6f; however, its resistance/cell is substantially higher. Consequently, there is little difference from a power dissipation standpoint.

IV. ROTATING CURRENT

In this conductor access scheme, the propagate elements are perforations in a continuous sheet of conductor material deposited directly on the epi-garnet. Bubble propagation is accomplished by a pair of

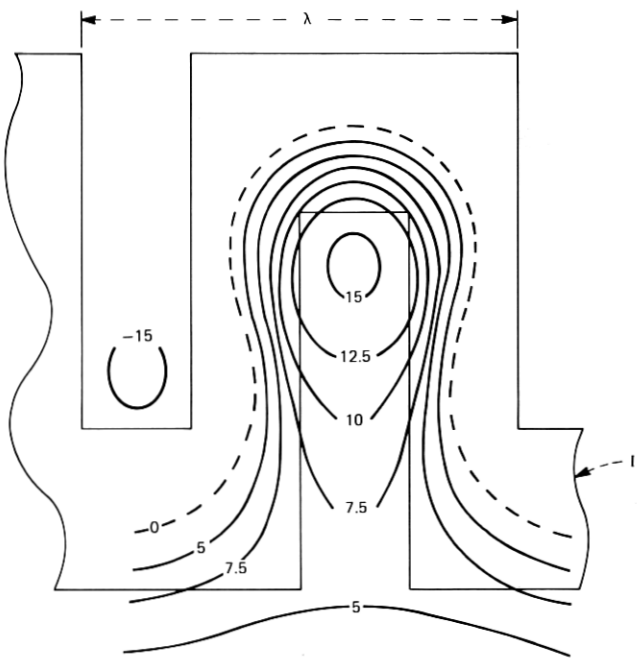

Fig. 10—Measured z-field contours for a meander-line conductor path. Note that the peak field extends toward the boundary of the conductor path.

bipolar currents applied in orthogonal directions to the conductor plane. This structure was first examined by T. J. Walsh and S. H. Charap.[6] Their computer simulations demonstrated the principle of operation. The obvious advantage over a field access device is the absence of field coils. This permits a simpler package and higher operating frequencies, which were previously limited by the field coils.

4.1 Principle of operation

A current is applied to a patterned conductor overlay. This current produces poles around the apertures. As the current is rotated in the conductor plane, the poles rotate about the apertures (see Fig. 11). In this figure, a chevron is the aperture (propagate element). As a current I passes from left to right, poles are established, positive on the bottom and negative on the top of the chevron. The bubble is attracted to the positive poles and will rest at the lower portion of the chevrons as in Fig. 11a. In the following three illustrations, the current is shown rotated in 90-degree steps. As the current rotates, the poles it produces also shift, giving rise to bubble propagation.

4.2 Experimental

Circuits were fabricated with 16-μm and 8-μm periods. Because of the processing advantages of single-gap structures, most test elements

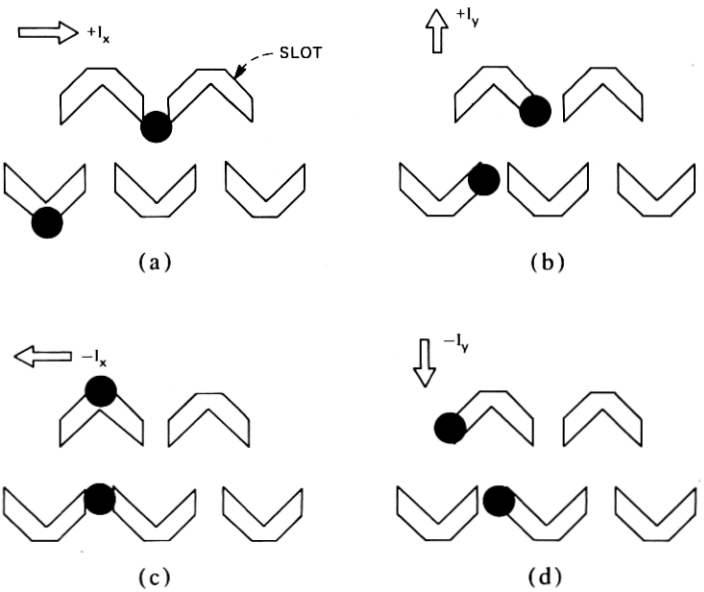

Fig. 11—Principle of operation for a circuit using rotating current for the drive. Motion, (a) through (d), proceeds much as for a single-gap permalloy circuit where chevrons are driven by a rotating field.

were chevrons. Multiple elements, such as the T-bar or X-bar, require tighter line-width control and tax processing capabilities. Portions of the masks used to make the circuits are shown in Fig. 12.

Circuits were patterned in a conductor film of 4500 Å AlCu. Bubbles were viewed in reflection with the conductor sheet serving as the reflecting surface. Four drive pulses are applied in quadrature for propagation, and a typical pulse train is shown in Fig. 13. Some overlap of adjacent current pulses is required. The amount of overlap was varied to ascertain the best operating margins with the lowest power dissipation. It was determined that 33-percent overlap was optimum. Note the slots in the arms of the test structures of Fig. 13. The slots function to keep the current flow lines parallel.

Both chevron and X-bar propagate elements were evaluated. The propagate margins for three chevron-like elements at an 8-μm period are given in Fig. 14. The margins are for various bubble patterns in straight-line propagation. Tests with different bubble patterns gave no indication of bubble-bubble interaction or reduction in propagate margin. Propagation through a 90-degree turn of Fig. 12c was marginal. The X-bar structure of Fig. 12d did not propagate domains' reliability.

4.3 Status

The high current densities required for propagation of 4 to 5 mA/μm as well as the complexities of providing multiple current drives into a common load curtailed efforts on this single-conductor approach. Consequently, problems associated with the design of generators, transfers, turns, and detectors have not been addressed.

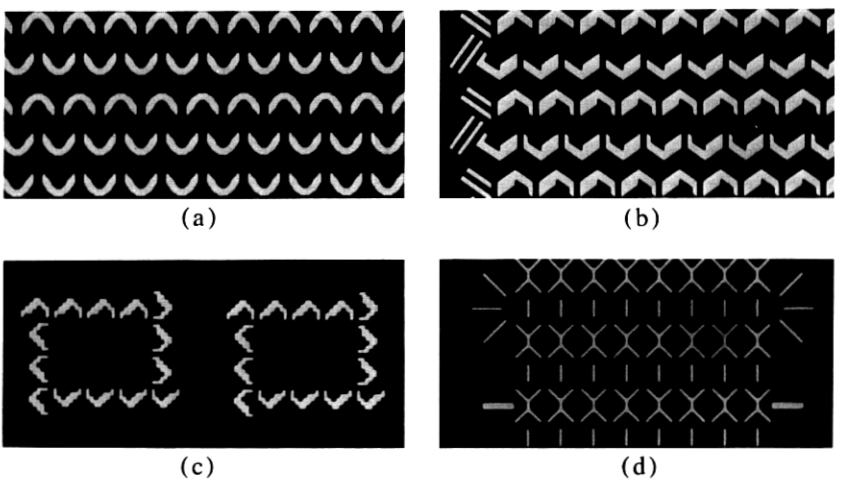

Fig. 12—Test masks used to evaluate rotating current structures.

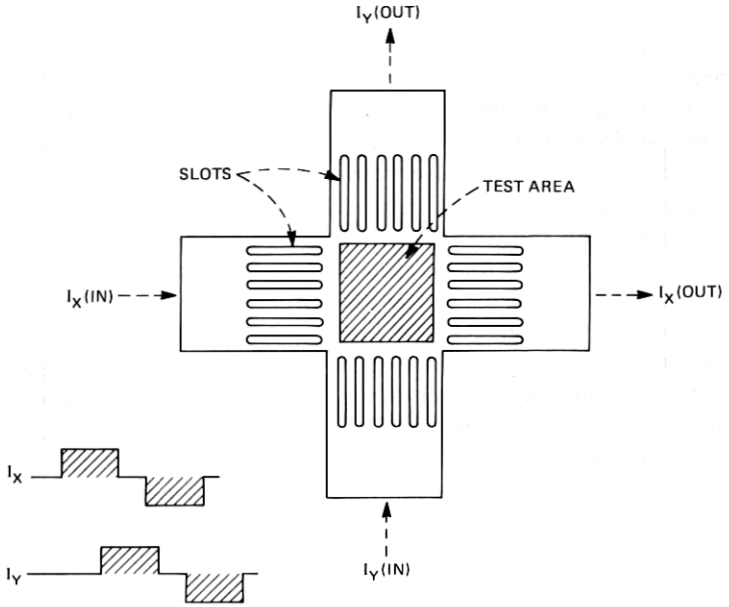

Fig. 13—Details of the overall test circuit. The slots in the lead-in arms prevent the current from "pin-cushioning."

V. CURRENT-ACCESS PROPAGATION BASED ON A STATIC OFFSET FORCE

In this section, we take an in-depth look at propagation circuits that can be driven by a single bipolar current source. The circuits of Copeland and Dekker discussed in Section II and those introduced in the following section, in which the meandering conductor is replaced by an apertured sheet, fall into this category.

5.1 Description

An excellent discussion of the static offset force problem has already been presented by Copeland et al.[10] We expand their results to include the effect of the domain wall coercivity H_C. In the usual single conductor circuit, the current flows in a conductor that crosses back and forth over the bubble track as shown in Fig. 15a. When a bipolar current is applied to the conductor, it produces an approximate standing wave field envelope:

$$H_I = N_I I \sin 2\pi x/\lambda, \tag{1}$$

where the X direction is along the bubble track and H_I is a Z-directed bubble drive field (Fig. 15b). It is obvious that a bubble can respond to

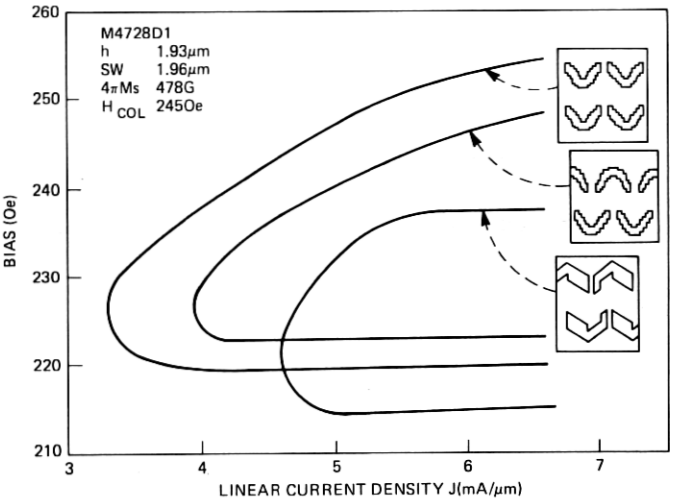

Fig. 14—Operating margins for the three aperture designs indicated.

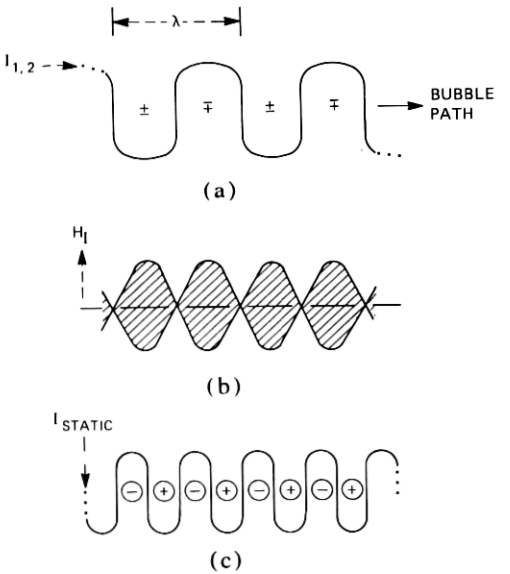

Fig. 15—Schematic layout of a single-conductor circuit. The conductor driven with a bipolar current (a) and the idealized z-field standing-wave pattern produced (b) are shown, as well as a double-frequency meander-conductor driven by a constant current (c).

this standing-wave field pattern by either oscillating back and forth or, more likely, being ejected from the track altogether. Next add the static current I_S (Fig. 15c) which produces yet another field pattern but this time with a double spatial frequency. This field is of the form

$$H_S = N_S I_S \cos(4\pi x/\lambda). \quad (2)$$

In eqs. (1) and (2), N_I and N_S are current-to-field conversion factors.

It is only illustrative, of course, that we use a static current I_S to produce H_S. We have already seen that grooves in a garnet or permalloy points can accomplish the same end and without an added power dissipation. If the dynamic (H_I) and the static (H_S) drive fields are properly proportioned, we achieve propagation as illustrated in Fig. 16. The ideal offset is $\lambda/8$ with an absolute maximum tolerance of $\pm \lambda/8$.

5.2 Conditions for bubble propagation

Before we discuss the constraints that must be imposed on H_I and H_S to obtain bubble propagation, it is helpful to review some bubble fundamentals. A field H applied to a stationary wall causes motion at a velocity v(cm/s) given by the equation

$$v = \mu(H - H_c), \quad (3)$$

where μ(cm/sec-Oe) is the wall mobility. In the case of a bubble, the change in field intensity across the bubble ΔH is used with the result

$$V = \frac{\mu}{2}[\Delta H - 8H_c/\pi]. \quad (4)$$

Since the bubble in the circuit (Fig. 15) experiences fields H_I and H_S simultaneously, we combine (1) and (2) to obtain

$$H_T = N_I I \sin 2\pi X/\lambda + N_S I_S \cos(4\pi X/\lambda). \quad (5)$$

There is no general analytical solution for the velocity of a bubble, even assuming H_I sinusoidal and $H_c = 0$. By graphical analysis we can,

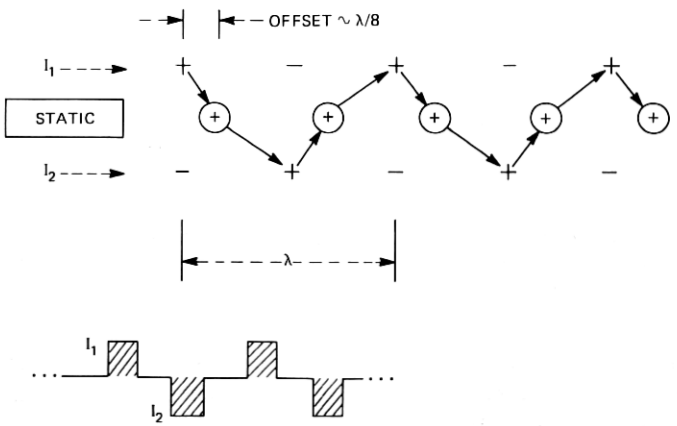

Fig. 16—The unidirectional propagation mechanism for the circuit of Fig. 15.

however, determine the minimum fields needed to overcome the coercivity H_c. From these we can determine the minimum drive currents. The mobility can then be introduced as an iteration of the coercivity under the assumption that the bubble moves at constant velocity.

The drive field H_I and the static field H_S and their sum are plotted in Fig. 17. It is assumed that positive fields increase the bias-causing bubbles to seek locations at which the applied fields are most negative. We treat the case where the bubble diameter is one-fourth the circuit period λ; however, the analysis can be extended to any diameter. Since mobility effects are being neglected, the condition $\Delta H \geqq 8H_c/\pi$ is sufficient to move a bubble. Actually, (4) is valid only for a linear gradient; however, we assume that any field difference at the extremes of the bubble diameter is equivalent to ΔH.

We start with a bubble in position 1 of Fig. 17, where 1 defines the location of the center of the bubble and, initially, with $H_c = 0$. Increasing H_I from zero to the amplitude sketched on the figure shifts the bubble from 1 to 2 and then, as H_I returns to zero, to 3. This completes a half-step of propagation. The other half-step takes place when H_I is reversed in sign. Next, we consider the conditions imposed on H_S when the coercivity H_c is included. There are "dead spots" at H_I (peak), and it is the role of the static field H_S to dislodge bubbles from those positions. The minimum values of H_S for any movement whatsoever is

$$2H_S = 8H_c/\pi. \tag{6}$$

Equation (6) therefore defines the critical minimum value for H_S. To

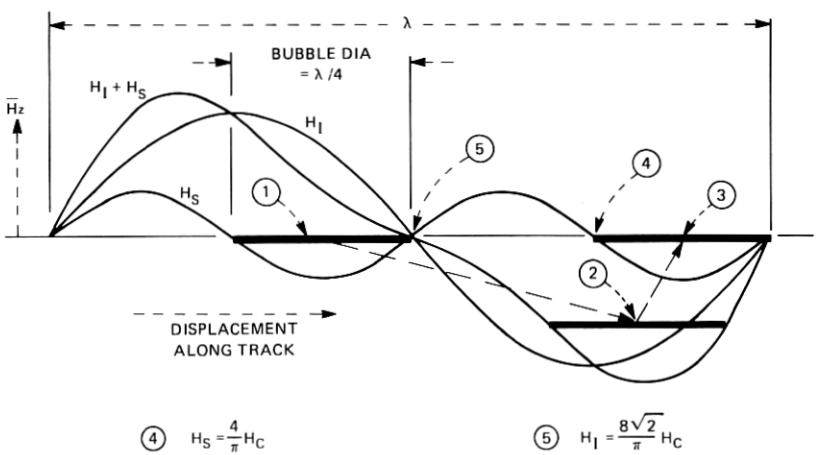

Fig. 17—Idealized z-fields H_I and H_S for a single-conductor propagation circuit with a static offset field. Bubble motion is from 1 to 3.

deduce the critical amplitude of H_I, we set $H_S = 4H_c/\pi$ and assume that there is a bubble at 1. As H_I is increased from zero amplitude, the bubble will move to the right, eventually reaching 5. Now 5 is a minimum gradient location for the bubble and, to overcome the coercivity, the amplitude of H_I must reach

$$H_I = 2\sqrt{2}H_S. \tag{7}$$

Once beyond 5, the bubble moves quickly ahead since it has excess gradient until it stops at 4, where again the field gradient is $8H_c/\pi$. When H_I returns to zero, the static field H_S completes this half-step by nudging the bubble a bit further to the right.

In summary, our two design equations are

$$H_S = 4H_c/\pi \tag{8}$$

and

$$H_I = 8\sqrt{2}H_c/\pi. \tag{9}$$

5.3 Methods to realize a static offset field

It is beyond the scope of this paper to list all the methods proposed to produce a static offset field. Permalloy dots, permalloy points, and embossed garnet features, i.e., grooves, are the three most extensively reported. In the next section, two more approaches are added to that list. They are (*i*) permalloy features contoured in the *z*-direction and polarized by the bias field and (*ii*) ion-implanted low-energy bubble rest positions produced by selectively implanting zones in the surface of the garnet. The remainder of this section, however, is devoted to "grooves," as they are representative of the other approaches.

In *Magnetic Bubbles* by O'Dell,[11] the equivalence of bubbles and current loops is discussed at length. This analogy serves as an excellent introduction to the subject of grooves. It can be shown that the stray field of a bubble and a loop current are identical if the bubble is replaced by a loop current $I_B = 2M_s h$, where the units are mA, gauss and μm, respectively. As an example, if $h = 1.5$ μm and $M_s = 40$ gauss, parameters typical for an 8-μm device, then $I_B = 120$ mA. Shown in Fig. 18a, the "loop current" representation aids in the comprehension of bubble behavior.

For a cylindrical hole in a magnetic layer, a similar equivalent current is $I_H = M_s h$, which, for the parameters above, is 60 mA. For partially etched holes, i.e., craters, the expression is $I_h = M_s \Delta h$ (Figs. 18b and 18c). Since an undulating groove is nothing more than a continuous chain of craters, the analogy can readily be extended to cover that configuration.

We have also included the design curves of Fig. 19, which give the

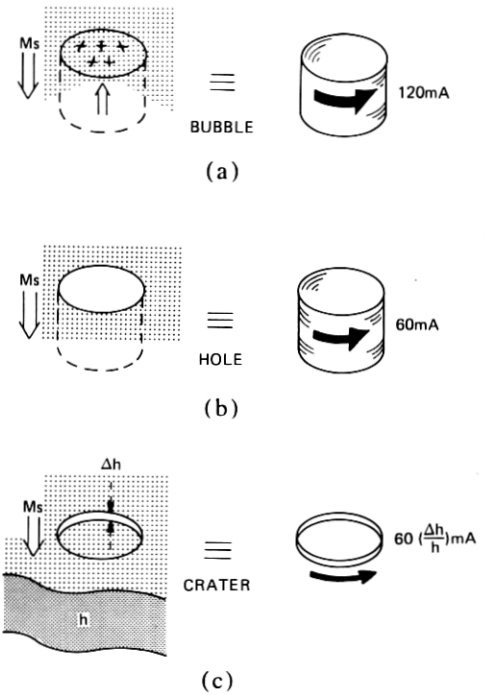

Fig. 18—The loop current magnetostatically equivalent to a typical bubble found in 8-μm period devices is given in (a). Similar relationships hold for a hole (b) and a partial hole (c).

field of a current loop located on the surface of a plate of thickness h. These curves will be useful if a more detailed analysis is attempted. They give the z-field averaged through the plate thickness h and normalized to the field at the center of the loop.

VI. KEYHOLE AND KNOTHOLE CIRCUITS

A class of bubble devices is now introduced, i.e., those driven by currents applied to apertured sheets rather than to arrays of conductors. In this section, only those configurations with a single conductor sheet are described. In Section VII, those circuits with two conductor sheets are covered.

6.1 Keyhole circuits

The idea for keyhole circuits originated from considerations involving the well-known "conductor crossing problem" in permalloy circuits. In particular, we were concerned with the role of the bias field. The bias field necessary to stabilize 6-μm and 1-μm diameter bubbles is about 180 Oe and 450 Oe, respectively. Consequently, the direct

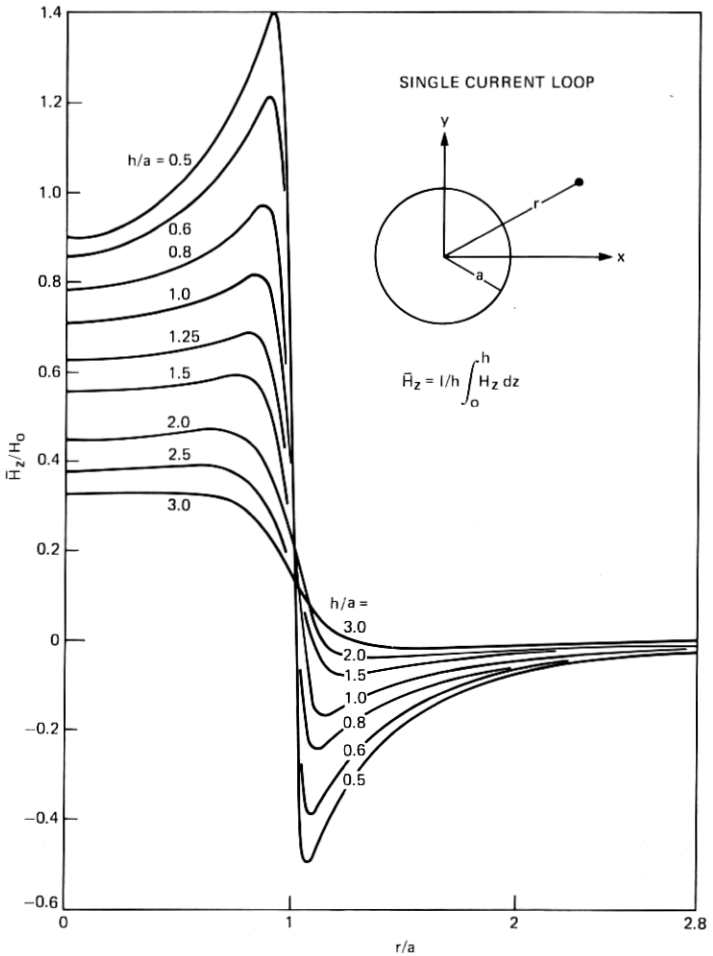

Fig. 19—Z-field contours normalized to the field H_O at the center of a current loop. These curves are useful to characterize bubble-bubble as well as bubble-etched feature (embossed) interactions.

influence of the bias field on the magnetic state of the permalloy features cannot be neglected in circuits with small bubbles, i.e., high density circuits.

We use the bias field to produce a static offset field by the approach seen in Fig. 20. The field H_{bias} has a component $H_{\parallel}$ directed along the body of any permalloy feature inclined to the plane of the garnet. Such is the case, then, for a permalloy feature patterned at the edge of a tapered conductor. Magnetic poles that repel bubbles develop at the end of the permalloy feature nearer the garnet, while those that attract

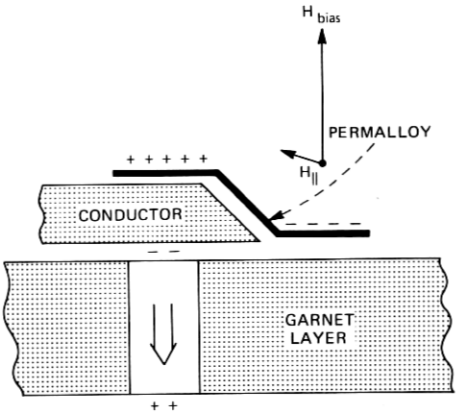

Fig. 20—A permalloy element, located on the edge of a tapered conductor, polarized by a component of the bias field.

bubbles develop at the end farther from the garnet. A reversal of the bias field direction will reverse the sign of the permalloy poles. However, the poles of the bubble also reverse, so the interaction remains unchanged. It is relatively easy to approximate the magnitude of the local field perturbations presented to the bubble. These calculations show that peak fields of a few oersteds to tens of oersteds can be expected.

Bubble propagation circuits capitalizing on this effect were designed; Fig. 21 is typical of those in which the apertures, squares fitted with a tab, are keyhole-like in design; hence, the name. Position and shape of the permalloy bar is seen in more detail in Fig. 22. For the reasons described above, bubbles are attracted to the ends of permalloy bars and repelled from their centers. Bubbles travel from left to right, moving from bar to bar in response to a bipolar current applied vertically to the sheet. They must "tunnel" through barriers as they travel from end-to-end on a given bar, but not as they jump from one bar to another. This asymmetry was apparent in the minimum drive currents of circuits that were tested.

For an 8-μm period circuit operated at 500-kHz, pulse amplitudes were required of 11.2 mA/μm to move along the permalloy and 7.2 mA/μm to bridge successive elements. Construction details were: 0.10-μm SiO_2 prespacer, 0.28-μm AlCu, 0.23-μm SiO_2 spacer, and 0.62-μm permalloy (ploy). With a garnet material that supported 1-μm bubbles, the operating bias range was 495 $\pm$ 17 Oe. A feature of this class of circuits is that they can accommodate a very wide range of bubble diameters. One foremost disadvantage is that they are difficult to process because of the intricacies of the aperture design.

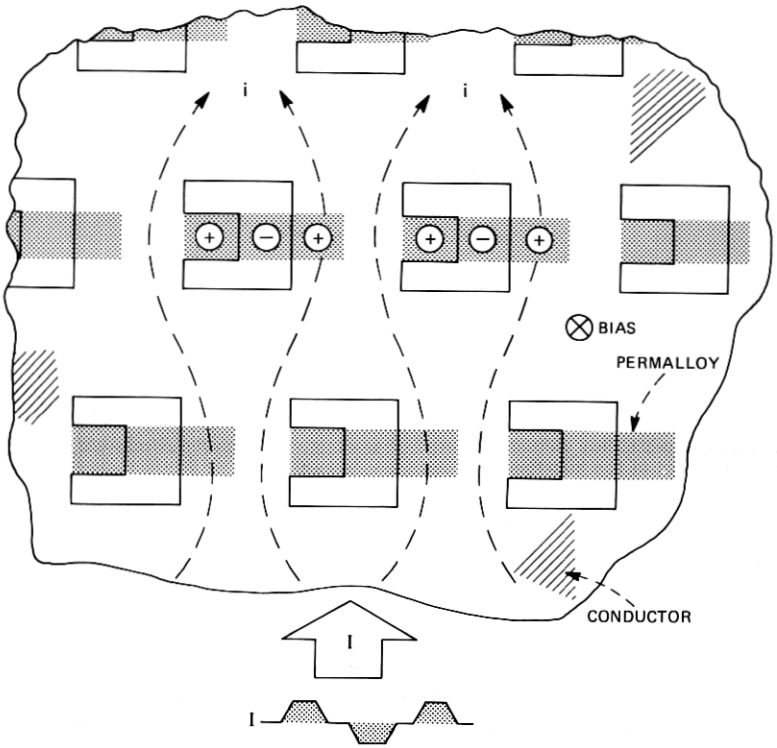

Fig. 21—Bubbles in this keyhole circuit move from left to right in response to a bidirectional current drive. The tab within the hole elevates the end of the permalloy bar but does not interfere with current flow around the aperture.

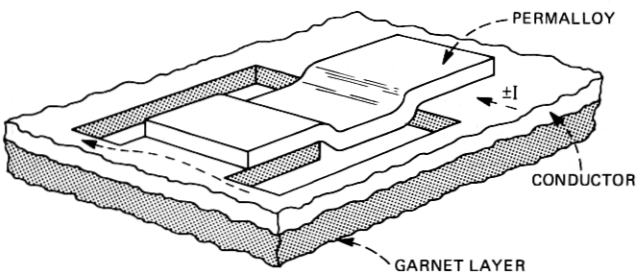

Fig. 22—Perspective view of a keyhole aperture shows the contoured permalloy.

6.2 Knothole circuits

In a knothole circuit, ion-implanted islands are combined with a single-apertured conductor sheet to form a bubble shift register. Uniform ion implantation of a garnet surface is the traditional method of

suppressing hard bubbles. Field-access bubble propagate circuits that use implanted patterns rather than permalloy elements are being considered for next-generation high-density applications. The uniaxial anisotropy of most garnet materials, and especially those treated in this paper, is lowered by any implantation that stresses the lattice. One can consider that bubbles couple to implanted areas because these areas tend to reduce the stray field energy by providing flux closure. The interaction, however, is more complex, as it can involve "charge walls" in the implant layer. Also, bubbles are especially attracted to the implant side of boundaries that partition implanted and nonimplanted areas. Phenomologically, an implanted island behaves like that of an area that has been thinned and as such can be replaced by a loop current. It follows then that the knothole circuit is a physical representation of the hypothetical structure analyzed in Section V.

A straight-line knothole shift register requires two implant islands and a single, simple aperture for each circuit period. Note that a tab in the aperture is no longer necessary and has been removed. Hence, this circuit has been given the descriptive name knothole. The general layout and operation of three parallel shift registers is illustrated in Fig. 23. Bubbles in the center row propagate to the right, those in the

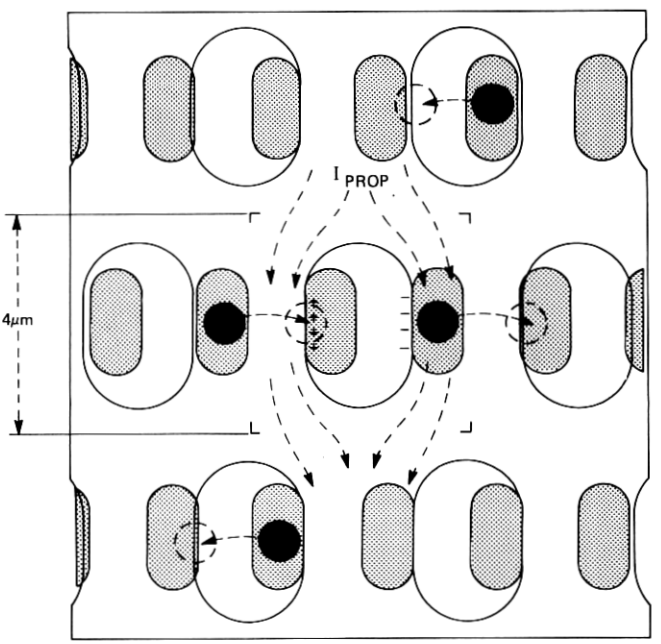

Fig. 23—Bubbles move from rest positions at the ion-implanted islands in response to current flow downward. Each circuit period requires two implanted islands.

outside rows propagate to the left. A bipolar current applied to the sheet drives the bubbles.

The performance of knothole circuits is sensitive to bubble size. To illustrate this point, refer to Fig. 24 where the data are presented for a 4-μm period test circuit using a nominal 1.7-μm bubble material. Islands were given an implant of 2.5×10^{13} Ne at 100 Kev, and no overall implant was included. A static in-plane field of 210 Oe was applied parallel to the current. Bias margin, frequency range, and drive power/bit (based on 0.1 ohms/cell) are outstanding. The direction of propagation is *opposite*, however, to the design direction. The oversize bubbles straddle pairs of implanted areas during operation.

Design of an 8-μm period closed-loop shift register is given in Fig. 25 and data in Fig. 26. Here the nominal bubble diameter is 1.6 μm, which is a good match to the nominal 2 μm by 4 μm implant islands; hence, the direction of propagation is correct in the classical sense, i.e., clockwise around the loop. The islands were implanted at 3×10^{13} with Ne at 50 Kev. Driven at $J = 3$ mA/μm, the continuous power dissipation is 58 μw/b.

A variety of π-turns were tested during the course of this development, and the most successful of these is incorporated in the circuit of

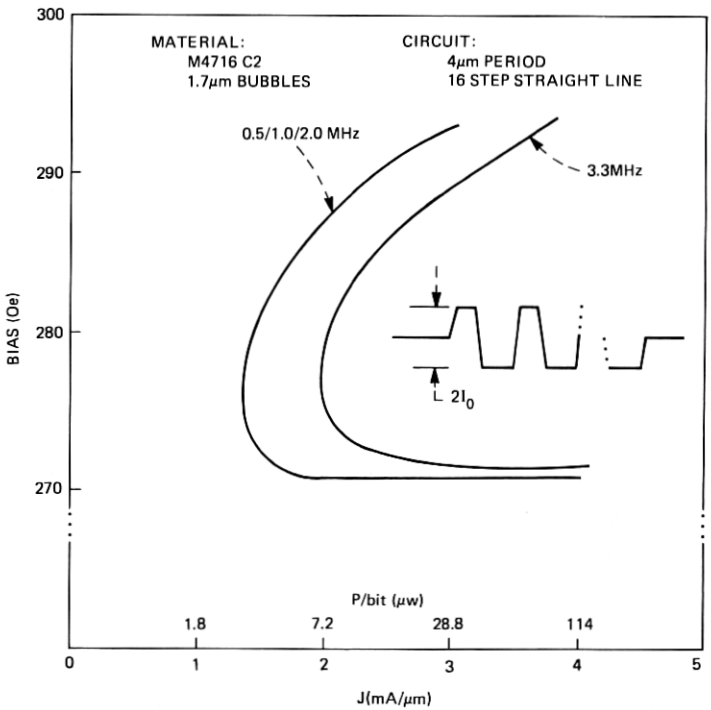

Fig. 24—Operating margins vs frequency for a 4-μm period knothole circuit.

Fig. 25. The shape of the aperture in the turn was optimized from field plots on scale models and iterated until the desired drive gradients were seen. Operating margins of this turn improve when an in-plane field is applied parallel to the direction of the drive current. For the data of Fig. 26, the in-plane field was 100 Oe.

Straight-line propagation parallel to the drive current was achieved with the circuit of Fig. 27. Operating margins are similar to those obtained for propagation normal to the current, and much of the same design criteria apply here. Although the drive currents per cell are lower, the resistance/cell is substantially higher; thus, the power/cell is essentially unchanged.

A detailed description of support functions such as generation and detection is deferred until Section VII, which treats dual conductor circuits.

VII. DUAL CONDUCTOR OPERATION

The knothole configuration with its single perforated sheet and "offset-force" zones does not have the design flexibility that can be

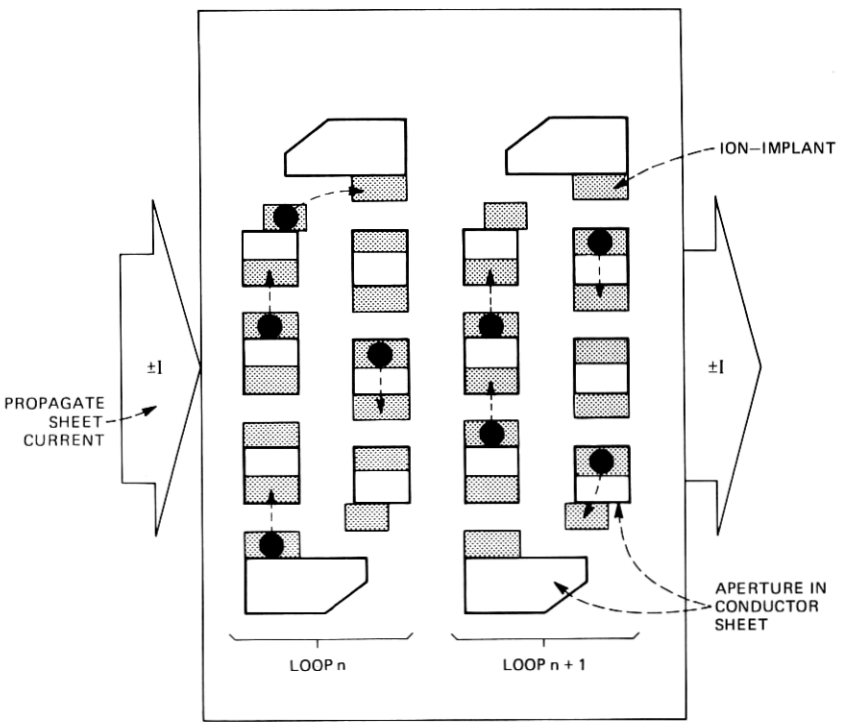

Fig. 25—Details of π-turns used in 7-step shift register loops. Clockwise turns can be mirrored to make counterclockwise turns.

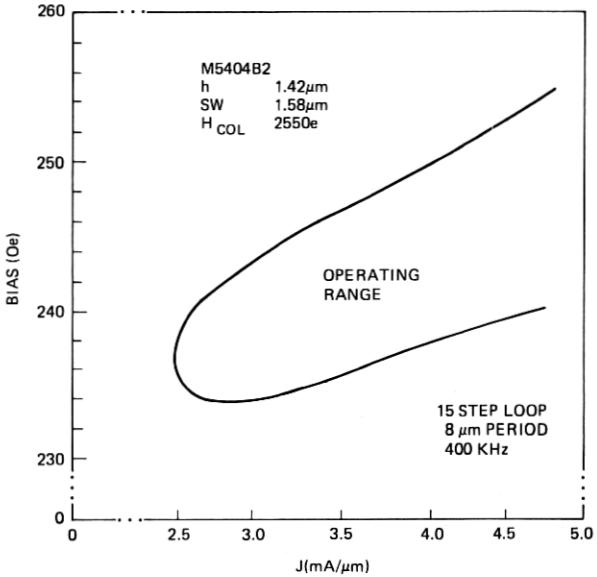

Fig. 26—Data for a 15-step knothole loop designed as in Fig. 25. Bubbles were propagated in 14-step bursts.

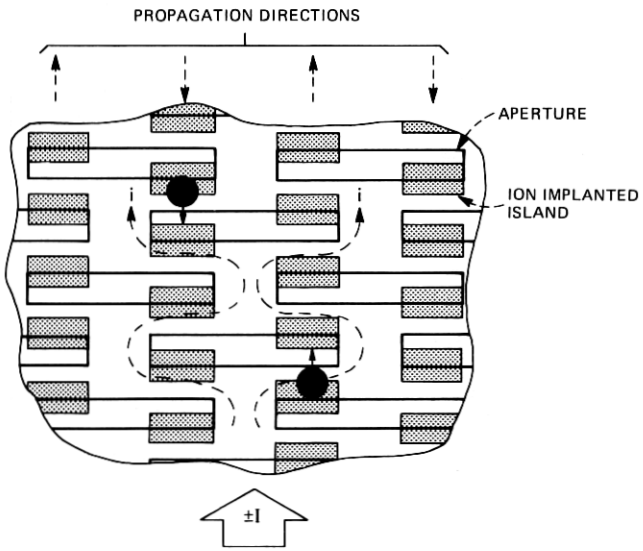

Fig. 27—Propagation parallel to the direction of general current flow.

achieved with a pair of conductor sheets. For example, with the pair of conductor sheets it is possible to transfer a bubble, i.e., switch a bubble from one path to another, or reverse the direction of propagation, simply by altering the propagate pulse sequence. This section deals

with straight-line propagation parallel and perpendicular to the direction of current flow, closed loop design, nucleate generation, detection, and transfer. Also included is a discussion of factors that influence chip design. The discussion is limited to the case where the currents in the two levels flow either parallel or anti-parallel to one another. It will be apparent to the reader, however, that, if the structures are reconfigured so that the currents flow perpendicular to one another, a new family of device structures somewhere between the rotating current structures of Section IV and those of this section could be realized.

Dual conductor circuits are fabricated with a first patterned conductor level either directly on the epitaxial garnet or onto a pre-spacer layer, an insulating layer, and finally a second patterned conductor level. Details of the actual fabrication are covered in Section IX. It will be useful at this time to describe the general layout of the test structure depicted in Fig. 28. All the test data described in the following sections were taken on circuits located within the cross-hatched region which is 320 μm wide and 600 μm long. The paths that lead into this region are shaped to make the current density within the region as uniform as possible.

In line drawings equivalent to processed circuits, for a view looking down onto the second conductor layer, the following conventions will be established and used throughout (see Fig. 29). All apertures in the first conductor level (that nearest the garnet) are outlined by a solid line, whereas apertures in the second level are indicated by a dot pattern. Sheet currents $I_{1,3}$ and $I_{2,4}$ flow in the first and second

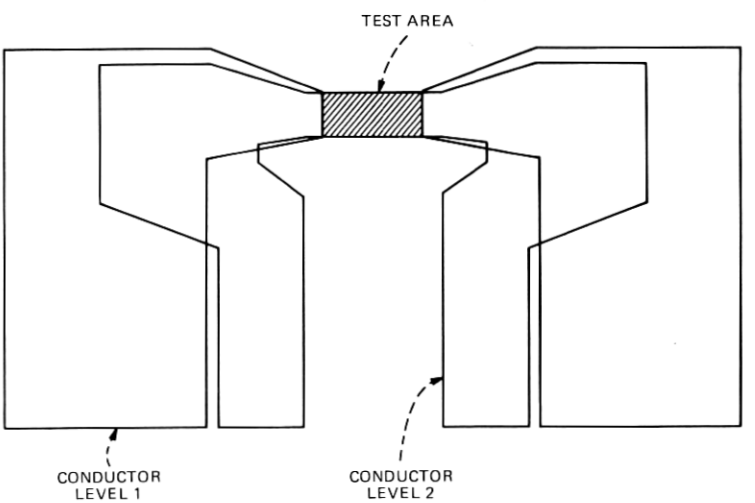

Fig. 28—Layout of the circuit used to test dual-conductor designs. Two or more probe fingers contact each pad area located along the bottom edge. Uniform current density is maintained at the test area.

conductors, respectively, where they generate local bias-field perturbations at positions 1, 3 and 2, 4. For a bubble-stabilizing field H_{bias} directed downward as shown, bubbles are attracted to location 1 for current I_1, location 2 for I_2, etc.

7.1 Propagation normal to the current flow

In Fig. 29, it can be seen that a bubble initially at position 1 propagates upwards (normal to the direction of current flow) when the current pulse sequence [234] is applied. Sequence [321] returns the bubble to its starting position. Straight-line propagation over a further distance is achieved by simply linking like pairs of apertures as in Fig. 30. The length of each aperture is 0.5λ, and the distance between successive like positions is the circuit period, λ. It should also be apparent that the maximum tolerable misalignment of apertures in the vertical direction is 0.25λ.

Typical current-pulse waveshapes to produce the sequence

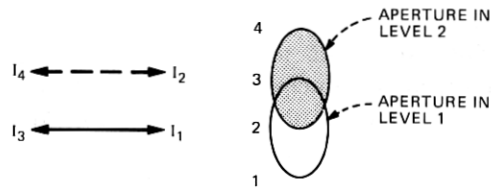

Fig. 29—A four-position, dual-conductor, bubble-stepping circuit. Bubbles are attracted to positions 1 through 4 when currents I_1 through I_4 are applied.

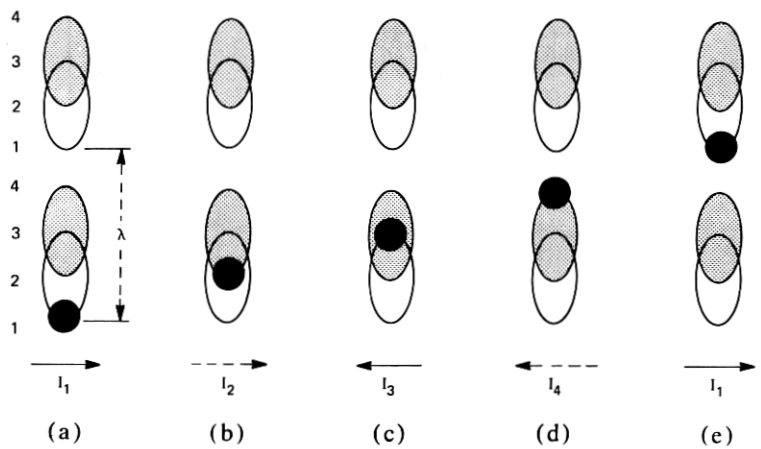

Fig. 30—A time sequence of the operation of a dual-conductor shift register. The direction of propagation will be reversed if the currents are applied in the sequence (e) through (a).

[123412341] for stepping a bubble through two periods are sketched in Fig. 31. Some overlap between successive pulses is helpful to further quantize the traveling-wave bias field minimum that drives the bubble. Also, to get a bubble fully advanced into position for, say, another two-step burst, then a final [41] overlap should be provided.

Success in aperture design is measured in terms of generating the maximum possible field gradient for the lowest power dissipation. Almost any aperture will perturb an otherwise uniform current density and give rise to bubble motion. Some of those tried were shown in Fig. 6, along with field plots obtained on scaled-up models (details in Section X). This field data information coupled with both processing and operational experience points to the rectangular shape 0.3λ by 0.5λ as the most practical choice.

The operating margins for a series of 8-μm period dual-conductor test circuits are presented in Figs. 32 to 38. Circuit data cover both unimplanted and implanted garnets as well as the influence of in-plane fields parallel to the drive currents. A frequency and temperature run are also included. Individual data points are shown wherever they aid in understanding the experiment. Bubbles used in these tests were obtained by subjecting a chip to a large in-plane field. Testing continued until the bubble supply was depleted, and a new supply was initialized.

We report, in Fig. 32, 1-mHz data on an implanted garnet test circuit driven with a two-step to and from sequence [1234123432143214]. Of special interest is the spread in data points, especially at low drive. We suspect that this is a result of the bubble states found in implanted garnets[12–14] and to a greater extent in unimplanted garnets. The domain structure of the implanted layer is also suspected.

The low bias margin is limited by stripout, as is usual for most of the dual-conductor circuits tested. This is especially significant when detection is considered. Free-bubble collapse limits the absolute upper bias, since "hold currents" are not maintained between pulse bursts. If an in-plane field is applied,[15] much of the uncertainty in the data points is eliminated, as is evident in Fig. 33.

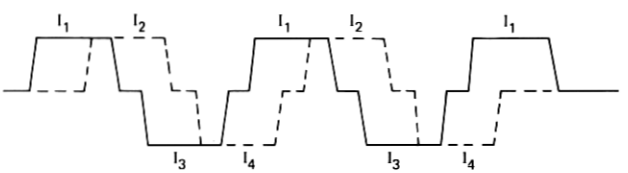

Fig. 31—The current pulse sequence used to step bubbles in a dual-conductor circuit. The overlap of pulses is used to further quantize the propagation field.

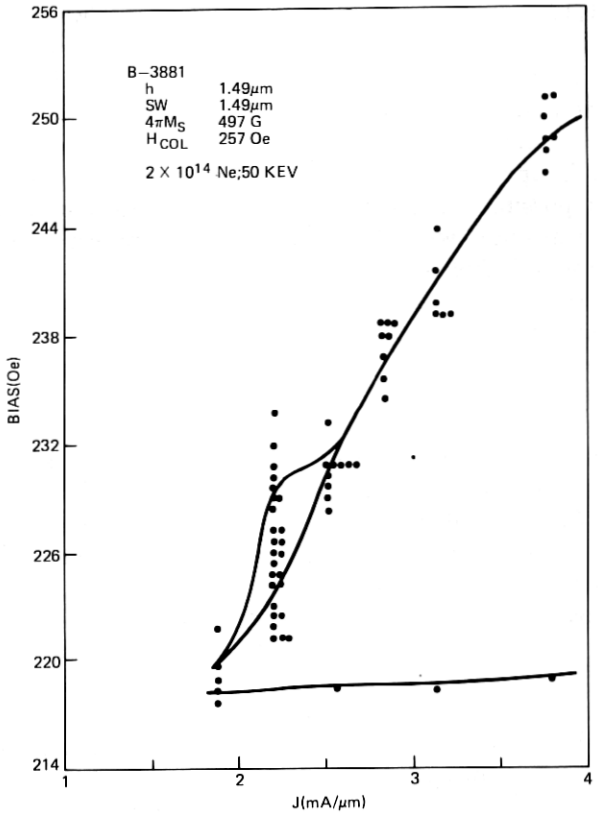

Fig. 32—Bias margin vs drive for an implanted garnet tested at a 1-MHz stepping rate in an 8-μm period dual-conductor circuit. Each data point represents an individual check of the upper bias margin. The spread in the test data indicates that the bubble state and/or the implant layer magnetization does not reproduce from test to test.

When an unimplanted garnet is tested, the upper bias margin often shows two distinct distributions (Fig. 34). Failure modes associated with these curves indicate that two distinct bubble states, probably the $S = 0$ and $S = 1$, are involved. With a sufficiently intense in-plane field, the double distribution disappears. Refer to Fig. 35, where margins for both a 200-Oe and 300-Oe in-plane field are given.

These experiments suggest that an in-plane field is helpful to stabilize bubble propagation in dual-conductor circuits. We do expect the shape of the field gradients to continually redirect bubbles toward the desired path. However, it is known that $S \neq 0$ bubbles do not move along the maximum field gradient, but rather at angles (often near right angles) to the gradient. In Table I, the skew angle calculated for $S = 1$ bubbles are tabulated for the garnet compositions reported in this paper. Further insight into the problem comes from an analysis of

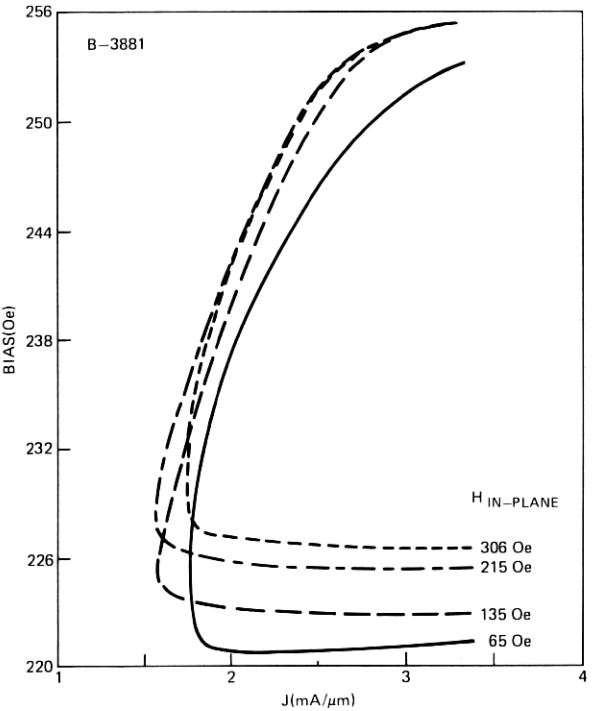

Fig. 33—Margin data for the conditions of Fig. 32, except that an in-plane field from 65 to 306 Oe was applied parallel to the current flow. The spread in data points was virtually eliminated.

Table I—Comparison of material parameters

Material Type	q (ratio)	$4\pi M_s$ (gauss)	ΔH_c (Oe)	μ (cmS/s-Oe)	γ (l/Oe-s)	ψ^* (degrees)	$f_{OPT}\dagger$ (MHz)
YSmLuCaGe garnet	3.8	524	2.0	300	1.7×10^7	22.5	0.4
LaLuSmGa garnet	4.0	478	1.5	500–1000	1.7×10^7	35–45	0.5–1.0

* Tan $\psi = 4\mu S/\gamma d$ $(S = 1)$.
† $f_{OPT} = 4\mu H_c/\pi\lambda$ $(\lambda = 8\ \mu m)$.

the trajectory of an $S \neq 0$ bubble moving in the dipole field generated at a circular hole. Details are presented in Section X. The choice of whether to cope with bubble states by one of the conventional hard bubble suppression methods or by an in-plane field will be dictated by the method chosen to detect bubbles. It may prove advantageous to shape the apertures, particularly in turns, to take advantage of preferred propagation angles.

In Fig. 36, the results are presented of a frequency run on an unimplanted garnet in a 200-Oe in-plane field. These results are

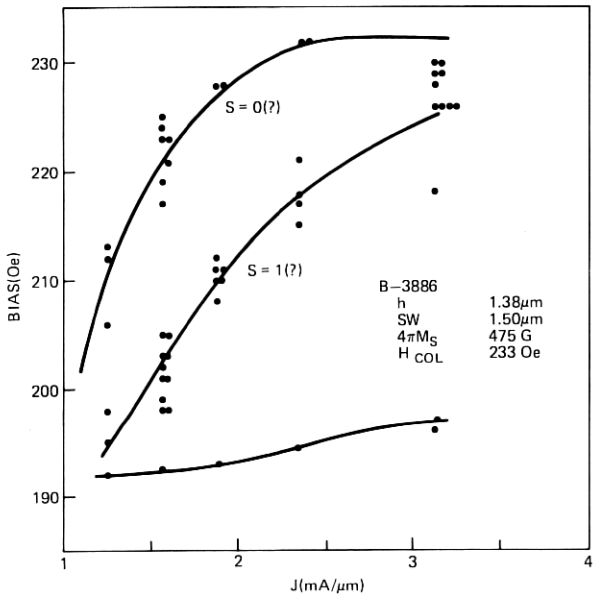

Fig. 34—Bias margins vs drive for an unimplanted garnet tested at 1 MHz in an 8-μm period dual-conductor circuit. Two distinct distributions in the upper bias margin were observed.

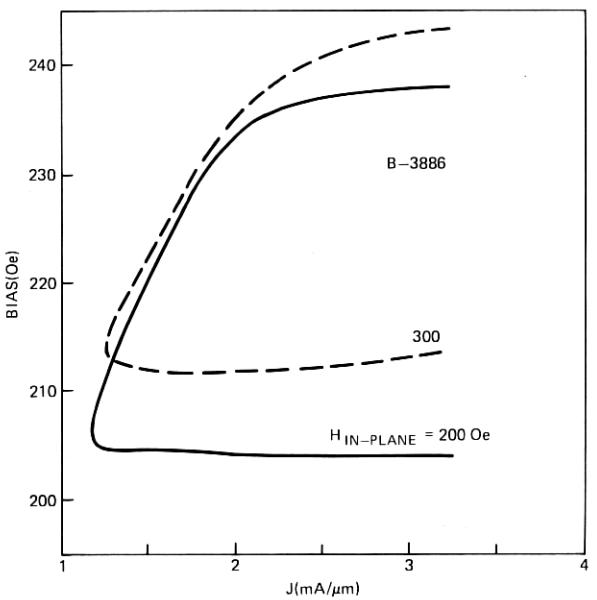

Fig. 35—The data of Fig. 34 repeated except with an in-plane field applied parallel to the current. With unimplanted garnets, substantially higher in-plane fields are needed to tighten the data points.

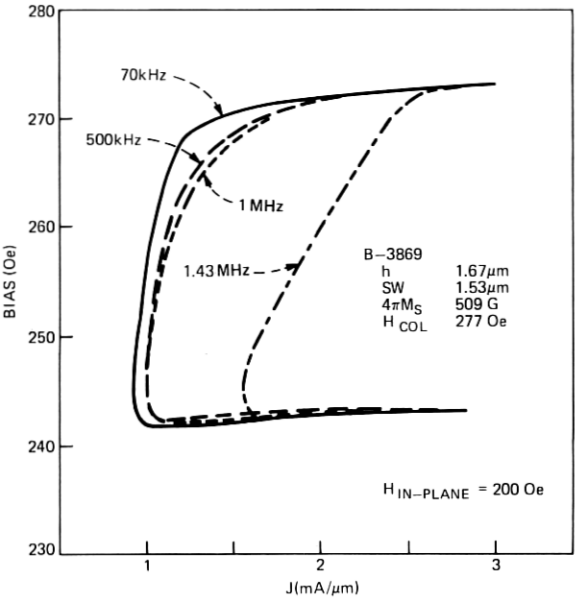

Fig. 36—Operating bias margin vs frequency for an unimplanted garnet film with a 200-Oe in-plane field.

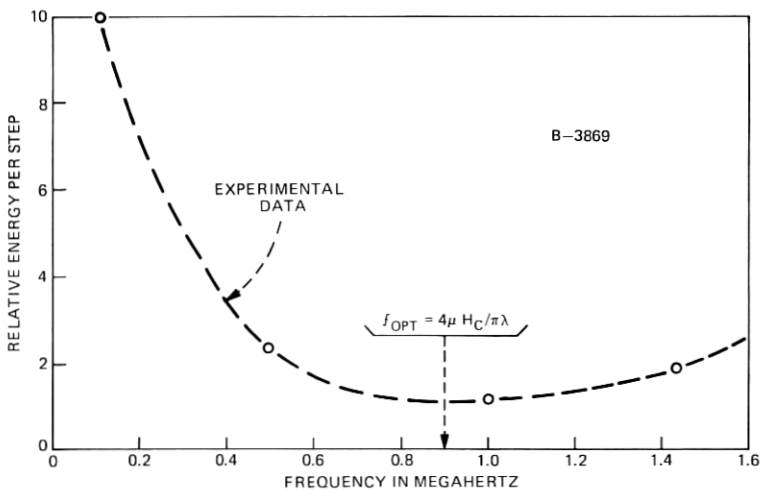

Fig. 37—It is wasteful of power to run current-access circuits except at a frequency f_{OPT} at which the energy dissipated per step is a minimum. Calculated and experimental values of f_{OPT} are compared.

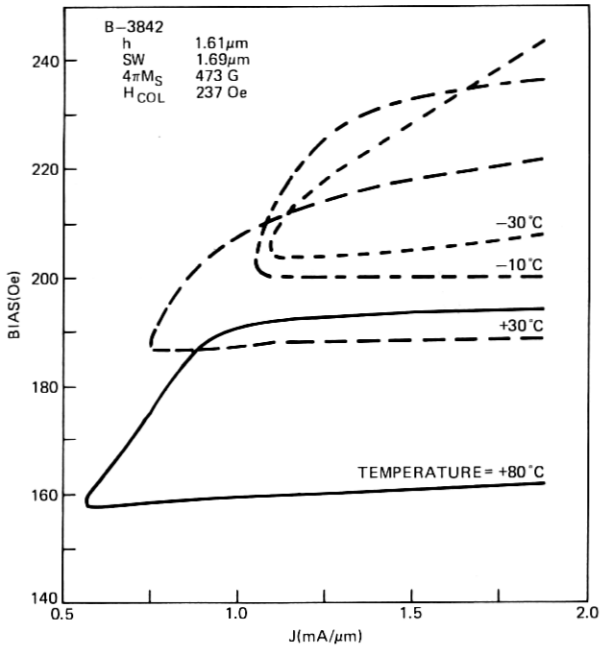

Fig. 38—Operating margins vs temperature taken at 30 kHz with a four-step propagation sequence. The garnet was unimplanted.

consistent with predictions based on calculated drive gradients and measured garnet properties. We can use these results to introduce f_{OPT}, the optimum frequency at which to step a bubble from one point to another to minimize energy dissipation. It can be shown that $f_{OPT} = 4\mu H_c/\pi\lambda$. The relative energy per step (proportional to J^2/f) vs frequency calculated from the data of Fig. 36 is plotted in Fig. 37. The calculated f_{OPT} for wafer B-3869 (H_c = 0.5 Oe, μ = 1,000 cm/sec-Oe) compares favorably to the frequency corresponding to the energy minimum of Fig. 37.

Operating margins at 30 kHz for an unimplanted garnet over the temperature range −30°C to +80°C are given in Fig. 38. These data were furnished by J. L. Smith. The minimum drive increases at low temperature much as expected due to the increase in coercivity. Note especially the very wide margins at 80°C.

7.2 Propagation around a closed loop

Details of a nine-step, bi-directional, closed loop are illustrated in Fig. 39. Note that the slots in the turn are 0.75λ in length and that elements that lead into the turn are repositioned somewhat. Bubbles propagate clockwise for the drive sequence [···12341234···] and

counterclockwise for [· · ·43214321· · ·]. Bias field-drive characteristics for a 6-μm period loop operated at 1 mHz are given in Fig. 40. The margins are quite adequate, as is generally the case for loops at the center of the test area. If z-field cancellation is not used, bubbles in

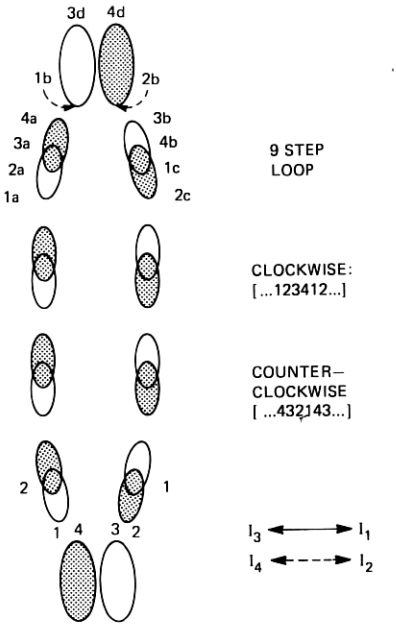

Fig. 39—A 9-step dual-conductor closed loop. The elliptical apertures in the turns have been lengthened for the reasons described in the text.

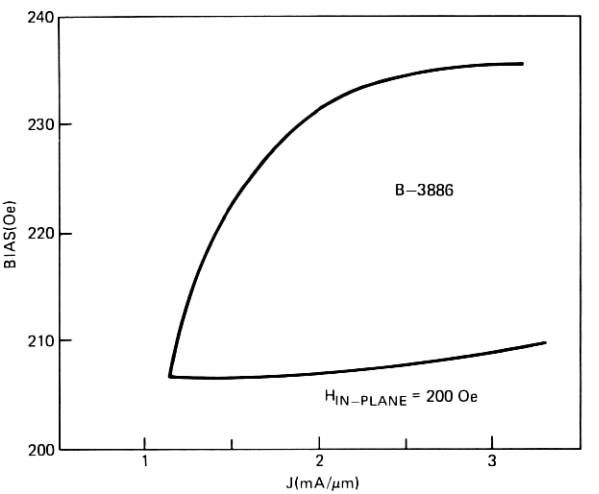

Fig. 40—Bias margin vs drive for a 6-μm period, 7-step loop operated at 1 MHz. The garnet was unimplanted.

loops located near the outer edges of the test area are biased by both an alternating and a constant field. A typical failure mode (Fig. 39) finds bubbles in clockwise motion, jumping to 3d from 2b rather than stepping to 3b. Some modifications were necessary to cope with this problem.

First, the two slots in the turn were lengthened further to 1.25λ and, second, additional apertures were placed beyond the turn itself to help equalize the current distribution. The latter is readily accomplished by interconnecting loops end to end (Fig. 41). Note that the bubbles in adjacent loops move in paths counter to each other just as the gears of a gear train.

Impetus for making the modifications given above came from test circuits in which interconnecting loops spanned the width of the test area. Loops with lengthened turn-elements outperformed all the others in positions 1 and 5, whereas all loops were satisfactory in positions 2, 3, and 4.

These experiments also gave additional evidence of the "gyro" nature of the bubbles in our materials. Consistently, the even-numbered loops outperformed the odd-numbered loops for one direction of

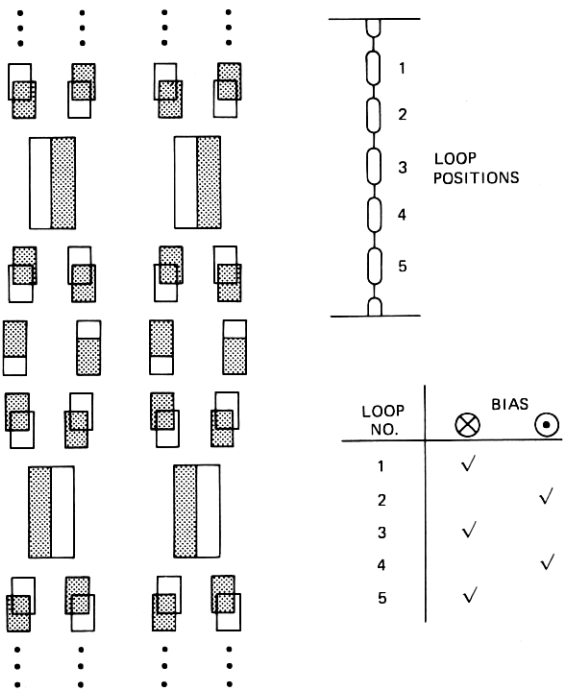

Fig. 41—Loops can be interconnected end-to-end by the method shown. The propagation direction of adjacent loops alternates, i.e., cw, ccw. Performance is related to the propagation sense and bias field direction.

bias and vice versa. One additional observation not as yet understood was made: Operation was generally better if the bias field was directed toward rather than away from the garnet surface.

7.3 Propagation parallel to current flow

In this section, propagation parallel to the direction of general current flow is considered. This is not an absolutely essential operation for a chip layout, since such motion can also be made by combinations of motions normal to current flow and the π-turns discussed in the preceding section. In fact, our earliest shift registers were designed that way. The principle of operation, from Fig. 42a, is straightforward. A bubble starting at the leftmost position 1a proceeds through 1a2a3a4a1234 in response to pulse sequence [123412341].

The actual operation is far from ideal, since propagation down the center track is stable only for a restricted (and oftentimes non-existent)

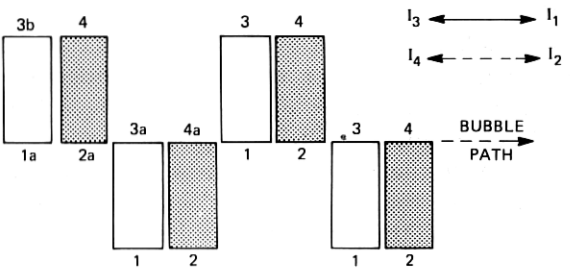

(a)

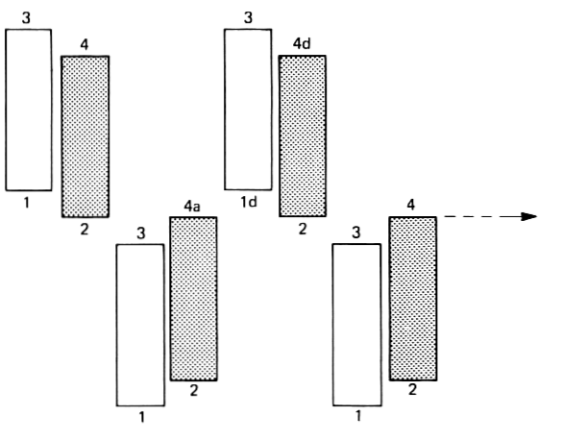

(b)

Fig. 42—Circuit for propagation parallel to the current. The original bidirectional design (a) was modified (b) to be unidirectional to improve performance.

set of drive and bias conditions. It is observed that a bubble in transit through 1a2a jumps to 3b rather than proceeding to 3a as desired. This occurs since the current density at 3b, and thus its pole strength, is substantially greater than at 3a, thereby counteracting 3b's increased distance from 2a.

Operation improves substantially if the apertures are increased in length and staggered as shown in Fig. 42b. This modification further removes the offending poles from the intended bubble track and also forces increased current along the bubble track. As a result, the circuit of Fig. 42b gives adequate margins for motion [· · · 12341234 · · ·], however, motion along [· · · 43214321 · · ·] is unreliable because of encounters such as 1d to 4d rather than 4a.

Operating margins for an 8-μm period shift register stepped at a 1-mHz rate are given in Fig. 43. The garnet was not implanted nor was an in-plane field applied. The performance is seen to be quite good.

7.4 Bubble generation

A nucleate bubble generator can either be patterned in one of the propagation conductor levels or it can be provided in a separate conductor level. Only the former design is considered here, since the design of the latter is obvious. Now it is possible to introduce slots in a sheet conductor if the slots are narrow (1/4λ or less) and run essentially parallel to the current flow. Such slots can be used to concentrate current and thus nucleate bubbles, yet permit current flow during normal propagation. Just how this can be done is seen in Fig. 44.

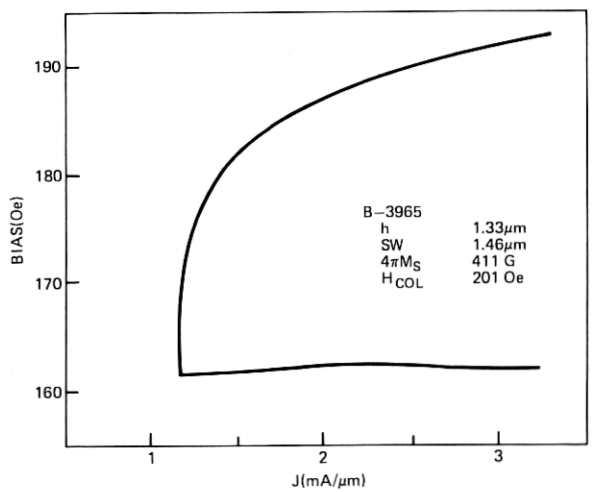

Fig. 43—Bias range vs drive at 8-μm period and 1 MHz for circuit (b) of Fig. 42. The garnet was not implanted.

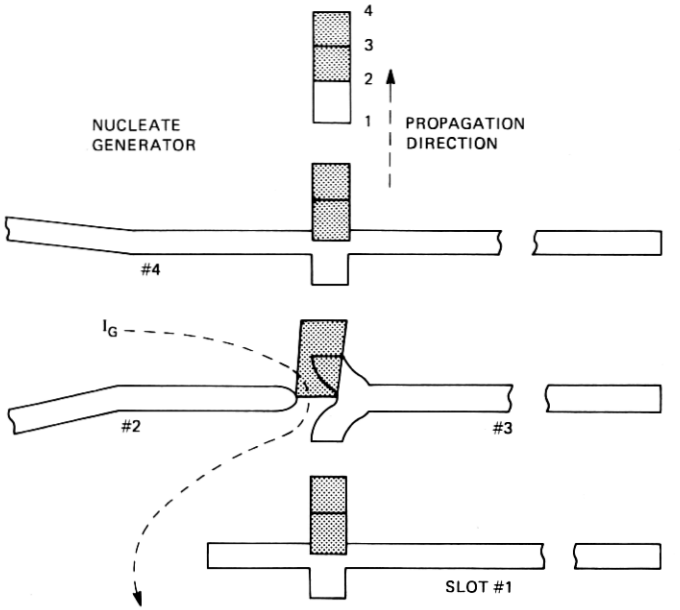

Fig. 44—A nucleate generator can be patterned as part of a conducting level. Slots guide the generator current but do not interfere with normal propagation. Bubbles are nucleated at the tip of slot #2.

The generator is incorporated into level 1 since that ensures the lowest possible generate current. Slots #2 and #4 funnel the generator current I_g from the input pad into the generator proper. A continuation of slot #4 acting in conjunction with slots #1 and #3 forms relatively high resistance paths so that most of the incident current I_g concentrates at the tip of slot #2, nucleating a bubble, before diffusing as it enters the chip area below.

Generator operation has been characterized in a nominally 8-μm period shift register processed on wafer B3954. The drive conditions were: amplitude 1.5 mA/μm, width 1.5 μs with 33 percent overlap. The generate pulse was applied in conjunction with propagate pulse 4. Subsequent propagate pulses move the newly generated bubble along the shift register track. Both adjacent and isolated domains were generated. The 200-ns wide generate pulse had an amplitude range of 230 to 360 mA.

The composite bias margins for generation at and propagation away from the generator were 19 Oe, with the lower end of the margin at stripout. For propagation through the generator, the margins reduce to 15 Oe with most of the margin loss at the low end. To ensure proper motion of bubbles as they pass upwards through the generator structure, a current density $J_{1,3}$ must be maintained between slots #3 and

#4. In our experiments, a single resistor diverted a fraction of the drive current $I_{1,3}$ into the generator pad.

7.5 Detection

Field-access permalloy devices use a chevron expander detector in which a bubble domain is stretched laterally before detection takes place in a magnetoresistance sensor. This approach has the advantage that it permits unlimited expansion without any effect on the data rate of the chip. The exit portion of the detector can be designed either to shrink the strip domain back to a bubble or to discharge the strip domain into a guard rail. The detector we report is similar to that just described and to a detector used with the bubble lattice.[8]

Bubble expansion and contraction is accomplished in the structure of Fig. 45. The analogy to a chevron expander structure is apparent. Factors relating J and $\bar{H}_z$ for an array of parallel conductor strips were introduced in Section III and are detailed further in Section X. In typical geometries, a current density $J = 4$ mA/μm generates a bias field decrement of nearly 20 Oe. In other words, stripout in the detector will be sustained over a 20-Oe range of the bias field. Since all the dual-conductor functions operate down to the strip-to-bubble transition field, we can expect to realize most of that bias field range.

Design curves to estimate the in-plane field H_x due to (*i*) the strip domain and (*ii*) the drive conductor strips are given in Figs. 46 and 47, respectively. At 8-μm period, assuming $4\pi M_s = 500G$ and $J = 4$mA/μm, we expect $H_x = 100$ Oe for a typical strip domain and a maximum field of 20 Oe (depends on detector-to-conductor strip positioning) from the drive conductors. The magnitude of these fields suggests that a thin-permalloy magnetoresistive sensor can be used. A photograph

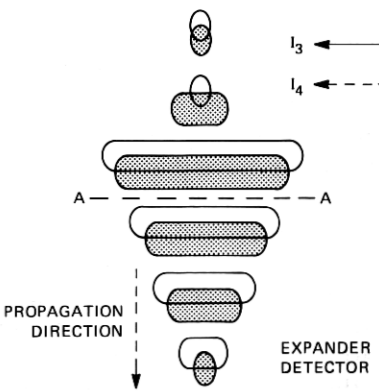

Fig. 45—Details of a dual-level expander detector. Bubbles, entering from the top, are expanded for either magnetoresistive or inductive sensing at A- -A.

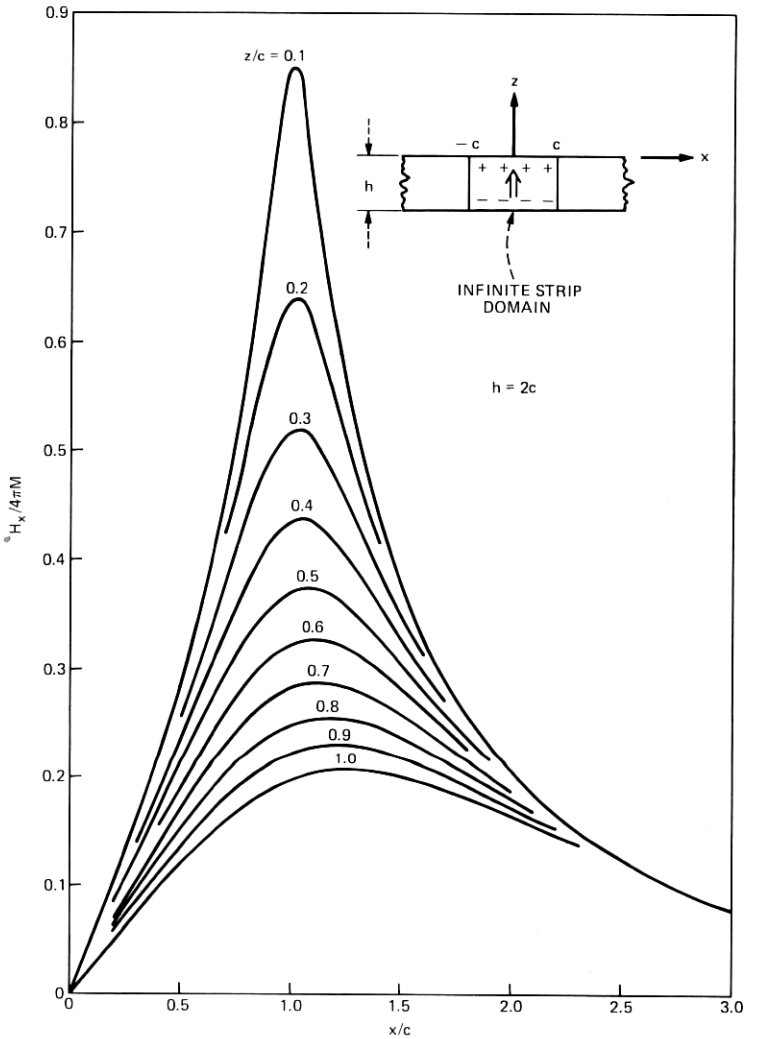

Fig. 46—Calculated in-plane field from a strip domain effective on a magnetoresistive sensor.

of the conductor-expander section complete with a "Chinese character" sensor is seen in Fig. 48. The sensor is processed on top of the pair of slotted conductor sheets.

In current-access devices, there is the opportunity to design a chip without permalloy. For example, if a strip domain is driven by an RF component of the bias field, the variation in the strip's flux can be sensed by a conductor pickup loop. This scheme is being pursued by J. M. Geary, and he has allowed us to present some of his preliminary

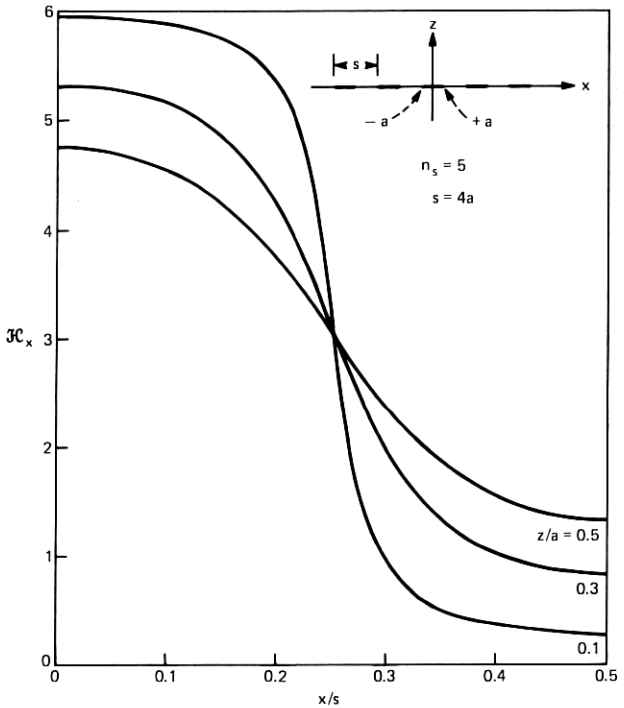

Fig. 47—Calculated in-plane field from the parallel drive strips of an expander detector.

results. A single-turn pickup loop 20 μm in length was patterned in a conducting sublayer at "A···A" of Fig. 45. An output signal of 5 μV was obtained when the width of a strip domain was modulated at 8 MHz (Fig. 49). RF detection in magnetic devices is not new and, in particular, we refer to an excellent article by Benrud et al., which deals with RF detection in thin permalloy-film memories.[16]

7.6 Transfer

Transfer is a particularly useful function since, combined with propagation, generation, and detection, it completes one set of functions that can be used to design a major-minor chip. This is significant, as it is well known that the major-minor organizations give improved performance over single loop shift registers. More important is that a dual-conductor major-minor chip can be partitioned into individually accessed regions with a resultant reduction in chip power dissipation.

One obvious way to implement a transfer is to use a "transfer" conductor patterned as part of a third conductor level to gate bubbles from minor storage loops to a major track and back again in much the

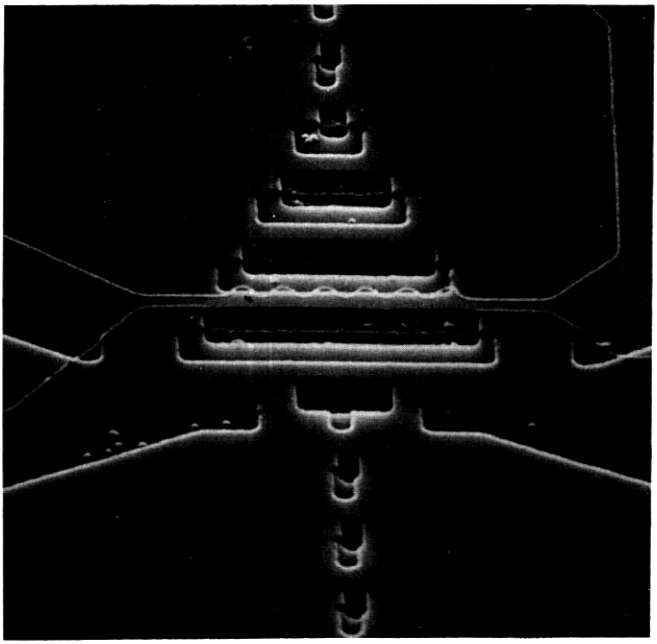

Fig. 48—An SEM photograph of an expander detector with a thin permalloy magnetoresistive sensor. The circuit period is 8 μm.

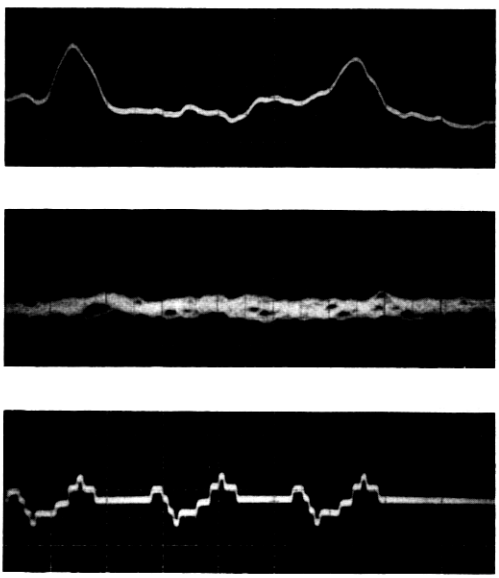

Fig. 49—Strip domains, excited by an 8-MHz RF signal, are detected in a single-loop. The raw signal, approximately 5 μv in amplitude, amplified and demodulated is shown in the upper trace. The bias field was taken above bubble collapse for the middle trace. A composite of the drive current is shown in the lower trace. Horizontal scale is 20 μs/div.

spirit of "field access" permalloy structures. However, perhaps one less processing level will be needed if the transfer can be accomplished within the framework of the propagate conductor levels themselves.

Such a compatible transfer gate can be realized by nesting apertures within one another as per the upper turn of the closed loop in Fig. 50. When this arrangement is used, it is only necessary to modify the propagation pulse sequence to cause bubbles in the transfer position to move into exit paths, whereas bubbles not in the transfer position are only idled backward and forward and always in a manner consistent with the retention of data when normal propagation resumes. Returning to Fig. 50, bubbles in the nine-step loop propagate clockwise with the standard pulse sequence [···12341234···]. However, a bubble located at the transfer position "1a" is transferred to position "4b" by the sequence [123412141234] in which the steps associated with the

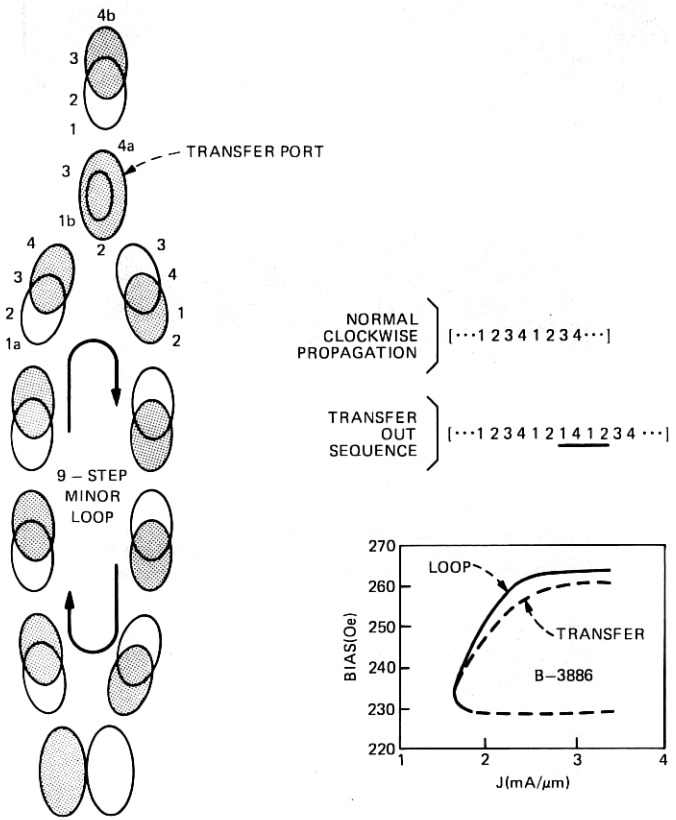

Fig. 50—Design and performance of a transfer port. In the transfer itself, the first level slot is nested within the slot of the second level. The propagation sequence is reprogrammed to transfer.

actual transfer have been underlined. It should be remembered that if data are to be preserved elsewhere, it is important to use only next number transitions in the transfer sequence.

Margins of propagation and transfer taken at 400 kHz are also included in Fig. 50. It can be seen that this transfer has very good margins indeed. More recent data have shown that, when the pulse which moves a bubble from 1b to 4a (4 in the underlined sequence) is lengthened by 0.25 μs, then an otherwise 1-MHz operation can be maintained. That is, only even-odd number transitions are permitted. ted.

7.7 Dual-conductor chip design considerations

There are two distinct aspects to the minimization of dissipation in dual-conductor devices. We discuss the minimization of power consumption on a local basis in Section 7.7.1 and on a chip basis in Section 7.7.2.

7.7.1 Optimization of conductor thickness

Power dissipation will always be a concern in current-access devices. For example, for $J = 1.5$ mA/μm, $\lambda = 8$ μm and $R = 0.1$ $\Omega/\square$, the continuous power dissipation is 14.4 μW/b. Even at $J = 1$ mA/μm and $\lambda = 4$ μm, the power dissipation is 1.6 μW/b. In this section, we turn to the problem of finding the correct thickness for conductors 1 and 2 under the constraint of an intervening insulator of thicknesses. From a practical standpoint, the insulator must withstand any voltage that exists between the two levels. The drive conductors are usually commoned at one end so that the maximum voltage encountered is the sum of the voltage drops of the layers. For the chip design discussed in the next section, the maximum inter-conductor voltage is 7.5 V.

For the purpose of calculating relative power consumption in a 2-conductor device, regard the fields produced by each level as those from an infinitesimally thin conducting sheet at the median plane of the actual conductor. For numerical work, the fields computed from eq. (25) will be used. When the two-conductor levels produce the same field, the relative power per unit area, normalized to the hole diameter $2a$, is

$$P = 2a/t_1\bar{\mathscr{H}}_1^2 + 2a/t_2\bar{\mathscr{H}}_2^2, \tag{10}$$

where t_1 and t_2 are the conductor thicknesses. The conductor of thickness t_1 is nearer the garnet. The two-conductor levels are separated by an insulator s units thick, as shown in Fig. 51. Values for P were computed at the maximum of $\bar{\mathscr{H}}$ near $r \approx a$ for $h/a = 0.8$ subject to the height constraint

$$a\tau = t_1 + s + t_2. \tag{11}$$

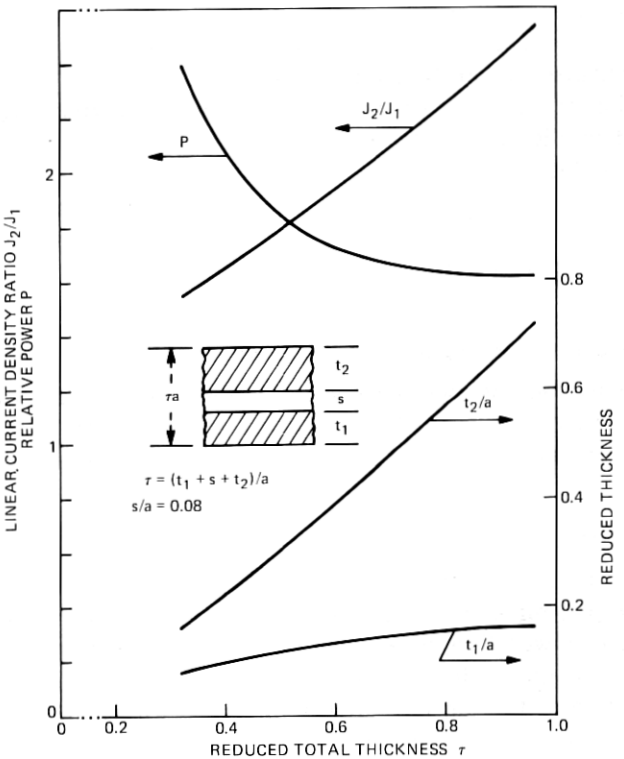

Fig. 51—Nomograph to determine the optimum thicknesses of levels 1 and 2 to minimize power dissipation in a dual-conductor circuit. Analysis based on a circular aperture of diameter $2a$ and garnet thickness $h = a$.

For each of several τ values, the minimum of eq. (10) was found. The results are shown in Fig. 51 together with the ratio of the current densities J_2/J_1 for the two levels. This ratio follows from the requirement of equal fields from the levels: $J_2/J_1 = \bar{\mathcal{H}}_1/\bar{\mathcal{H}}_2$.

The behavior of P as a function of τ represents a trade-off between efficient field production—$\bar{\mathcal{H}}$ large—and efficient power transmission in the conductor levels—t large. The best compromise between these conflicting requirements occurs for $\tau \approx 1$. The broad minimum of P about $\tau \approx 1$ permits a wide choice of τ with only minor changes in power consumption. For example, a 50-percent reduction of τ from 0.96 to 0.48 causes only a 16-percent increase in P. For current experimental devices, typical dimensions are $t_1 = 0.25$ μm, $s = 0.15$ μm, and $t_2 = 0.35$ μm. Using $a = 2$ μm, one finds $\tau = 0.38$. Although a larger value does reduce power consumption, it also increases processing complexity.

7.7.2 Design of a major-minor chip with partitioning

We now introduce partitioning of the conducting layers in a dual-conductor shift-register or major-minor chip design. In a partitioned chip, the main storage area and the major track are independently driven with a resultant reduction in chip dissipation. The shift-register and the major-minor chip layouts are very similar except that the shift-register uses parallel tracks rather than minor loops. Both of these designs allow for redundancy in the storage area. Given the functions of propagation, generation, annihilation, and transfer, the design of dual-conductor chips proceeds much as for field-access chips. There are, however, considerations peculiar to these current-accessed chip designs that we shall bring to your attention in this section.

The design and performance characteristics of a hypothetical major-minor chip with an 8-μm period and 262,144-b capacity is outlined in Fig. 52. Similar designs have been proposed by J. L. Smith and P. I. Bonyhard. Bubbles are assumed to move in bursts at a 1-MHz stepping rate. The chip is partitioned into independently accessed storage and detector-major track zones. The resistance everywhere is assumed to be 0.1 Ω/square. Each zone is driven at the current density indicated in the figure. If the entire chip was run continuously at 1 MHz, it would dissipate over 4 W. With partitioning, these zones can be independently accessed, reducing the chip dissipation substantially with no sacrifice in performance. In a partitioned chip it is, of course,

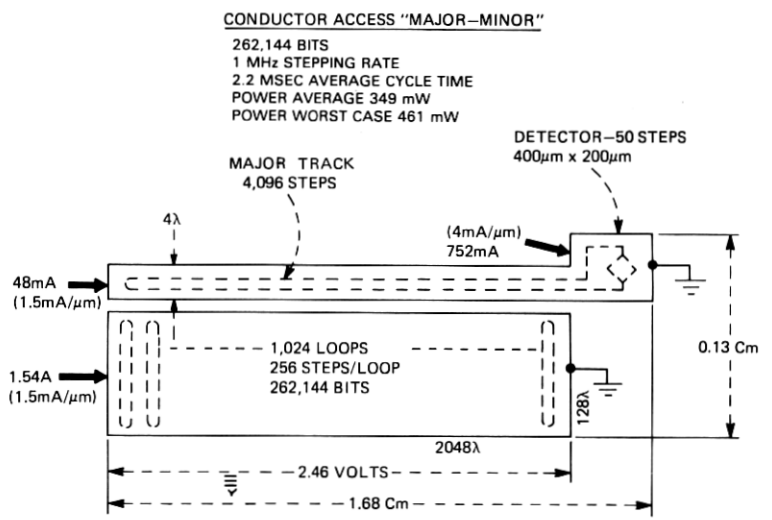

Fig. 52—Proposed design of a partitioned "major-minor" dual-conductor chip. The chip is made rectangular to increase the drive impedance and partitioned to permit selective drive to reduce the on-chip power dissipation.

necessary to move bubbles between zones. Propagation across slots was discussed with generators in Section 7.4.

It is desirable to make the impedance of the storage area compatible with driver circuitry. If the geometry of the storage area is laid out as a square, then it will present about 0.1 Ω resistance to its drivers—completely independent of the storage capacity. However, if the conductor sheet is reconfigured as a rectangle, its resistance can be "transformed" into a better match for semi-conductor drivers.

If the resulting "stick-like" chip is too awkward to handle, it can be folded, since the current (and bubbles) will have no difficulty negotiating the turns. A rectagular chip does have the advantage that it can dissipate heat more readily than a square chip and that it is well configured for a coilless package.

The number of minor loops is determined by noting that 1024 loops are, in binary multiples, the most that can be driven from a 5 V supply. This storage area would dissipate 3.77 W if driven continuously, but its duty factor is very low (0.03) so the average power dissipation is just 110 mW. The detector and major track do run essentially continuously; however, they together represent a very small fraction of the chip area and, in total, dissipate only 239 mW. As a result, the total chip dissipation is but 349 mW. Further information on cycle time, duty factor, and power dissipation is summarized in Table II. If the chip capacity is quadrupled (1024 b/loop), the chip dissipation would only double and the cycle times would remain about the same.

VIII. EPITAXIAL GARNET MATERIAL

In this section, we examine the material requirements for current-access bubble devices. The specific material parameters of particular importance to this technology are discussed and a garnet system proposed which allows relatively high-domain wall mobility along with adequate uniaxial magnetic anisotropy.

8.1 Growth and characterization

All compositions grown for the current-access high-density bubble devices were grown on $Gd_3Ga_5O_{12}$ substrates by the LPE dipping

Table II—Characteristics of partitioned 262-kbit dual-conductor chip

Zone	Steps	Transit Time (ms)	Average Case			Worst Case		
			Cycle Time	Duty Factor	Power (mW)	Cycle Time	Duty Factor	Power (mW)
Minor loops	256	0.256	0.128	0.03	110	0.256	0.06	230
Major track and detector	4146	4.146	4.146	0.97	239	4.146	0.94	231
			4.274	1.00	349	4.402	1.00	461

technique using supercooled melts.[17] Axial rotation was maintained constant at approximately 100 rpm during the growth period. The details of the apparatus and growth techniques have been discussed elsewhere.[18-21] Growth temperatures were restricted to 875 ± 60°C. Lattice parameter measurements were obtained using the HPM method.[22] Magnetic property measurements were obtained using the standard techniques.[23-25]

8.2 Material properties

Table III lists the parameters which must be considered when designing a material to be used in dual conductor-current access devices. Items 1 to 11 in Table III are important parameters to be considered when designing a bubble material for use in most bubble circuit technologies. Items 11 to 13 are of particular importance for dual conductor-current access devices. Because of the high-speed performance inherent in this technology, the mobility of the bubble material is of primary importance. Dynamic coercivity and bubble propagation angle are two other parameters that become increasingly important in small bubble devices. Low dynamic coercivities allow lower drive currents to be used for bubble propagation. A discussion of the importance of the bubble propagation angle is presented in Section 7.3. An approach to increasing the mobility while maintaining adequate q values as well as an approach to lowering the dynamic coercivity is presented later in this section.

Epitaxial garnet films of nominal composition $Y_{1.2}Sm_{0.4}Lu_{0.5}Ca_{0.9}Ge_{0.9}Fe_{4.1}O_{12}$ have been shown to be useful in 16-μm period field-access bubble devices.[26] For 3-μm diameter bubbles, this composition offers the advantages of domain wall mobility slightly in excess of 250 cm s^{-1} Oe^{-1} along the q values of 5 and precise control of the temperature dependence of the magnetic properties by the appropriate adjustment of melt chemistry. Figure 53 shows the material length

Table III—Material parameters for current-access devices

1. Saturation magnetization, $4\pi M_s$ (*Gauss*)
2. Exchange constant, A (ergs cm^{-1})
3. Uniaxial anisotropy, K_u (ergs cm^{-3})
4. Material length parameter, $l(\mu m)$
5. Anisotropy field, H_K (Oe)
6. Quality factor, q (dimensionless)
7. Bubble collapse field, H_{col} (Oe)
8. Lattice parameter, L.P. (Å)
9. Magnetostriction coefficient, λ_{111}, λ_{100}
10. Temperature dependence of H_{col}, (% $°C^{-1}$)
11. Bubble mobility, μ (cm/sec-Oe)
12. Dynamic coercivity, ΔH_c (Oe)
13. Bubble propagation angle, ψ (degrees)

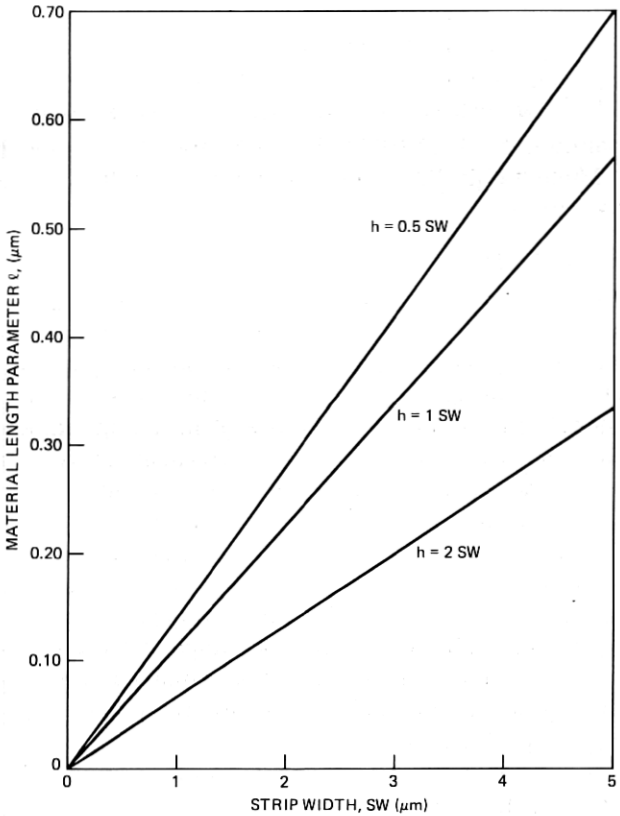

Fig. 53—Material length parameter (l) vs strip width (sw) with the thickness-to-strip-width ratio as a parameter.

parameter (l) as a function of domain strip width (sw) with the thickness-to-strip-width (h/sw) ratio as a parameter. Depending upon the h/sw ratio, the l parameter needed for a strip width of 1.7 μm ranges from 0.115 to 0.235 μm. For the case of h/sw = 1, the material length parameter must be 0.191 μm.

Extending the $(YSmLuCa)_3(FeGe)_5O_{12}$ system to smaller bubbles results in the nominal composition $Y_{1.0}Sm_{0.5}Lu_{0.7}Ca_{0.8}Ge_{0.8}Fe_{4.2}O_{12}$ which exhibits 1.7-μm diameter bubbles and the properties listed in Table IV. Materials grown from the general system $(YSmLuCa)_3(FeGe)_5O_{12}$ have exhibited dynamic coercivities ranging from 1.4 Oe to 3.2 Oe. The higher coercivities being measured are on the larger anisotropy materials, supporting smaller diameter bubbles. Because of the particular importance of bubble mobility in the current-access technology, a technique was needed to maintain a q value of

approximately 3 to 4 for materials exhibiting an l value of 0.16 to 0.19 μm while also increasing the domain wall mobility.

It would be advantageous to be able to decrease the samarium content of the composition listed in Table IV while maintaining the q value, which would result in an increased mobility. One approach to achieving this is to increase the concentration of the most "anisotropy active" constituents. Figure 54 shows the calculated uniaxial anisotropy as a function of the lutetium content of garnet compositions in the three systems $(YLuSmCa)_3(FeGe)_5O_{12}$, $(LaLuSmCa)_3(FeGe)_5O_{12}$, and $(LaLuSm)_3(FeGa)_5O_{12}$. The samarium content and the Curie temperature are used as parameters. Curves A through C are calculated for Ca-Ge substitution of ~0.8 moles per garnet formula unit and a Curie temperature of ~480°K. Curves D and E represent gallium substitution leading to a Curie temperature of ~440°K. We point out that the curves shown in Fig. 54 do not take into account the lattice constant constraint usually imposed on epitaxial garnet films. The compositions required to achieve a lattice constant match with $Gd_3Ga_5O_{12}$ (GGG) substrates (12.383Å) are indicated by the point on each curve marked L.M. Comparison of curves A and B in Fig. 54 reveals that, to decrease the samarium content from 0.5 to 0.3 in the garnet formula and maintain both the anisotropy of ~35000 ergs-cm^{-3} and a lattice parameter match with the GGG substrate, compositions outside the $(YLuSmCa)_3(FeGe)_5O_{12}$ system must be considered. Curve C indicates that the $(LaLuSmCa)_3(FeGe)_5O_{12}$ system allows both the uniaxial anisotropy of ~35000 ergs-cm^{-3} and a lattice match to be achieved. A discussion of the advantages of lanthanum have been presented elsewhere.[27]

It is well known that materials with high $4\pi M_s$ require relatively little diamagnetic ion substitution. The advantages realized in the divalent-tetravalent ion substitution system can be obtained with less complicated crystal compositions when high moment material is required.[28] For materials exhibiting a high $4\pi M_s$, Ca^{2+}-Ge^{4+} substitution could result in too high a Curie temperature making it difficult to

Table IV—Composition:
$Y_{1.0}Sm_{0.5}Lu_{0.7}Ca_{0.8}Ge_{0.8}Fe_{4.2}O_{12}$

Lattice parameter	12.383 Å
$4\pi M_s$	510 G
K_u	36,600 ergs cm^{-3}
l	0.19 μm
A	2.7×10^{-7} ergs cm^{-1}
H_k	1800 Oe
q	3.5
μ	~300 cm/S-Oe
ΔH_c (dynamic coercivity)	3.0 Oe

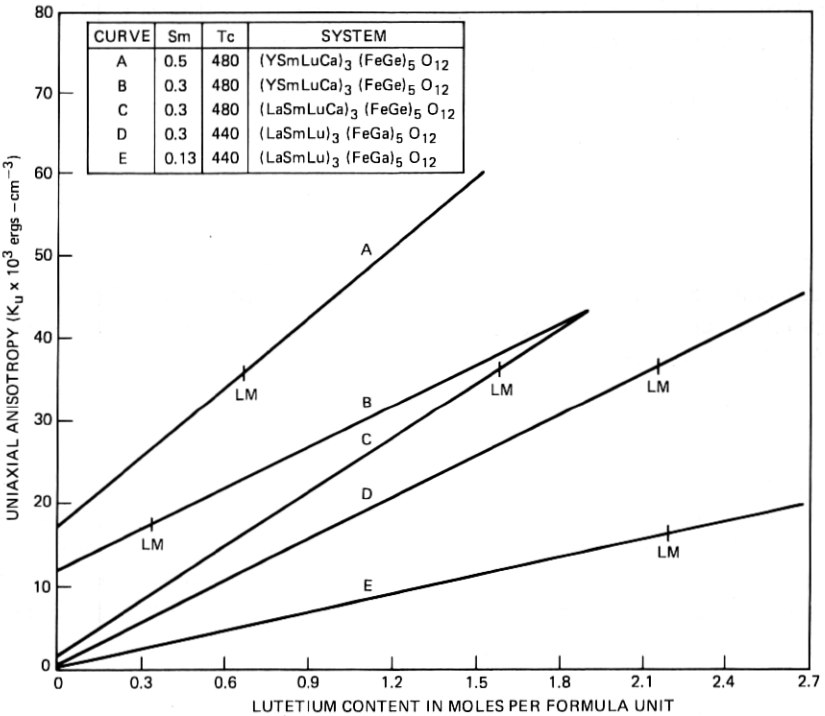

Fig. 54—Calculated uniaxial magnetic anisotropy vs lutetium content for the systems $(YSmLuCa)_3(FeGe)_5O_{12}$, $(LaSmLuCa)_3(FeGe)_5O_{12}$, and $(LaLuSm)_3(FeGa)_5O_{12}$. The samarium content and the Curie temperature are varied. The GGG lattice matching compositions are indicated by the symbol LM on each curve.

control the temperature dependence of the magnetic properties to match the barium ferrite bias magnets.

A slight imbalance of the divalent-tetravalent ion ratio could also result in increased coercivity. The immersion of a gallium garnet substrate into a melt supersaturated with an iron garnet containing Ca^{2+}–Ge^{4+} might be expected to show increased substrate dissolution prior to initial film growth as compared to the same substrate immersed in a melt supersaturated with a gallium containing iron garnet. Considering the complications in melt chemistry and the careful control of growth conditions necessary to minimize compositional fluctuations in Ca^{2+}–Ge^{4+} substituted garnets, a move to simpler film compositions would be advantageous.

Curve D illustrates the anisotropy calculated for the $(LaLuSm)_3(FeGa)_5O_{12}$ system. Note that the lattice match composition occurs at a lutetium concentration of ~2.15 moles per garnet formula unit and that a uniaxial anisotropy of ~35000 ergs-cm^{-3} can be obtained. Table V lists a nominal composition in the

$(LaLuSm)_3(FeGa)_5O_{12}$ system along with some measured magnetic properties. Curve E shows that lowering the samarium concentration to 0.13 moles per garnet formula unit results in a significantly lower anisotropy for the GGG lattice matching composition.

8.3 Dynamic coercivity

The dynamic coercivity of epitaxial bubble garnet films supporting ~1.7-μm diameter bubbles has been measured as a function of film thickness.[29] Figure 55 shows the dynamic coercivity measured by a bubble translation technique as a function of inverse film thickness. All curves are for material exhibiting 1.7-μm diameter bubbles. Curve C is for a sample in the $(YLuSmCa)_3(FeGe)_5O_{12}$ system, while curves A and B represent two compositions in the $(LaLuSm)_3(FeGa)_5O_{12}$ system. Curve A is for a samarium concentration of ~0.13 moles per garnet formula unit, while curve B represents data taken on a sample containing a samarium concentration of 0.3 moles. Note that the gallium material exhibits significantly lower dynamic coercivities than does the Ca^{2+}-Ge^{4+} substituted material.

8.4 Melt chemistry

The phase equilibria observed in the $(YSmLuCa)_3(FeGe)_5O_{12}$ system have been presented previously.[19] Lanthanum does not form an iron garnet, and lutetium iron garnet has been reported being grown only once in bulk form,[30] possibly because of phase equilibria difficulties. As the concentration of lanthanum increases in the pseudo-ternary Flux—Fe_2O_3—$\sum Ln_2O_3$, the garnet phase field would be expected to narrow considerably. Figure 56 shows a section of the pseudo-ternary Flux—Fe_2O_3—$\sum Ln_2O_3$, where $\sum Ln_2O_3$ corresponds to the sum of La_2O_3+Lu_2O_3. The ratio of La_2O_3/Lu_2O_3 was fixed at 0.332 to allow stress-free epitaxial film growth on GGG substrates. Note that all data shown in the pseudo-ternary are for unsubstituted iron garnets. Substitution of diamagnetic ions could be expected to shift the location of the phase boundaries. Addition of gallium results in the garnet-perovskite boundary being displaced towards the Flux—Fe_2O_3 binary. Depending on the overall garnet oxide concentration in the melt, the

Table V—Composition: $La_{0.6}Lu_{2.1}Sm_{0.3}Ga_{0.9}Fe_{4.1}O_{12}$

$4\pi M_s$	466G
K_u	35,500 ergs cm^{-3}
A	2.0×10^{-7} ergs cm^{-1}
l	0.18 μm
H_K	1915 Oe
Q	4.1
μ	500–1000 cm/S-Oe
ΔH_c (dynamic coercivity)	~2 Oe

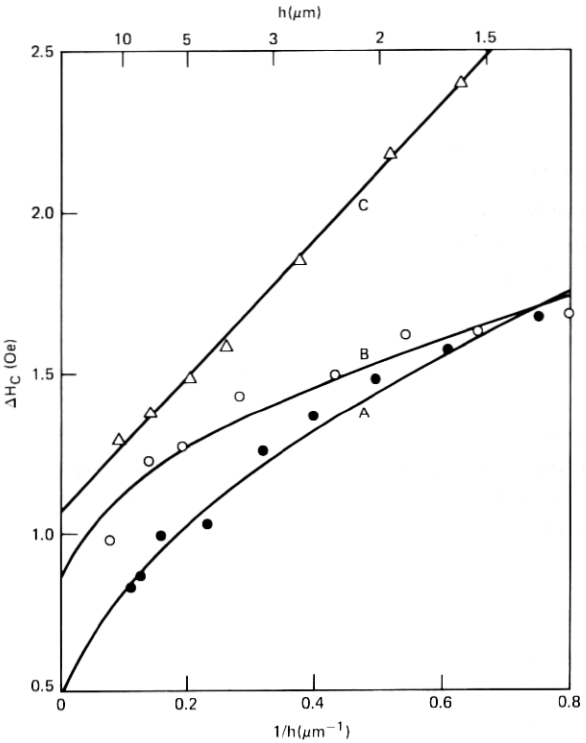

Fig. 55—Bubble dynamic coercivity (ΔH_c) as a function of inverse film thickness for 1.7-μm bubble material. Curve C is for $(YLuSmCa)_3(FeGe)_5O_{12}$. Curves A and B represent two compositions in the system $(LaLuSm)_3(FeGa)_5O_{12}$. Curve A is for a samarium concentration of ~0.13 moles per garnet formula unit. Curve B represents data on a sample containing 0.3 moles of samarium.

range of $Fe_2O_3/\sum Ln_2O_3$ over which garnet is found to be the primary phase field is from 6 to 9. For comparison, the Fe_2O_3/Y_2O_3 ratio range for garnet in the Flux—Fe_2O_3—Y_2O_3 pseudo-ternary is from 12 to 40.

Because of the large size of La^{3+}, one would expect a relatively low value for the La^{3+} distribution coefficient. The definition for the distribution coefficient of lanthanum is:

$$k^{La} = \frac{\left(\frac{La}{La+Lu+Sm}\right)_{crystal}}{\left(\frac{La}{La+Lu+Sm}\right)_{melt}},$$

where the symbols in the fractions represent the number of moles present. Although the value for the effective coefficient will be rate-dependent, the value for k^{La} under average growth conditions is found to be ~0.42.

The use of compositions in the $(LaLuSm)_3(FeGa)_5O_{12}$ system allows less complicated crystal compositions to be used. Lower dynamic coercivities and increased domain wall mobility can be obtained.

IX. PROCESSING

There are two major concerns in processing dual conductor structures. First, the two conductors should both be as close as possible to the epitaxial film supporting the bubbles. Hence, a prespacer (analogous to the prespacer used between conductor and epitaxial layer in standard field access devices) should be as thin as possible or completely omitted. In addition, it is immediately obvious that the dielectric layer between the conductors must be as thin as the limits of dielectric breakdown permit. Second, the very small period devices possible within the material constraints of this technology will require increasingly precise control for etching the fine-aperture metal film pattern. What is required is an etching method that will produce metal patterns dimensionally identical to the etch mask.

9.1 Material requirements

9.1.1 Insulating films

If a prespacer is used, the material and/or process selection is quite unrestrained as the surface is completely planar and the layer thickness

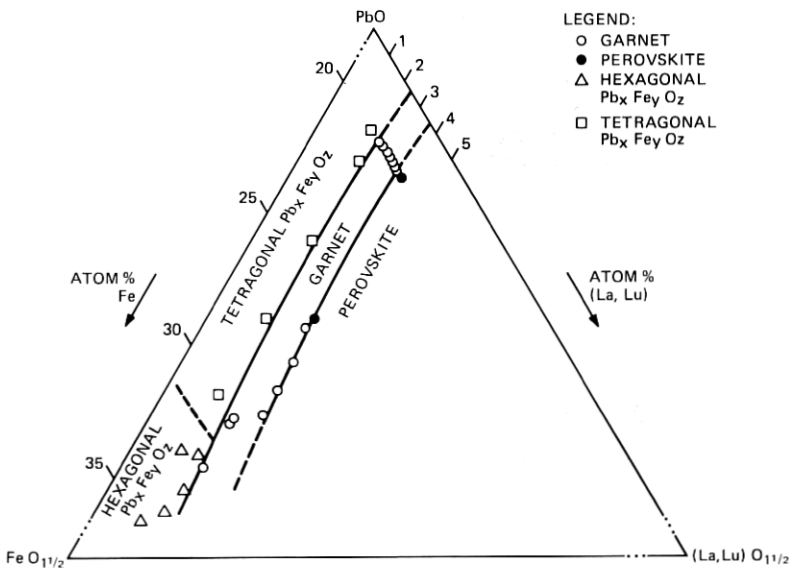

Fig. 56—A section of the pseudoternary Flux—Fe_2O_3—ΣLn_2O_3, where ΣLn_2O_3 represents La_2O_3 + Lu_2O_3.

required is very small. Thus, several avenues can probably be used: RF diode-sputtered SiO_2 or SiN; RF magnetron or S-gun deposited SiO_2 or SiN; plasma-deposited or CVD-deposited SiO_2 or SiN. In all the work reported, prespacers were SiO_2 deposited by RF plasma deposition using an Applied Materials Plasma I radial flow system.

The insulating layer between conductors has more stringent requirements due to the multiplicity of crossovers and the need for minimum thickness. Thus, very good dielectric properties are required and a process that deposits a conformal coating is mandatory, i.e., equivalent deposition rates on vertical and horizontal surfaces are required (Fig. 57). Higher-pressure processes such as plasma-deposition or CVD are clearly preferred over line-of-sight deposition methods such as evaporation or sputtering. A relatively low-temperature (c.f. 250 to 280°C) plasma SiO_2 deposition process has been developed using the Applied Materials Plasma I apparatus.[31] Dual conductor circuits fabricated using the plasma-SiO_2 insulator exhibit breakdown potentials equivalent to those expected for high-quality, thermally grown SiO_2 films of an equivalent thickness. We thus conclude that the step coverage over the dual conductor features is optimal.

9.1.2 Conductor materials

Though any highly conductive metal alloy system may be used, Al or Au alloys appear quite suitable, and most of the work reported has

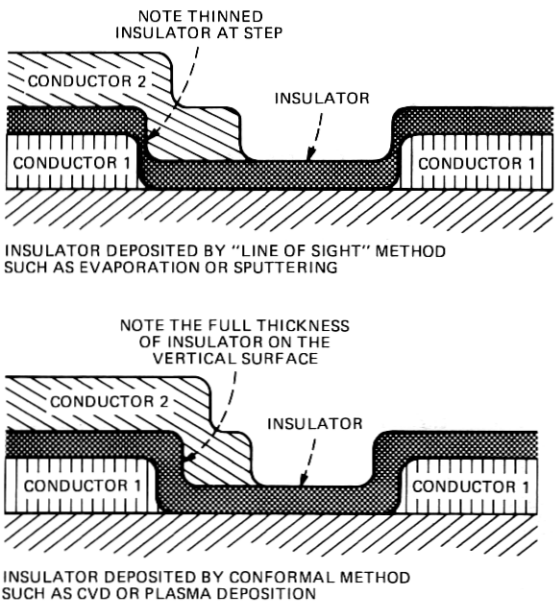

Fig. 57—Effect of conformal vs line-of-sight deposition on insulating film thickness at crossovers.

used Al alloys with low copper content (0.7 to 4 percent). The AlCu alloys are particularly suited because the relatively high current density required for some functions in the dual conductor circuits ($>10^5$ A/cm^2) indicates the use of conductor materials with low electromigration rates. The AlCu alloys have been evaporated using a standard e-gun source and planetary wafer fixturing to maximize step coverage. It is advantageous to carry out this deposition at as low a substrate temperature as possible to prevent stress buildup in the AlCu films.[32]

9.2 Metal patterning

9.2.1 Photolithography

Standard contact-print photolithography was used on devices reported here.[33] We anticipate that other high-resolution methods such as projection printing, X-ray exposure, etc. may be used equally well.

9.2.2 Metal patterning

In standard rotating magnetic field-access bubble devices, the Al conductor layer is relatively simple, and at least for 16-μm period circuits can be etched with standard wet chemical methods. In dual conductor-accessed circuits, however, wet-etch processes are unusable in small period circuits due to the undercutting of the photoresist pattern by the isotropic etch process. This undercutting severely limits the dimensions achievable in conductor patterning. In fact, since these circuits will invariably require that near state-of-the-art resolution be reproduced in the resist mask, no isotropic process or process which biases the conductor line or space dimensions with respect to the photoresist pattern should be used. In the following section, we describe a plasma-etching process that does indeed exactly reproduce the etch mask in the Al film. It is conceivable that other methods may be used, such as the planar anodization method described by D. K. Rose.[34]

For an etch patterning process, very high material etch selectivity will be required. If no prespacer is used, the first-level etch process cannot be allowed to cut into the epitaxial garnet film and thin it selectively. Similar constraints operate when etching the second conductor, since any thinning of the underlying insulator layer will obviously reduce the dielectric breakdown strength between the two conductors. Plasma etching is an obvious choice to satisfy the requirements for etching Al alloy films for high-density dual conductor circuits for the following reasons: (*i*) plasma etching uses a chemical process to remove metal and very high etch selectivity can be achieved for different materials, (*ii*) careful selection and control of plasma process parameters can replicate photoresist patterns in aluminum films without measurable (<0.1 μm) dimensional variation. (A good survey of plasma etch processes can be found in Refs. 35 and 36.)

The particular RF (13.56-MHz) plasma process adapted is based on one developed by D. Wang, et al.[37] The apparatus used was designed by C. J. Mogab and F. B. Alexander,[38] and the etch chamber is shown schematically in Fig. 58. The basic etch process involves the following reaction:

$$Al(s) + 3Cl(plasma) \rightarrow AlCl_3(solid)$$

followed by volatilization of the $AlCl_3$ solid

$$2AlCl_3(solid) \rightarrow (AlCl_3)_2(gas).$$

There is evidence that the anisotropic etch process is promoted by the impact of charged particles on the horizontal surface (Fig. 59).

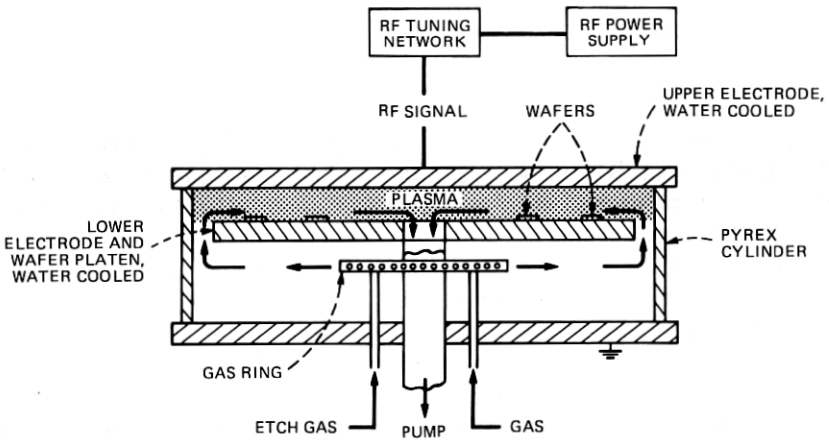

Fig. 58—Radial flow plasma etch apparatus.

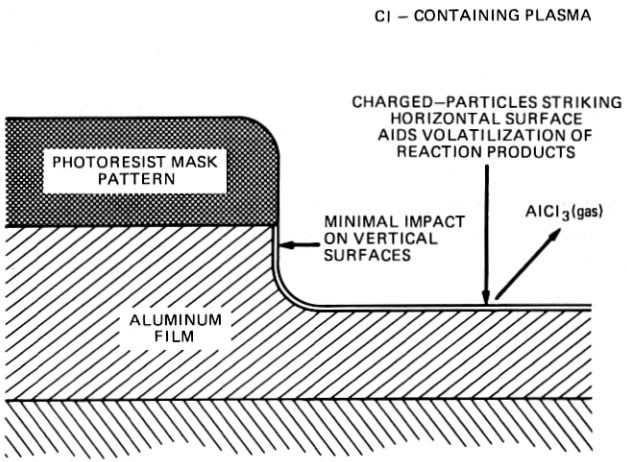

Fig. 59—Schematic of anisotropic etch process.

Obviously, a bias-free etching process will produce near-vertical walls on the metal patterns, which might pose problems in the crossover features in the dual conductor circuits. To date, the combination of conformal plasma SiO_2 and good step coverage in the Al evaporation process have minimized the potential problems, both with respect to dielectric breakdown and also propagate drive margin reduction, which might be caused by high-resistance crossovers. Figures 60 to 63 are SEM photographs of plasma-etched, dual-conductor patterns. Figure 60 shows a horizontal, straight-line propagate path, while Figure 61 shows several vertical loops. Figure 62 shows one of the generator designs tested. Figure 63 shows, at the same magnification, three data storage loops designed and fabricated within identical linewidth and alignment tolerances. The three loops are of 8-, 6-, and 4-μm period.

X. MAGNETIC FIELDS AND BUBBLE MOTION

Early conductor-drive devices[39,40] confined currents to discrete conductor lines narrower than a bubble diameter. The present approach to conductor propagation distributes current over a conducting sheet with openings which provide the necessary spatial variations of magnetic field. To furnish some insights and a design aid for conductor-access propagation, two simple geometries—parallel conducting stripes

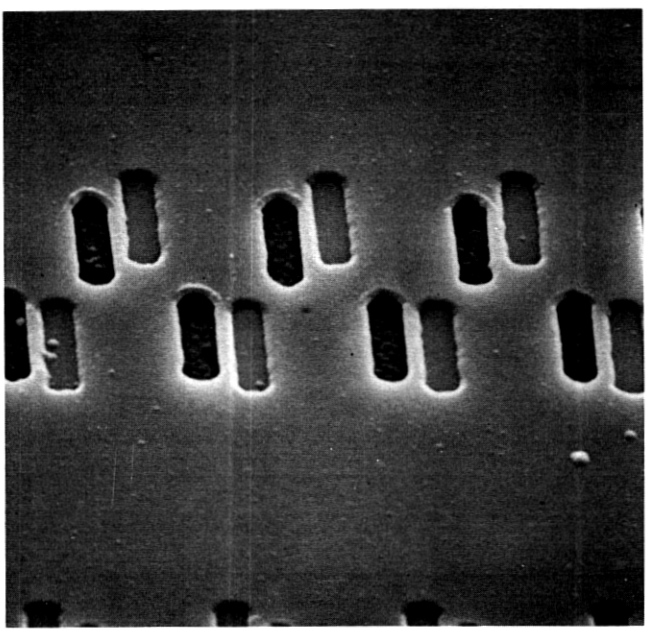

Fig. 60—An SEM of an 8-μm period dual-conductor propagate pattern. The darker apertures are in the first conductor and the lighter in the second conductor pattern. These apertures were etched in the AlCu alloy by a plasma etch technique using a Cl-containing gas (2860X).

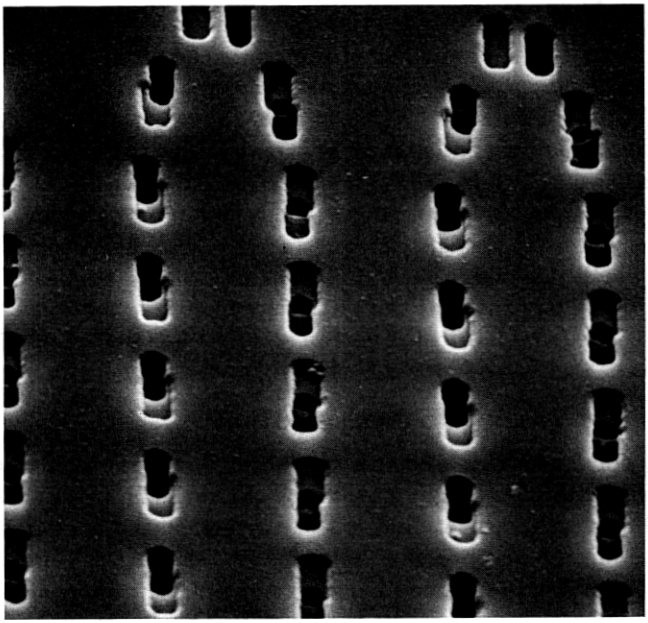

Fig. 61—An SEM of 8-μm memory storage loops (2200X).

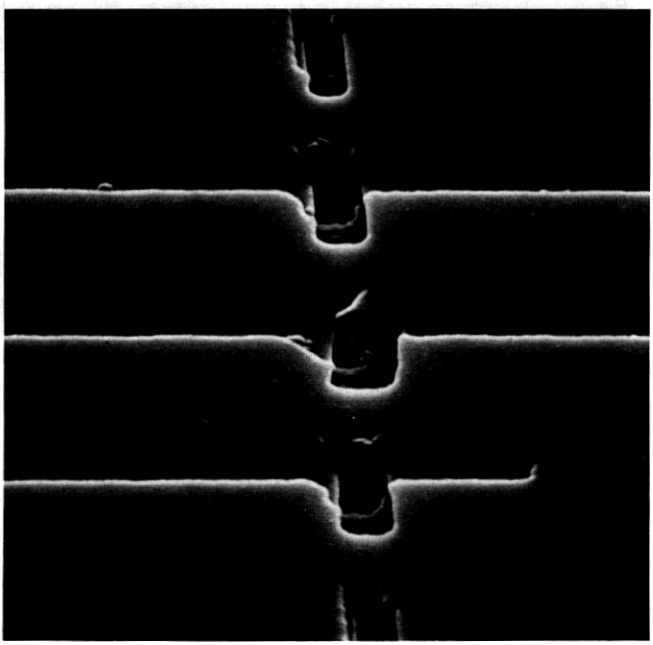

Fig. 62—An SEM of an experimental generator pattern plasma etched in AlCu (3160X).

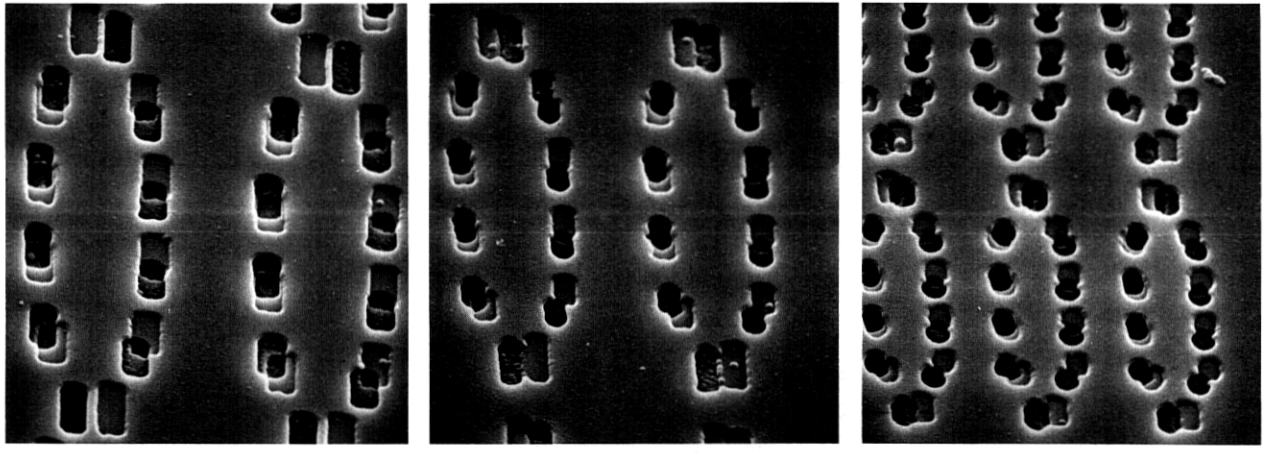

(a) (b) (c)

Fig. 63—Data storage loops plasma etched in AlCu films. The three patterns follow identical dimensional design rules (2870X). (a) 8-μm period; (b) 6-μm period; (c) 4-μm period.

and a circular hole in an infinite conducting sheet—were investigated. Bubble motion in a gradient field was also studied.

10.1 Stripe conductors

Consider an infinitesimally thin conducting sheet in the plane $z = 0$. From this sheet, infinite in the y direction, remove material to form conducting stripes of width $2a$ and spacing $s > 2a$; see Fig. 64. Each stripe carries a current $I = -2aJ_o$ in the y direction, where J_o is the constant linear current density of each stripe. In MKS units, the contribution[41]

$$H_z(n) = (J_o/2\pi) \ln[r_2(n)/r_1(n)] \tag{12}$$

of the nth stripe to the z component of the field intensity may be expressed in dimensionless form by the quantity

$$\mathcal{H}_s(n) = \frac{4\pi H_z(n)}{J_o} = \ln\left[\frac{(\xi + \alpha - n\sigma)^2 + \zeta^2}{(\xi - \alpha - n\sigma)^2 + \zeta^2}\right], \tag{13}$$

where the lengths $r_1(n)$ and $r_2(n)$ are defined in Fig. 64, $\xi = x/h$, $\zeta = z/h$, $\alpha = a/h$, and $\sigma = s/h$. For bubble propagation, one is interested in the average intensity

$$\bar{\mathcal{H}}_s(n) = h^{-1} \int_{z_s}^{z_s+h} H_z(n)\, dz, \tag{14}$$

where z_s is the garnet-conductor separation and h the garnet-film thickness. After integrating eq. (14) and summing over the stripes, one finds

$$\bar{\mathcal{H}}_s = \sum_n \sum_{j=1}^{2} (-1)^j [\zeta_j \ln A_{nj} + 2\beta_j(n) \text{Arctan } C_{nj}], \tag{15}$$

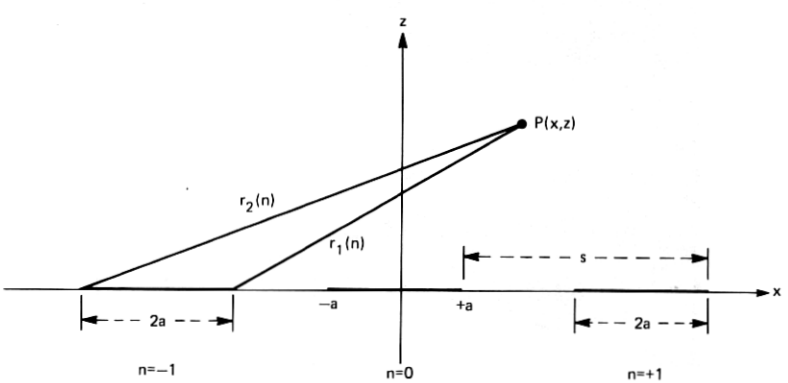

Fig. 64—Coordinate system for an array of infinite conducting stripes. The conductors, $2a$ units wide and spaced s units apart, occupy the plane $z = 0$. Each stripe extends to infinity in the $\pm y$ directions, carries a current I, and bears an index n.

where

$$\mathcal{H}_s = 4\pi \bar{H}_z / J_o = \text{dimensionless average intensity},$$

$$\bar{H}_z = \sum_n \bar{H}_z(n) = \text{average intensity},$$

$$\zeta_1 = z_s/h, \qquad \zeta_2 = \zeta_1 + 1, \qquad \beta_j(n) = \xi + (-1)^j \alpha - n\sigma,$$

$$A_{nj} = [\zeta_j^2 + \beta_2^2(n)]/[\zeta_j^2 + \beta_1^2(n)],$$

$$C_{nj} = \beta_j(n)/[\beta_j^2(n) + \zeta_1\zeta_2].$$

When the number of stripes is small, say, less than 100, the best way to evaluate eq. (15) is by programming the right-hand side as it stands. As the number of stripes n_s is increased, this procedure becomes less attractive because $2n_s$ evaluations of the logarithm and arctangent functions are needed for each value of x. Note that, for $n_s < \infty$, $\bar{\mathcal{H}}_s$ is not periodic; for a complete numerical description of eq. (15) in the vicinity of the stripes, the number of function evaluations is $2n_x n_\alpha n_s^2$, where n_x is the number of points per period s and n_α the number of α values of interest.

When n_s is large, say, $n_s > 100$, the behavior of $\bar{\mathcal{H}}_s$ near the array center may be approximated by an infinite number of stripes. This choice permits a significant reduction in computation time but fails to give information about the behavior near the array edges—a matter that will be investigated separately. As $n_s \to \infty$, the dimensionless average intensity, regarded as a function of ξ, has the properties

$$\bar{\mathcal{H}}_s(\xi) = \bar{\mathcal{H}}_s(\xi + \sigma) \quad \text{and} \quad \bar{\mathcal{H}}_s(-\xi) = -\bar{\mathcal{H}}_s(+\xi). \tag{16}$$

Consequently, one can restrict evaluation of $\bar{\mathcal{H}}_s$ to the points $0 \leqslant \xi \leqslant \sigma/2$. Equation (16) implies $\bar{\mathcal{H}}_s(0) = \bar{\mathcal{H}}_s(\sigma/2) = 0$. This result may also be deduced from symmetry considerations. For an origin at the center of an opening between stripes, the same symmetry arguments require $\bar{\mathcal{H}}_s$ to be antisymmetric about this origin. For numerical evaluation of $\bar{\mathcal{H}}_s$ in the limit $n_s \to \infty$, eq. (15) was rewritten as

$$\bar{\mathcal{H}}_s = \mathcal{H}_1 + \mathcal{H}_2, \tag{17}$$

where

$$\mathcal{H}_1 = \sum_{j=1}^{2} (-1)^j \zeta_j \Bigg[\ln A_{oj} + \sum_{n=1}^{N} [\ln A_{nj} A_{-nj}] - (8\alpha\xi/\sigma^2) \Bigg[\zeta(2) - \sum_{n=1}^{N} n^{-2} \Bigg] - [8\alpha\xi(\xi^2 + \alpha^2 - 3\zeta_j)/\sigma^4] \Bigg[\zeta(4) - \sum_{n=1}^{N} n^{-4} \Bigg] \Bigg],$$

$$\mathcal{H}_2 = 2 \sum_{j=1}^{2} \sum_{n=-N}^{+N} [(-1)^j \beta_j(n) \text{Arctan } C_{nj}]$$

$$- [16\alpha\xi(\zeta_2^3 - \zeta_1^3)/\sigma^4] \left[\zeta(4) - \sum_{n=1}^{N} n^{-4} \right],$$

$\zeta(k)$ = Riemann zeta function.[42]

Equation (17) adds the contributions from the $2N + 1$ stripes nearest the origin as they stand in eq. (15) to the contribution from the remaining stripes approximated by a truncated series in the inverse powers of the stripe index n. Since the leading term in the power series

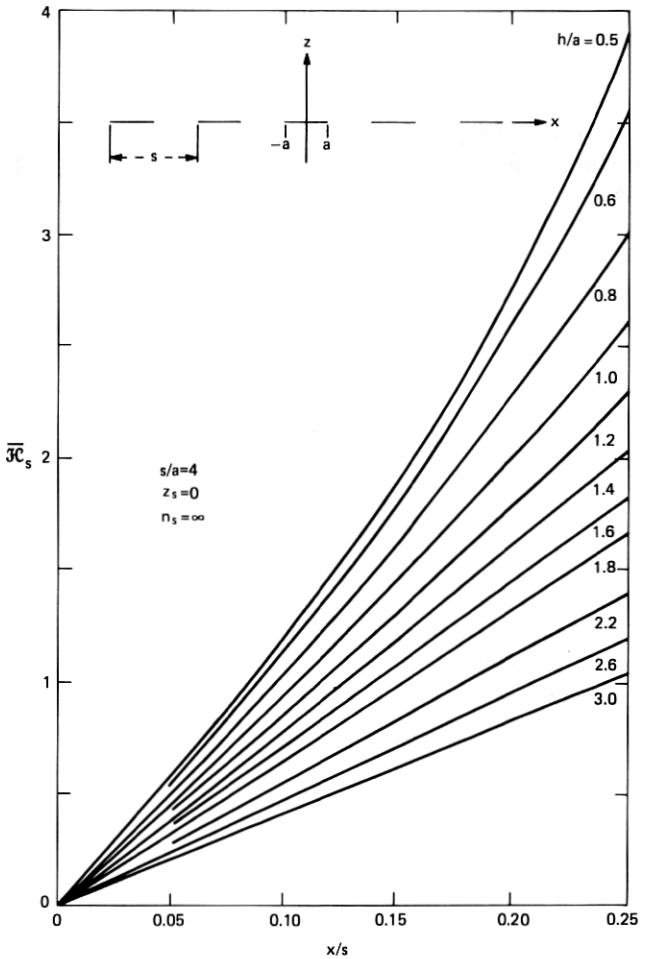

Fig. 65—Dimensionless average value $\overline{\mathcal{H}}_s$ of the z component of magnetic field as a function of x/s. The curves are graphs of eq. (17) for $s = 4a$ and $z_s = 0$. The ordinate $\overline{\mathcal{H}}_s$ is numerically equal to the field in oersteds when the linear current density of each stripe is 1 mA/μm.

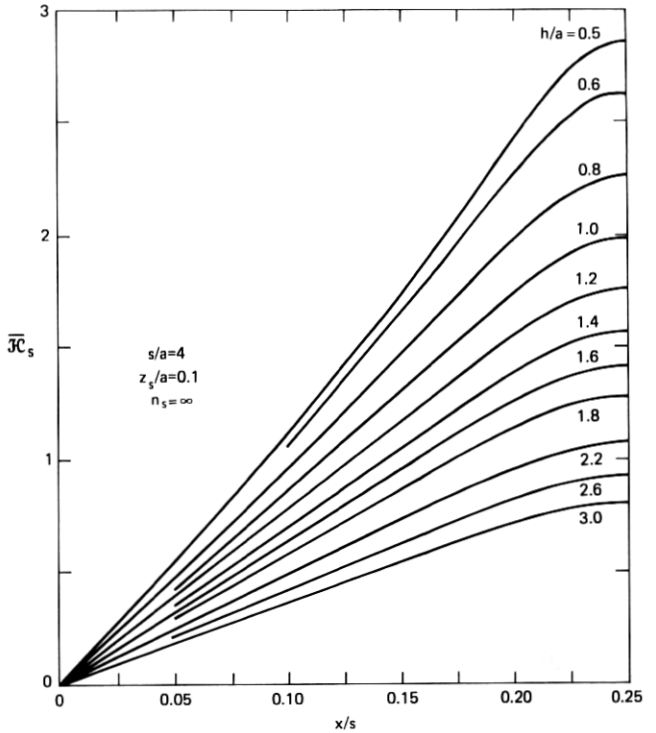

Fig. 66—Same as Fig. 65, except $x_s = 0.1a$.

is n^{-2}, the field at the origin due to a pair of stripes, remote from and symmetric about the origin, decreases as the inverse square of the distance of either stripe from the origin. Accuracy requirements determine N. For the choice $N = 10$, used in the computations presented here, the estimated error in $\bar{\mathcal{H}}_s$ is less than 10^{-5}. Figures 65 to 69 show graphs of $\bar{\mathcal{H}}_s$ vs x/s for parameter values useful to the device designer. Curves of $\bar{\mathcal{H}}_s$ for $z_s = 0$ are unique in that each has a cusp at $x/s = 0.25$, where the slope $\partial\bar{\mathcal{H}}_s/\partial x$ is not continuous. The choice $s = 4a$ requires calculation only for $0 < \xi \leq \sigma/4$ because $\bar{\mathcal{H}}_s$ is symmetric about $\xi = \pm\sigma/4$. The origin of this symmetry may be understood by superimposing another current sheet with current density $\mathbf{J} = (J_o/2)\hat{j}$ on the existing stripe pattern of Fig. 64. This addition leaves the z component of field unaltered. It creates, however, a system of adjacent conducting stripes of width $2a$, carrying the current $I = J_o a$ alternately in the positive and negative y direction. Such an array of stripes enjoys symmetry about the points of discontinuity. Contributions to the z component of field from any pair of stripes symmetrically disposed about a selected discontinuity will add; $\bar{\mathcal{H}}_s$ will, therefore, have extrema at points of current-density discontinuity. To illustrate how the average field intensity decreases with increasing distance from the conduc-

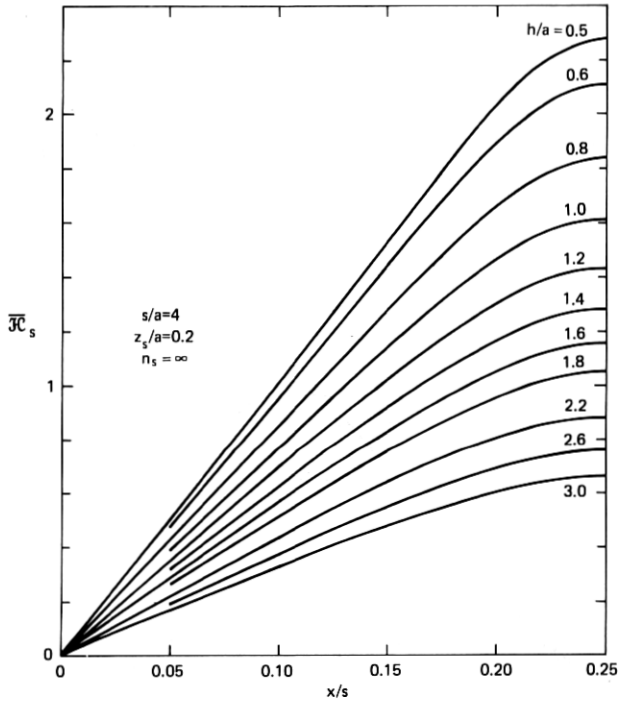

Fig. 67—Same as Fig. 65, except $z_s = 0.2a$.

tor array, values of $\bar{\mathscr{H}}_s$ were computed for several stand-off distances z_s. Since $\bar{\mathscr{H}}_s$ assumes its maximum value at $x/s = 0.25$ for $s/a = 4$, the stripe edge was chosen for the calculations. See Fig. 70.

To convert to cgs units, write $\bar{H}_z = \bar{\mathscr{H}}_s J_o$ Oe and express J_o in A/mm or mA/μm. In other words, the dimensionless quantity $\bar{\mathscr{H}}_s$ gives the average field intensity in oersteds when the linear current density J_o is 1 mA/μm.

The gradient of the average field $\partial \bar{H}_z/\partial x$ can be obtained with only a slight increase in computing effort because the needed function values are available. The dimensionless gradient is

$$\bar{\mathscr{G}} = \left(\frac{4\pi h}{J_o}\right)\frac{\partial \bar{H}_z}{\partial x} = 2\sum_{n}\sum_{j=1}^{2}(-1)^j \text{Arctan } C_{nj}. \tag{18}$$

When the number of stripes n_s is large, one may use the approximation

$$\bar{\mathscr{G}} = 2\sum_{-N}^{+N}\sum_{j=1}^{2}[(-1)^j \text{Arctan } C_{nj}] - (8\alpha/\sigma^2)\left[\zeta(2) - \sum_{1}^{N} n^{-2}\right]$$
$$- (8\alpha/\sigma^4)[3\xi^2 + \alpha^2 - \xi_2^2 - \zeta_2\zeta_1 - \xi_1^2]\left[\zeta(4) - \sum_{1}^{N} n^{-4}\right], \tag{19}$$

an expression correct to the 4th order in the quantity $1/n$. Equation

(19) adds the contribution from the $2N + 1$ stripes nearest the origin to the contribution, approximated by a truncated series in powers of $1/n$, of the infinitely many remaining stripes. Accuracy requirements determine the value of N.

10.2 Infinite conducting sheet with circular hole

Consider again an infinitely thin conducting sheet in the plane $z = 0$. Let the sheet contain a circular hole, extend to infinity, and support

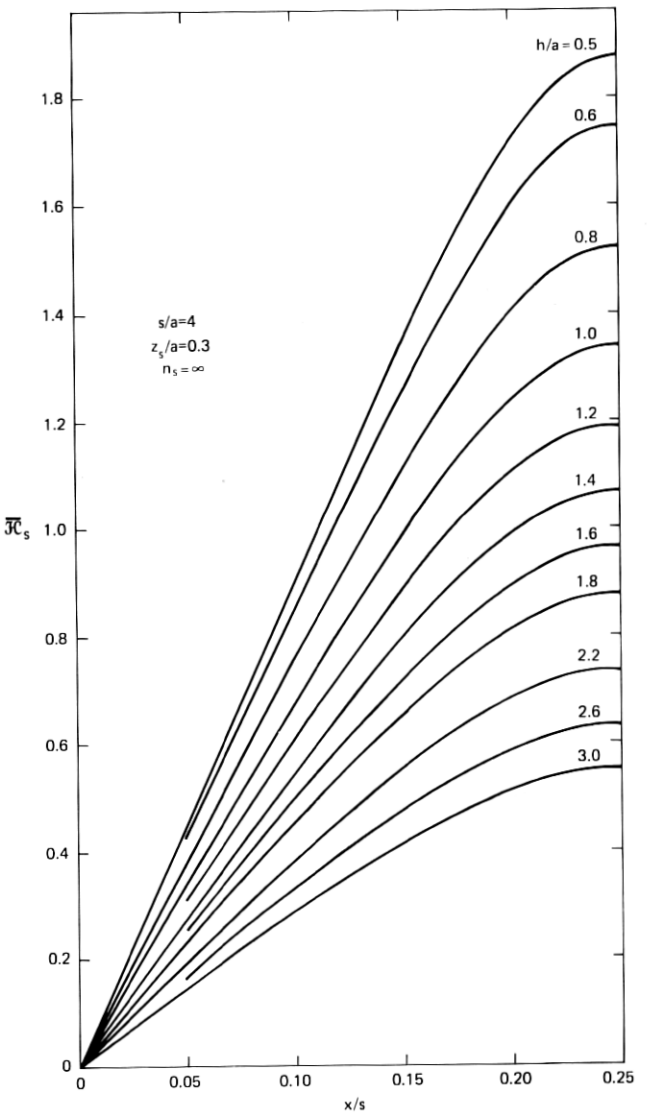

Fig. 68—Same as Fig. 65, except $z_s = 0.3a$.

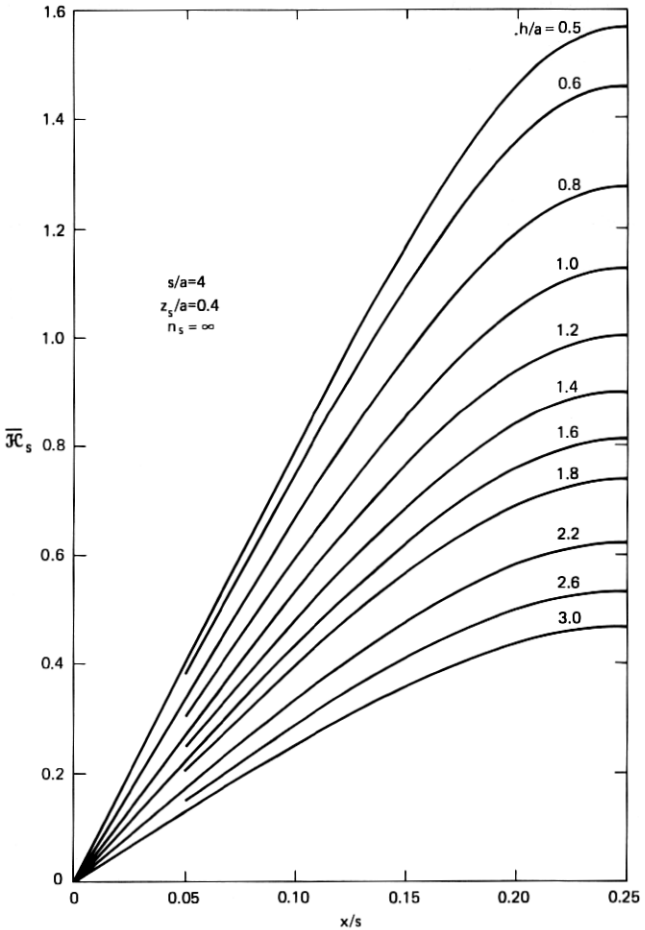

Fig. 69—Same as Fig. 65, except $z_s = 0.4a$.

the constant current density $\mathbf{J} = J_o\hat{\imath}$ at points infinitely removed from the hole. The origin of coordinates is chosen at the symmetry point of the geometry as shown in Fig. 71. The problem to be solved—a means of obtaining the z component of the magnetic field at the point $P(r, \theta)$—falls into two parts: (*i*) solution of a boundary-value problem to yield the linear current density $\mathbf{J}$ in the plane $z = 0$, and (*ii*) integration over the source distribution to obtain the field.

The first of these is discussed by Milne-Thompson[43] in connection with two-dimensional fluid flow around a cylindrical obstacle. The current density is

$$\mathbf{J} = J_o[1 - (a/\rho)^2\cos 2\phi]\hat{\imath} - J_o(a/\rho)^2\sin 2\phi\hat{\jmath}, \qquad (20)$$

where

J_o = constant linear current density at infinity,

a = hole radius,

ρ = radial source coordinate,

ϕ = angular source coordinate.

The reader may quickly verify that eq. (20) satisfies the requisite boundary conditions. The current density is tangential at $\rho = a$ and $\mathbf{J} \to J_o\hat{\imath}$ as $\rho \to \infty$. One can now obtain the magnetic field in MKS units from

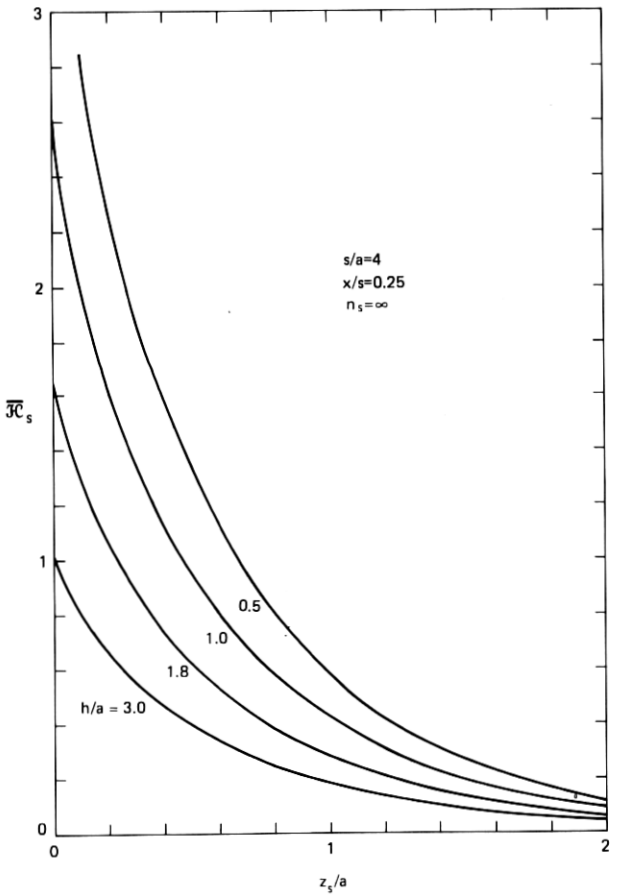

Fig. 70—Dimensionless average value $\bar{\mathcal{H}}_s$ of the z component of magnetic field as a function normalized stand-off distance z_s/a. The curves are graphs of eq. (17) for $s = 4a$ and $x = 0.25s$. The ordinate $\bar{\mathcal{H}}_s$ is numerically equal to the field in oersteds when the linear current density of each stripe is 1 mA/μm.

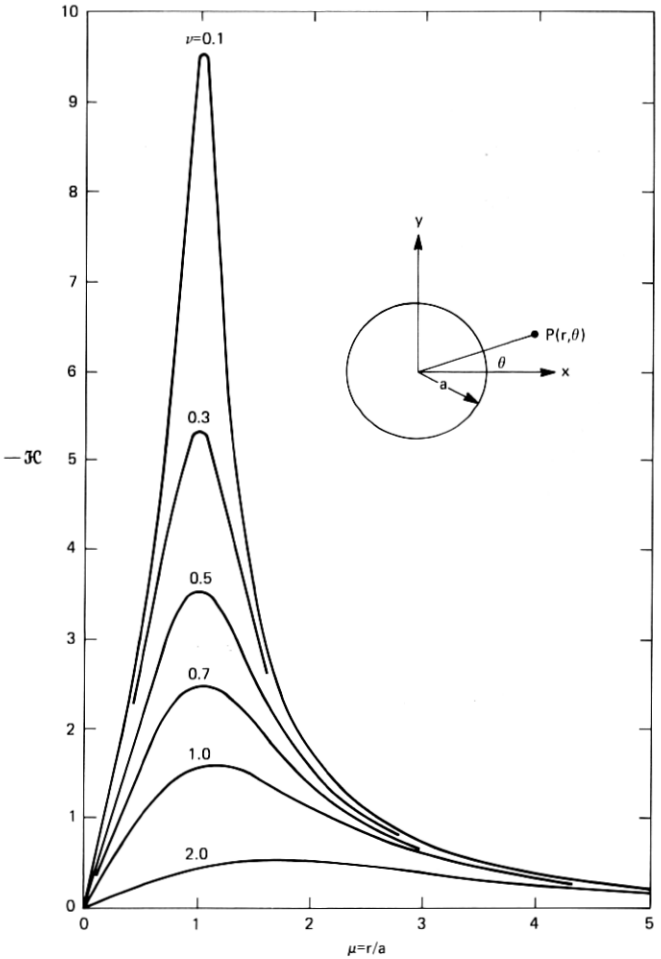

Fig. 71—Current sheet with circular hole. The dimensionless z component of the magnetic field is shown as a function of the reduced distance $\mu = r/a$ for several values of $\nu = z/a$. The curves are graphs of $\mathcal{H}$ defined by the integral below eq. (23). The ordinate $\mathcal{H}$ is numerically equal to the field in oersteds when $\theta = 90°$ and the linear current density approaches 1 mA/μm as $r \to \infty$.

$$4\pi\mathbf{H} = \int_s \frac{\mathbf{J} \times \mathbf{R}}{R^3}\, d\xi\, d\eta, \tag{21}$$

where

$$\mathbf{R} = (x - \xi)\hat{\imath} + (y - \eta)\hat{\jmath} + z\hat{k} \quad \text{and} \quad R = |\mathbf{R}|.$$

The surface integral, with respect to the source coordinates ξ and η, extends over the entire $\xi - \eta$ plane apart from the points $\rho = (\xi^2 + \eta^2)^{1/2} < a$, where the current density vanishes. After projecting

eq. (21) on the z-axis and expressing all components in cylindrical coordinates, one obtains a double integral of the form

$$4\pi H_z = J_o \int_0^{2\pi} d\phi \int_a^{\infty} \Phi(r, \theta, z, \rho, \phi)\, d\rho. \tag{22}$$

All radial integrals are tabulated; see, for example, Gradshteyn and Ryzhik.[44] The remaining angular integration, however, must be done numerically. After appropriate changes of the variables and collecting terms, eq. (22) reduces to

$$4\pi H_z = J_o \mathscr{H} \sin\theta, \tag{23}$$

where

$$\mathscr{H} = 2\int_0^{\pi} (F_1 + F_2 + F_3)\, d\psi = \mathscr{H}(\mu, \nu),$$

$$F_1 = \frac{C_0 + C_1 C + C_2 C^2 + C_3 C^3 + C_4 C^4}{\sigma^2(\sigma^2 - \mu^2 C^2)(\sigma^2 + 1 - 2\mu C)^{1/2}},$$

$$F_2 = C\ln[(\sigma^2 + 1 - 2\mu C)^{1/2} + 1 - \mu C],$$

$$F_3 = \mu(2C^2 - 1)\sigma^{-3}\ln\left[\frac{\sigma(\sigma^2 + 1 - 2\mu C)^{1/2} + \sigma^2 - \mu C}{\sigma - \mu C}\right],$$

$$\mu = r/a, \qquad \nu = z/a,$$

$$\sigma = (\mu^2 + \nu^2)^{1/2}, \qquad C = \cos\psi,$$

$$C_0 = \mu\sigma^2(1 + \sigma^2),$$

$$C_1 = (\sigma^2 + \mu^2)(1 - \sigma^2),$$

$$C_2 = -\mu[\sigma^2(\sigma^2 + 3) + 2\mu^2],$$

$$C_3 = 2\mu^2(\sigma^2 - 1),$$

$$C_4 = 4\mu^3.$$

Numerical integration over the angular variable of eq. (22) employed the automatic numerical quadrature routine QUAD.[45] The dependence of $\mathscr{H}$ on the radius and altitude is shown in Fig. 71. Using this figure and eq. (23), one may now estimate H_z in MKS units. In the hybrid units described earlier, the z component of magnetic field in oersteds is numerically equal to $\mathscr{H}$ when $J_o = 1$ mA/μm and $\theta = \pi/2$.

To obtain information about the average value,

$$\bar{H}_z = \frac{1}{h}\int_{z_s}^{z_s+h} H_z\, dz = \frac{J_o \sin\theta}{4\pi h}\int_{z_s}^{z_s+h} \mathscr{H}(\mu, \nu)\, dz, \tag{24}$$

the dimensionless quantity

$$\bar{\mathscr{H}} = \bar{\mathscr{H}}(\mu, \gamma) = h^{-1} \int_{z_s}^{z_s+h} \mathscr{H}\, dz = \gamma^{-1} \int_{\nu_s}^{\nu_s+\gamma} \mathscr{H}(\mu, \nu)\, d\nu \qquad (25)$$

was computed. Here $\nu_s = z_s/a$ and $\gamma = h/a$. Since several γ values are of interest, one may take advantage of the linear property of integration to reduce the number of function evaluations. Index the γ values of interest with j such that $\gamma_{j+1} > \gamma_j$. To obtain a uniform formula and accommodate Fortran requirements, one must choose $\gamma_1 = 0$ and the smallest value of interest γ_2. Then, with the notation $\bar{\mathscr{H}}_j = \bar{\mathscr{H}}(\mu, \gamma_{j+1})$, one finds

$$\bar{\mathscr{H}}_j = \frac{1}{\gamma_{j+1}} \sum_{i=1}^{j} g_i, \qquad (26)$$

where

$$g_i = \int_{\nu_s+\gamma_i}^{\nu_s+\gamma_{i+1}} \mathscr{H}(\mu, \nu)\, d\nu.$$

Each g_i was evaluated with a 3-point Gaussian rule; for the γ_j used in the computation the estimated error is of order 10^{-4}. The radial slope $\bar{\mathscr{S}} = \partial\bar{\mathscr{H}}/\partial\mu$ was also computed using the approximation

$$\bar{\mathscr{S}}(\mu_k, \gamma_j) \approx [\bar{\mathscr{H}}(\mu_{k+1}, \gamma_j) - \bar{\mathscr{H}}(\mu_{k-1}, \gamma_j)]/2\Delta u, \qquad (27)$$

where Δu is the constant difference between adjacent values of μ. The dependence of $-\bar{\mathscr{H}}$ and $-\bar{\mathscr{S}}$ on r/a is shown in Figs. 72 and 73, respectively. Contour maps of constant $\bar{H}_z$ demonstrate the overall behavior of the field. Figure 7 shows contours of $\bar{H}_z$ = constant for the reduced stand-off distances $z_s/a = 0.06$ and 0.3. For both, $h/a = 0.8$.

10.3 Linear chain of oval holes

Current experimental devices use quasi-elliptic openings rather than circular holes; see, for example, Fig. 29. The work of Richmond[46] with electric fields about a linear grating permits more realistic magnetic field calculations. Consider an infinite chain of identical oval holes on the y-axis, spaced 2b units apart, each with semiaxes $a_2 > a_1$ parallel to the y and x axes, respectively. See Fig. 74 for the oval at the origin. Because of symmetry and the periodicity 2b in the y direction, Laplace's equation need be solved only in the region of Fig. 74. Richmond[46] gives the conformal transformation

$$z = (a_1/c)w + (a_2/\gamma)\cosh^{-1}(\cos\gamma \cosh w) \qquad (28)$$

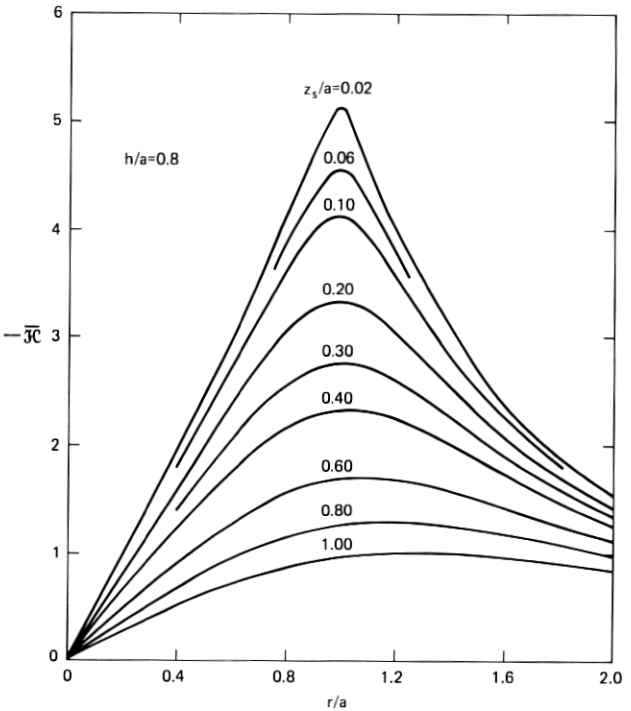

Fig. 72—Dimensionless average value $\bar{\mathcal{H}}$ of z component of magnetic field as a function of r/a for an infinite current sheet with a circular hole. The curves are graphs of eq. (25) for $h = 0.8a$, where a is the hole radius. The ordinate $\bar{\mathcal{H}}$ is numerically equal to the field in oersteds when $\theta = 90°$ and the linear current density approaches 1 mA/μm as $r \to \infty$.

from which one finds the complex linear current density

$$J = \frac{2bJ_o}{\pi}\left[\frac{dw}{dz}\right]^* = \left[\frac{\alpha_2 \gamma c J_o(\cos^2\gamma \cosh^2 w - 1)^{1/2}}{\alpha_1\gamma(\cos^2\gamma \cosh^2 w - 1)^{1/2} + c \cos\gamma \sinh w}\right]^* \tag{29}$$

outside the oval. Here J_o, a real constant, is the linear current density as $x = \to \infty$, $\alpha_1 = a_1/a_2$, $\alpha_2 = 2b/\pi a_2$, $z = x + iy$, $w = u + iv$, and * means complex conjugate. Inside the oval, $J = 0$. The real parameters c and γ satisfy the nonlinear equations $\cos\gamma \cosh c = 1$ and $c(\gamma\alpha_2 - 1) = \alpha_1\gamma$. Elimination of c from the equations leads to an efficient algorithm, based on Newton's method, for machine computation of γ for practical values of $\alpha_1 \leqslant 1$ and α_2. The iteration scheme

$$\gamma_{i+1} = \gamma_i - \frac{f_i}{f_i'} = \gamma_i + \frac{\gamma_i g_i[\alpha_1\gamma_i + g_i(1 - \alpha_2\gamma_i)]\cos\gamma_i}{\alpha_1\gamma_i^2 + g_i^2\cos\gamma_i}, \tag{30}$$

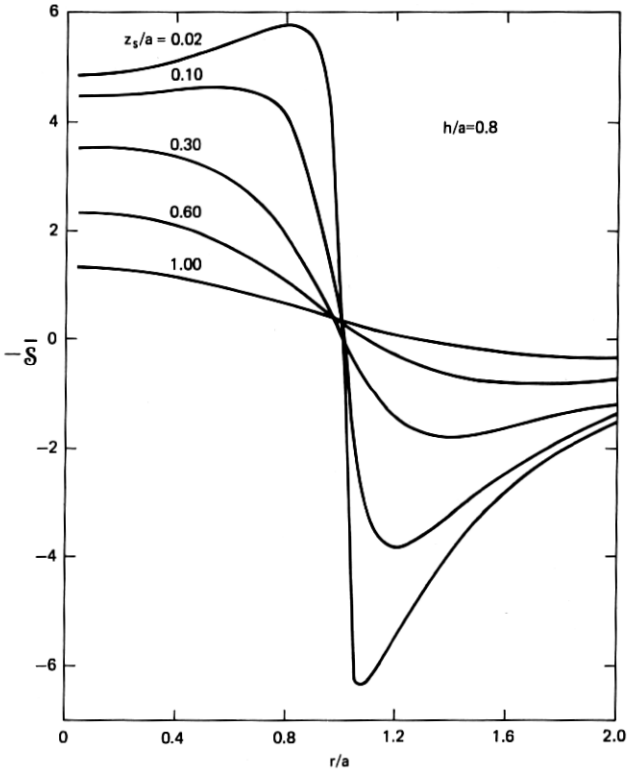

Fig. 73—Dimensionless slope $\mathcal{S} = \partial\mathcal{H}/\partial\mu$ of the z component of magnetic field as a function of r/a for an infinite current sheet with a circular hole. The curves are graphs of eq. (27) for $h = 0.8a$, where a is the hole radius.

where

$$f = \alpha_1 g^{-1} + \gamma^{-1} - \alpha_2,$$

$$g = \ln[(1 + \sin\gamma)/\cos\gamma],$$

$$f' = df/d\gamma,$$

$$f_i = f(\gamma_i),$$

$$f_i' = df/d\gamma \text{ evaluated at } \gamma = \gamma_i,$$

may be started with $\gamma_o = 1/\alpha_2$. If the iteration process ends with γ_j, the parameter c follows from $c = g_j = \ln[(1 + \sin\gamma_j)/\cos\gamma_j]$.

By setting u or v constant in eq. (28), one obtains equipotential or flow lines, respectively. Several flow lines, indexed with the angle variable $\Psi = 180v/\pi$, are shown in Fig. 74. The oval satisfies the parametric equations

$$x/a_2 = (\alpha_1/c)\cosh^{-1}(q/\cos\gamma) \qquad (31a)$$

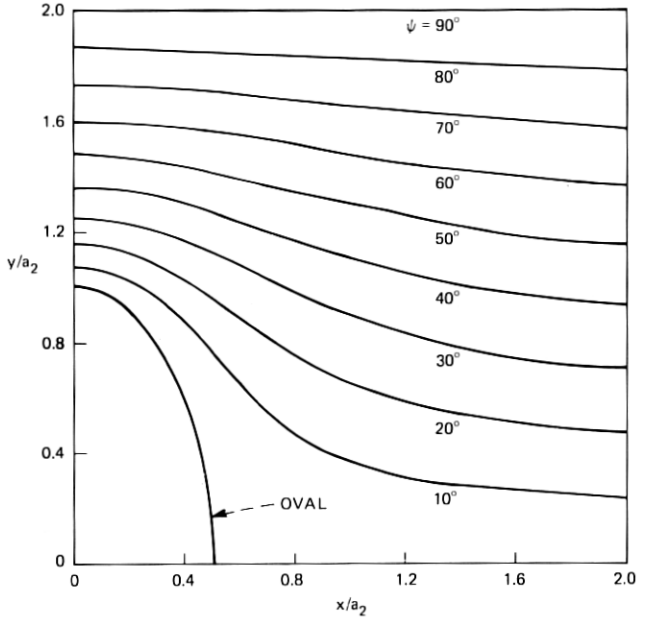

Fig. 74—Current flow near an infinite chain of oval holes. Identical oval holes with semiaxes $a_2 = 2a_1$ and spacing $2b = 4a_2$ occupy the y-axis. The flow lines, indexed with $\psi = 180\upsilon/\pi$, were obtained from eq. (28) with υ = constant. Note the almost elliptical shape of the oval for the parameter ratios $a_1/a_2 = 0.5$ and $b/a_2 = 2$ used here.

and

$$y/a_2 = (1/\gamma)\cos^{-1}q, \tag{31b}$$

where $0 \leq \cos\gamma \leq q \leq 1$. Richmond[46] discusses the departure from ellipticity. For geometries of practical interest, say, $a_1/a_2 \approx 0.5$ and $b/a_2 \approx 2$, the oval may be regarded as an ellipse. The distribution of current along the line of minimum separation between ovals satisfies eq. (29) with $u = 0$. It was computed from

$$\frac{J}{J_o} = \frac{\alpha_2\gamma c(1 - \cos^2\gamma\cos^2\upsilon)^{1/2}}{\alpha_1\gamma(1 - \cos^2\gamma\cos^2\upsilon)^{1/2} + c\cos\gamma\sin\upsilon}, \qquad 0 \leq \upsilon \leq \pi/2 \tag{32}$$

and is shown in Fig. 75. The coordinate value associated with υ follows from eq. (28).

To complete the field computations, an efficient method for the numerical double integration of the components of eq. (21) must be constructed. This work is in progress.

10.4 Bubble motion

Experimental evidence, Fig. 34, for example, strongly suggests bubbles with different hardness parameters. A study of bubble motion will

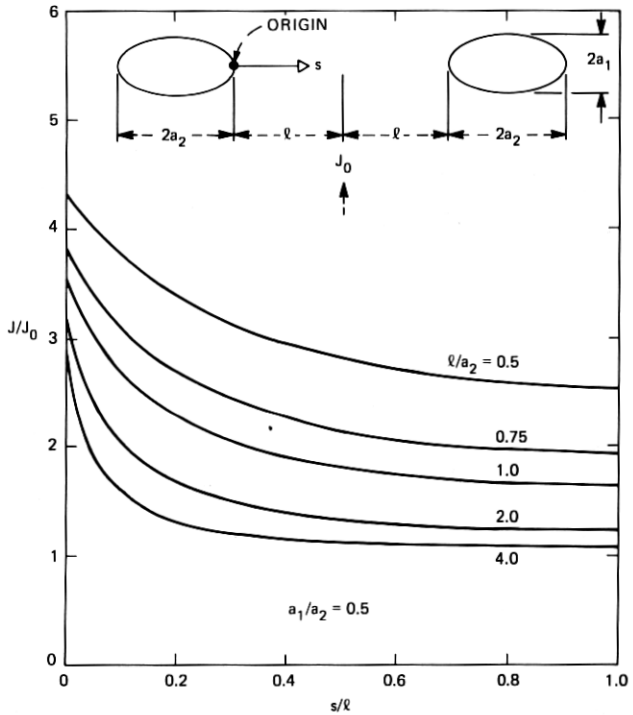

Fig. 75—Distribution of linear current density along the line of minimum separation between ovals of an infinite chain. The current density is normalized to J_0, its value infinitely far from the ovals. The graphs were obtained from eq. (32).

aid the device designer by prediction of trajectories and transit times.

With the assumption that the bubble speed,[47]

$$V = \mu_b[d_b|\nabla \bar{H}_z| - 8H_c/\pi] \geqslant 0, \tag{33}$$

is independent of the hardness or S number, the equations of motion in rectangular coordinates are

$$\dot{x}_i = -VT_{ij}e_j, \tag{34}$$

where V is a scalar point function, μ_b is the bubble mobility equal to one-half the wall mobility, d_b is the bubble diameter, $\bar{H}_z$ is the z component of field averaged over the bubble height, H_c is the coercivity field, $T_{11} = T_{22} = \cos\phi$, $T_{12} = -T_{21} = \sin\phi$, $\hat{e} = \nabla\bar{H}_z/|\nabla\bar{H}_z|$, e_j is the projection of $\hat{e}$ on the jth coordinate axis, and ϕ is the angle between $-\hat{e}$ and the local velocity $\mathbf{V}$. The angle ϕ depends on S according to $\sin\phi = 8SV/\gamma d_b^2|\nabla\bar{H}_z|$ and is regarded as a fixed parameter in eq. (34). Here γ is the gyromagnetic ratio of the material.[48] See also Fig. 76. When applied to bubble motion due to fields from a hole of radius a in a current sheet, eqs. (33) and (34) assume the form

$$\dot{\xi}_1 = -(F_c/\mu^3)[\xi_1\xi_2(\mu\bar{\mathscr{P}} - \bar{\mathscr{H}})\cos\phi + (\mu\xi_2^2\bar{\mathscr{P}} + \xi_1^2\bar{\mathscr{H}})\sin\phi], \quad (35a)$$

$$\dot{\xi}_2 = +(F_c/\mu^3)[\xi_1\xi_2(\mu\bar{\mathscr{P}} - \bar{\mathscr{H}})\sin\phi - (\mu\xi_2^2\bar{\mathscr{P}} + \xi_1^2\bar{\mathscr{H}})\cos\phi], \quad (35b)$$

where

$$F_c = 1 - 8H_c/\pi d_b\,|\nabla\bar{H}_z|,$$

$$|\nabla\bar{H}_z| = (J_o/a)[\bar{\mathscr{P}}^2\sin^2\theta + (\bar{\mathscr{H}}/\mu)^2\cos^2\theta]^{1/2},$$

$$\sin\theta = \xi_2/\mu,$$

$$\cos\theta = \xi_1/\mu,$$

$$\mu = (\xi_1^2 + \xi_2^2)^{1/2},$$

$$\xi_1 = x/a,$$

$$\xi_2 = y/a,$$

$$\bar{\mathscr{P}} = \partial\bar{\mathscr{H}}/\partial\mu.$$

Hybrid units were used for eq. (35); this allows substitution for H_c in oersteds. The current density J_o, however, must be in units of mA/μm. The dot over the variables on the left-hand side of eq. (35) means differentiation with respect to the normalized time $T = t/\tau$, where $\tau = a^2/\mu_b\, d_b\, J_o$. Solutions to these coupled, nonlinear differential equations must, in general, be obtained by numerical techniques. Some special cases, amenable to an analytical approach, are now described.

The equations of motion, eq. (34), assume a simple form when written in polar coordinates:

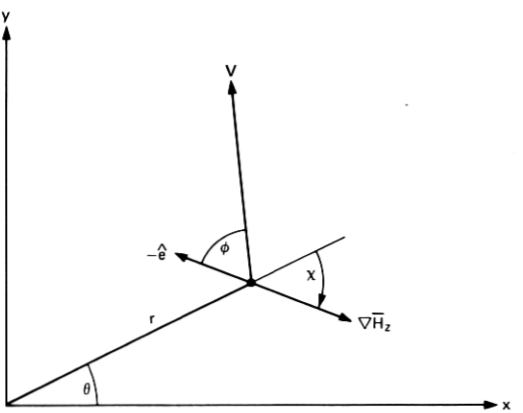

Fig. 76—Coordinate system and symbols used in the equations of bubble motion. Note that the angle χ, as shown here, is a negative quantity because the projection of $\nabla\bar{H}_z$ on the unit vector $\hat{\theta}$ of the polar coordinates (r, θ) is negative.

$$\dot{r} = dr/dt = -V\cos(\phi - \chi), \tag{36a}$$

$$\dot{\theta} = d\theta/dt = +(V/r)\sin(\phi - \chi), \tag{36b}$$

where χ is the angle between $\nabla \bar{H}_z$ and $\hat{r}$ a unit vector in the radial direction. Division of eq. (36b) by (36a) yields the velocity ratio

$$r\dot{\theta}/\dot{r} = v_\theta/v_r = \tan(\chi - \phi). \tag{37}$$

Consider now the special case $\chi = 0$. This implies $\partial \bar{H}_z/\partial\theta$ vanishes. Since ϕ is a constant, eq. (37) may be integrated to furnish the trajectory

$$\theta = \theta_o + \tan\phi \ln(r_o/r), \tag{38}$$

where r_o and θ_o specify the position at some reference time, $t = t_o$. The path is a logarithmic spiral; it is unique in that it is independent of the radial behavior of $\bar{H}_z$. The dependence of $\bar{H}_z$ on r will, however, determine the position and velocity along the spiral as a function of the time by inversion of the quadrature

$$t = t_o + \sec\phi \int_r^{r_o} \frac{ds}{V(s)}. \tag{39}$$

Equation (39) follows from eq. (36a). When the functional dependence of $\bar{H}_z$ on r is sufficiently simple, eq. (39) may be integrated and inverted. For example, when $\bar{H}_z = H_o(r/d_b)^2$, $V = v(r) = (r - \alpha\, d_b)/\tau_o$. Here H_o is a constant, $\alpha = 4H_c/\pi H_o$, $\tau_o = d_b/\mu_w H_o$, and $\mu_w = 2\mu_b$ is the wall mobility. Integration of eq. (39) furnishes

$$r = \alpha d_b + (r_o - \alpha d_b)\exp(-\lambda t), \tag{40}$$

where $\lambda = \tau_o^{-1}\cos\phi$ and $t_o = 0$. Figure 77 shows several trajectories. Bubble motion starts at a point $r = r_o$ marked $t/\tau_o = 0$. From there, bubbles travel along logarithmic spiral paths terminating at the origin. The numerals along the various paths give bubble position in units of t/τ_o for $\alpha d_b/r_o = 0.5$. When $H_c = 0$ and $0 \leqq \phi < 90°$, all bubbles spiral into the origin arriving there as $t \to \infty$.

Two special cases of bubble motion near a circular opening allow integration of eq. (35) by quadrature. For both, $S = \phi = 0$. Consider a bubble located on the y axis at $t = 0$. Using polar coordinates, one finds immediately $\theta =$ constant since $\phi = 0$ and $\chi = 0$ or π; see eq. (36). The radial equation is solved by the quadrature

$$t = \tau \int_0^{r/a} \frac{d\sigma}{|\bar{\mathcal{P}}(\sigma)| - \beta} \tag{41}$$

for motion starting at the origin. Here, $\tau = a^2/\mu_b d_b J_o$ and $\beta = 8H_c a/\pi d_b J_o$ with H_c in oersteds and J_o in mA/μm. Numerical evalua-

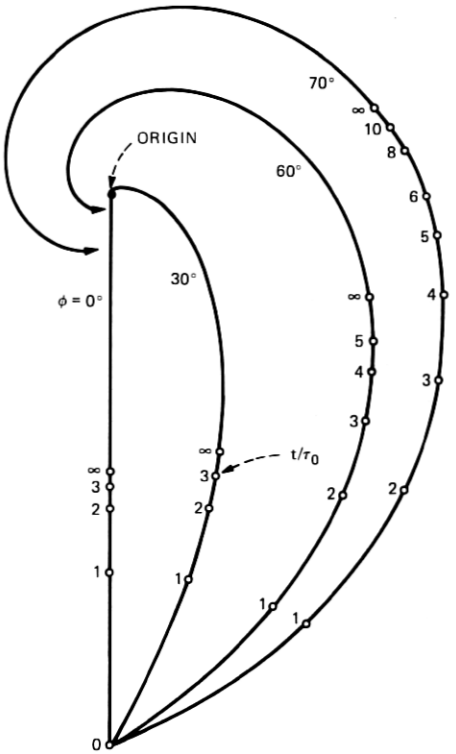

Fig. 77—Logarithmic spiral trajectories described by eq. (38). Bubbles spiral into the origin along these paths when $H_c = 0$. For $H_c > 0$, motion is along the same paths but bubbles do not reach the origin. The timing markers, in units of t/τ_o, show positions for $\alpha d_b/r_o = 0.5$.

tion of eq. (41) for $a = d_b = 2\mu$m, $H_c = 1$ Oe, $\mu_b = 1$ μm/μs-Oe, $J_o = 1$ mA/μm, $z_s/a = 0.06$, and $h/a = 0.8$ shows that 0.70 μs are required for motion from $r = 0$ to $r = 0.8a$. For these parameters, the characteristic time τ equals 2 μs. Arrival at $r/a = 0.8$ completes approximately 90 percent of the possible radial motion.

The second special case occurs when a bubble resides at the radial minimum of $\bar{\mathcal{H}}$ at $t = 0$. Enter eq. (36) with $\phi = 0$ and $\chi = -\pi/2$. Thus, $r = r_e$ = constant, and the equilibrium value r_e is found from the solution of $\bar{\mathcal{P}}(\mu) = \partial\bar{\mathcal{H}}/\partial\mu = 0$ with $\mu_e = r_e/a$. As may be seen from Fig. 72, $r_e/a \approx 1$ for small z_s/a. Equation (36b),

$$\dot{\theta} = V/r_e = \tau_1(\cos\theta - \beta_1), \tag{42}$$

where $\tau_1 = a^2\mu_e^2/\mu_b d_b J_o\,|\,\bar{\mathcal{H}}_e\,|$, $\beta_1 = 8H_c a\mu_e/\pi d_b J_o\,|\,\bar{\mathcal{H}}_e\,|$, and $\bar{\mathcal{H}}_e = \bar{\mathcal{H}}(\mu_e)$ is the value of $\bar{\mathcal{H}}$ at the equilibrium radius, has the solution

$$t = \tau_1 \csc\theta_m \ln\left[\frac{\tan(\theta_m/2) + \tan(\theta/2)}{\tan(\theta_m/2) - \tan(\theta/2)}\right] \tag{43}$$

for a bubble at $\theta = 0$ when $t = 0$. The angle θ_m is attained as $t \to \infty$ and satisfies the condition $\cos \theta_m = \beta_1$. For the numerical values used in the previous example together with $\mu_e = 1.00$ and $|\bar{\mathcal{H}}_e| = 4.56$, one finds $\theta_m = 56.0°$ and the time needed for travel from $\theta = 0$ to $\theta = 0.9\theta_m$ is 1.48 μs.

10.5 Discussion

The graphs of Figs. 65 to 69 apply to an infinite number of conducting stripes. As shown in these figures, $\bar{\mathcal{H}}_s = 0$ at the origin, a conductor center, and rises to a maximum at the right conductor edge. The symmetry of $\bar{\mathcal{H}}_s$ about a conductor edge for $s = 4a$ together with the periodicity and antisymmetry expressed by eq. (16) completes the description of $\bar{\mathcal{H}}_s$ for one period. See Fig. 8 for a typical spatial variation of $\bar{\mathcal{H}}_s$ over several periods.

When the number of conducting stripes is finite, $\bar{\mathcal{H}}_s$ still has the wavelike behavior per period as described above. There are, however, essential differences. The function $\bar{\mathcal{H}}_s$ is not periodic. In addition, the wavelike behavior of $\bar{\mathcal{H}}_s$ is superimposed on a gradual change in the mean value of the bias field. This change in bias is due to the current $I = 2an_sJ_o$ flowing in the n_s stripes. The magnitude of the effect can be estimated, using eq. (15), for a single stripe of width $(n_s - 1)s + 2a$. To illustrate the quality of the estimate, consider $n_s = 11$ and $s = 4a$. Choose the origin at the middle of the center stripe and calculate $\bar{\mathcal{H}}_s$ at the center of each stripe and at the corresponding abscissa for a single stripe of width $(n_s - 1)s + 2a = 42a$. Then, for $\alpha = 1$, the numerical results are shown in Table VI. Here, $\bar{\mathcal{H}}_1$ is the normalized intensity for the single stripe. In the design of current-access devices, the shift in local bias must be taken into account. By returning the drive current through a nearby stripe of comparable width, this shift in local bias can be reduced.

To develop current-access propagation structures, large-scale models were made and the magnetic fields due to current flow in them probed with a coil. See Section III. One structure was a stripe pattern which served to calibrate the coil in the following way. The coil of radius r_o and height h was placed over a central stripe with the coil center

Table VI

Stripe Index n	Abscissa x/h	$\lvert\bar{\mathcal{H}}_s\rvert$	$\lvert\bar{\mathcal{H}}_1\rvert$
0	0	0	0
±1	±4.0	0.367	0.385
±2	±8.0	0.760	0.802
±3	±12.0	1.218	1.293
±4	±16.0	1.829	1.995
±5	±20.0	2.928	3.582

directly over the stripe edge. This location permitted maximum flux linkage. One can now calculate the flux threading the coil from

$$\phi = \int B\, dA = 4J_o \int_0^{r_o} \mathscr{H}_s(u)\, du \int_0^{(r_o^2-u^2)^{1/2}} dv, \tag{44}$$

where the u-v coordinate system has its origin at the coil center with u parallel to x and v parallel to y. The integration proceeds over the first quadrant of the coil cross section; hence, the multiplier of 4. Finally, eq. (44) will give the flux in maxwells when the current density is expressed in A/mm and the coil radius in cm. Numerical integration over u utilized the parameter values $r_o = 0.1$ in., $h = 0.2$ in., and $z_s = 0.025$ in. Using the stripe width $2a = 0.5$ in., one gains entry to Fig. 66 with $h/a = 0.8$ and $z_s/a = 0.1$ to determine the values of $\mathscr{H}_s(u)$. Numerical quadrature yields $\phi = (6.183J_o/\pi)\pi r_o^2$. The result is written in this form because division by πr_o^2 provides the flux density averaged throughout the coil volume. For a sinusoidal drive $J_o = J_m \sin \omega t$, the rms voltage induced in the coil is

$$E_{\text{rms}} = 6.183 N_t \omega r_o^2 J_m \times 10^{-8}/\sqrt{2} = 2.1 \text{ mV} \tag{45}$$

for $N_t = 100$ turns, $\omega/2\pi = 30$ kHz, and $J_m = 1/25.4$ A/mm. This result compares favorably with the measured value of 2.0 mV. With the coil calibration in hand, one can assign absolute field values to voltage measurements from the large-scale models of proposed propagation structures. Apart from a slight increase in labor associated with a two-dimensional numerical integration over the coil cross section, one can also use eq. (25) for coil calibration. This has been done, and the results show a comparably small difference between the measured and calculated coil voltage.

XI. MISCELLANEOUS

This section contains items that do not seem to fit elsewhere. These include a three-level conductor circuit, a single level circuit with a lattice of etched islands, a deep implant layer for hard bubble suppression, and an analysis of bubble-bubble interactions.

11.1 Three-level conductor circuits

Advances in processing techniques will ultimately allow fabrication, at high yield, of structures with a complexity unattainable today. One structure that could become practical is the three-level circuit we discuss at this time.

Bias shift due to current flow in a conductor and its consequences was covered in Section III and, in particular, in Fig. 9. By using three-conductor levels and returning the current of the excited level through

the remaining two, one can ease the bias-shift problem and utilize for storage the full conductor width. Another advantage is simpler electronics; only unipolar drivers are needed.

Two possible propagation structures are shown in Fig. 78. Circuit (a) has slots side by side in each of the three levels. The number of + and − signs indicates the relative pole strengths at the ends of the slots when level 1 is energized with two units of current, half of which returns through each of the remaining levels. The wavelike curve sketched below is an approximation to H_z near the lower ends of the slots. If the levels are excited in turn with pulse currents I_j in the sequence [···123···], the wave will move to the right and bubble propagation will be to the right. Interchange any two drives in the sequence, such as [···213···], and bubbles move left. Circuit (b) with in-line oval holes in the three levels generates the indicated relative pole strengths when level 1 is excited. Here also, the sequence

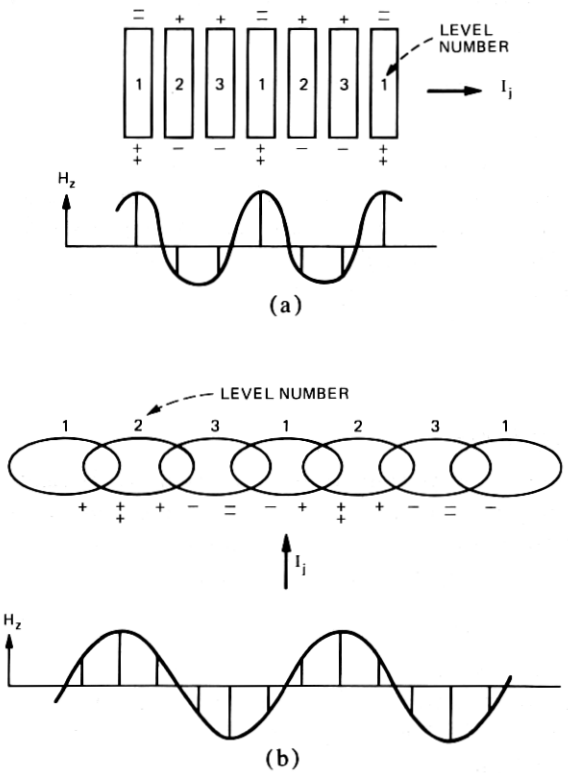

Fig. 78—Two types of three-level circuits are shown: in-line (a) and transverse (b) propagation. In either case, the drive current is returned through the remaining levels to provide z-field cancellation.

[...123...] will cause bubble motion to the right, and the reversal of any two drives in the sequence, to the left.

11.2 Single-level lattice-like circuits

In most single-level conductor circuits, a rather precise fit of the bubble with the feature which produces the static offset field is required. In other words, these circuits cannot tolerate a change in bubble size. A lone exception is that of Dekker in which permalloy points driven by an in-plane field generate the offset field. Other alternatives are possible. From the magnetostatic equivalence of bubbles and cylindrical holes etched in a garnet layer (craters), one can deduce that, at a distance, craters repel bubbles. Therefore, an array of craters can provide interstitial sites that precisely position bubbles. Bubble motion would then be somewhat analogous to electrons jumping from trap to trap in a semiconductor. Devices based on this principle are under study.

11.3 Deep implantation for hard bubble suppression

Data on the performance of implanted and nonimplanted films in dual-conductor devices were presented in Figs. 32 to 35. In particular, Figs. 32 and 34 point out that the minimum drive currents are higher when implanted films are used. This we attribute to a reduction in the effective drive fields because of the shielding effect of implanted layers. If the garnet is implanted at the garnet-substrate interface, this shielding will be eliminated. Experiments with a 2.25-μm thick YSmLuCaGe garnet implanted at 2×10^{16} with H^+ at 300 Kev confirmed this expectation. We anticipate that deep implantation will be especially useful if the garnet layers are less than a micron thick since the buried layer will precisely determine bubble height and, in addition, decouple bubbles from the sometimes troublesome substrate-garnet interface.

It is known that an in-plane field can be used to convert bubbles into the $S = 0$ state; however, the field must be very large if used with small bubble garnets. An analysis by Okabe[49] suggests that the magnitude of this field will be reduced with a very thick implant layer. A thick implant layer is practical only if it is buried.

11.4 Bubble-bubble interactions

We have already stressed the point that some conductor-access circuits can accommodate a wide range of bubble sizes. There is no "gap," in the sense of the permalloy circuits, to be overcome. In an 8-μm period, dual-conductor circuit, for example, bubbles ranging from 4 μm to less than 0.8 μm have been propagated. This tolerance to bubble size is especially useful when bubble-bubble interactions are a concern.

Bubble-bubble interaction imposes the following constraints on the circumstances under which a pair of adjacent bubbles in a track are stable in position when not driven and move in step when driven. In the absence of any drive excitation, the condition

$$H_c \geq 6\pi^2 M_s h r_o^3/\lambda^4, \tag{46}$$

where r_o is the bubble radius assures positional stability. That is, the mutual-interaction field gradients are just balanced by the coercivity H_c. During propagation, the trailing bubble must be driven to overcome both its coercivity and an interaction gradient from the leading bubble. The addition of this interaction is equivalent to a doubling of H_c. The drive current must therefore generate a gradient $\partial H_z/\partial x$ given by

$$2r_o \partial H_z/\partial x \geq 16 H_c/\pi. \tag{47}$$

It follows that, since $J \sim \partial H_z/\partial x$, $P/\text{bit} \sim (H_c r_o)^2$. From (46), it is seen that $r_o \sim H_c^{1/3}$ so

$$P/\text{bit} \sim H_c^{4/3}. \tag{48}$$

Equation (48) tells us that low-coercivity garnets are preferable to high-coercivity garnets since, with their use, the power dissipation will be reduced in spite of the interaction constraint (46).

XII. SUMMARY AND CONCLUSIONS

The purpose of this paper was to introduce new, very high speed, conductor-access devices where apertured conducting sheets replace the serpentine conductors of conventional conductor devices and the rotating-field coils of field-access devices. When apertured sheets are used, the bias field perturbations are highly localized, and therefore the drives can be ranged over wide limits. We have also shown that the impedance of the conducting layers can be made to match that of drivers operated from low-voltage (~5V) power supplies. The design of single, dual, and triple level conductor circuits was discussed.

All the functions for a shift register or a major-minor chip were covered, although some of the designs have not been optimized. For example, we have not as yet detected at a megahertz stepping rate. However, RF detection does look promising, and the redesign of both the detection electronics and the detector is in progress, and the results will be reported later.

The material requirements for the current-access device technology have been discussed. The high-speed performance inherent in this technology places more emphasis on the material parameters of bubble mobility and dynamic coercivity. Using the $(YLuSmCa)_3(FeGe)_5O_{12}$ system as a starting point, a technique has been presented to exercise

the bubble mobility while maintaining adequate uniaxial anisotropy. Compositions in the three systems, $(YLuSmCa)_3(FeGe)_5O_{12}$, $(LaLuSuCa)_3(FeGe)_5O_{12}$, and $(LaLuSm)_3(FeGa)_5O_{12}$, have been compared and the limitations found in the systems discussed. A simplified film composition in the $(LaLuSm)_3(FeGa)_5O_{12}$ systems is observed that exhibits 1.7-μm diameter bubbles along with high mobility and low dynamic coercivity.

Plasma etching has been used to define circuit features in the AlCu films. The anisotropic etch characteristics of the plasma etch process have produced metal patterns dimensionally identical to the photolithographically defined etch masks. Coupled to the high material-etch rate selectivity, the plasma etch process appears to be ideal for producing the very small period devices that current-access technology promises. Circuits have also been successfully fabricated using Au conductors patterned by ion milling technology; for Al conductors, however, the plasma etching has been the more practical etch method. Thin, conformal, insulating layers of SiO_2 have been successfully deposited by plasma deposition at low substrate temperatures, and it appears that this process is particularly suited for fabricating conductor-access devices.

Current-access and field-access devices differ, of course, in many ways. In terms of analytical complexity, the nonlinear permalloy-bubble interactions of the field-access scheme have been removed in current-access devices because permalloy is not used. One may anticipate, therefore, simpler, more frequent, and more accurate analyses in this new technology.

It is too early to conclude that conductor-access devices will become the technology of the next generation bubble devices. In this context, we include all the conductor-access devices now under development here and elsewhere. It is possible, for example, that the apertured sheet drive approach applied to the bubble-lattice file[7] will make that structure more attractive. There are some features that only conductor-access devices possess. If high speed is a necessity, as in video-based systems, conductor circuits are the only option available to the device designer at present. The anticipated small package size will be significant in applications for which space is a premium. The ability to run with logic-level power supplies is another plus for conductor devices. Finally, conductor circuits will require fewer precision analog control circuits since the critical control function to rotating field timing has been eliminated.

XIII. ACKNOWLEDGMENTS

Many people have contributed to this project. The authors thank W. Biolsi, W. L. Swartzwelder, and L. C. Luther for the growth of

garnet films, R. Wolfe for many informative discussions on ion implantation, G. P. Vella-Coleiro, R. D. Pierce, and W. Venard for material characterization, W. E. Hess for test electronics, J. A. Morrison for mathematical advice, and J. L. Blue for fruitful discussions about numerical analysis and programming.

We would also like to acknowledge the efforts of D. L. Fraser, Jr. and D. N. Wang who plasma-etched many of our early circuits, W. A. Johnson for fabricating Au conductor circuits by ion milling, R. O. Miller for constructing our plasma etch station, and R. S. Wagner for foresight and advice in developing the plasma etch process, and J. L. Smith and J. E. Geusic for words of encouragement during moments of frustration. Finally, special thanks should be given to R. T. Anderson for device-coding and to our patient typist, A. L. Becker.

XIV. MEMORIAL

This paper is dedicated to the memory of Edward M. Walters, a close friend and pioneer in magnetic bubbles.

REFERENCES

1. A. H. Bobeck, "Properties and Device Applications of Magnetic Domains in Orthoferrites," B.S.T.J., *46*, No. 8 (October 1967), pp. 1901–1925.
2. A. J. Perneski, "Propagation of Cylindrical Magnetic Domains in Orthoferrites," IEEE Trans. on Magnetics, *MAG-5*, No. 3 (September 1969), pp. 554–557.
3. R. Wolfe, J. C. North, W. A. Johnson, R. R. Spiwak, L. J. Varnerin, and R. F. Fisher, "Ion Implanted Patterns for Magnetic Bubble Propagation," AIP Conf. Proc., No. 10 (1972), pp. 339–343.
4. A. H. Bobeck and I. Danylchuk, "Characterization and Test Results for a 272K Bubble Memory Package," IEEE Trans. on Magnetics, *MAG-13*, No. 5 (September 1977), pp. 1370–1372.
5. J. A. Copeland, J. G. Josenhans, and R. R. Spiwak, "Circuit and Module Design for Conductor-Groove Bubble Memories," IEEE Trans. on Magnetics, *MAG-9*, No. 3 (September 1973), pp. 489–492.
6. T. J. Walsh and S. H. Charap, "Novel Bubble Drive," AIP Conf. Proc. No. 24 (1974), pp. 550–551.
7. O. Voegeli, B. A. Calhoun, L. L. Rosier, and J. C. Slonczewski, "The Use of Bubble Lattices for Information Storage," presented at the 1974 Conf. Magnetism and Magnetic Materials.
8. H. L. Hu, T. J. Beaulieu, D. W. Chapman, D. M. Franich, G. R. Henry, L. L. Rosier, and L. F. Shew, "1K Bit Bubble Lattice Storage Device: Initial Tests," J. Appl. Phys., *49*, No. 3 (March 1978), pp. 1913–1917.
9. E. H. L. J. Dekker, K. L. L. van Mierloo, and R. de Werdt, "Combination of Field and Current Access Magnetic Bubble Circuits," IEEE Trans. on Magnetics, *MAG-13*, No. 5 (September 1977), pp. 1261–1263.
10. J. A. Copeland, J. P. Elward, W. A. Johnson, and J. G. Ruch, "Single-Conductor Magnetic-Bubble Propagation Circuits," J. Appl. Phys., *42*, No. 4 (March 1971), pp. 1266–1267.
11. T. H. O'Dell, *Magnetic Bubbles*, London, England: MacMillan, 1974.
12. W. J. Tabor, A. H. Bobeck, G. P. Vella-Coleiro, and A. Rosencwaig, "A New Type of Cylindrical Magnetic Domain (Hard Bubble)," AIP Conf. Proc., No. 10 (1972), pp. 442–457.
13. J. C. Slonczewski, J. C. Malozemoff, and O. Voegeli, "Statics and Dynamics of Bubbles Containing Bloch Lines," AIP Conf. Proc., No. 10 (1972), pp. 458–477.
14. R. W. Patterson, "Annihilation of Bloch Lines In Hard Bubbles," AIP Conf. Proc., No. 24 (1974), pp. 608–609.
15. H. L. Hu and E. A. Giess, "Hard Bubble Suppression and Controlled State Gener-

ation of One Micron Bubbles in Ion-Implanted Garnet Films," IEEE Transactions on Magnetics, *MAG-11*, No. 5 (September 1975), pp. 1085–1087.
16. V. M. Benrud, G. L. Forslund, M. M. Hanson, R. L. Horst, A. D. Kaske, J. A. Kolling, D. S. Lo, M. J. Nordstrom, H. N. Oredson, W. J. Simon, C. H. Tolman, and E. J. Torok, "Oligatomic Film Memories," J. Appl. Phys., *42*, No. 4 (March 1971), pp. 1364–1373.
17. H. J. Levinstein, S. J. Licht, R. W. Landorf, and S. L. Blank, "Growth of High-Quality Garnet Thin Films from Supercooled Melts," Appl. Phys. Lett., *19*, No. 11 (December 1971), pp. 486–488.
18. S. L. Blank and J. W. Nielsen, "The Growth of Magnetic Garnets by Liquid Phase Epitaxy," J. Crystal Growth, *17* (1972), pp. 302–311.
19. S. L. Blank, J. W. Nielsen, and W. A. Biolsi, "Preparation and Properties of Magnetic Garnet Films Containing Divalent and Tetravalent Ions," J. Electrochem. Soc., *123*, No. 6 (June 1976), pp. 856–863.
20. S. L. Blank, B. S. Hewitt, L. K. Shick, and J. W. Nielsen, "Kinetics of LPE Growth and its Influence on Magnetic Properties," AIP Conf. Proc., No. 10, (1972), pp. 256–270.
21. E. A. Giess, B. E. Argyle, D. C. Cronemeyer, E. Klokholm, T. R. McGuire, D. F. O'Kane, T. S. Plaskett, and V. Sadagopan, "Europium-Yttrium Iron-Gallium Garnet Films Grown by Liquid Phase Epitaxy on Gadolinium Gallium Garnet," AIP Conf. Proc., No. 5, (1971), pp. 110–114.
22. R. L. Barnes, *Advances in X-Ray Analysis*, Vol. 15, K. J. Heinrich, C. F. Barrett, J. D. Newkirk and C. D. Rund, eds., New York: Plenum Press, 1972, pp. 330.
23. R. D. Pierce, "Magnetic Characterization of Bubble Garnet Films in an LPE Growth Facility," J. Crystal Growth, 27 (1974), pp. 299–305.
24. G. P. Vella-Coleiro and W. J. Tabor, "Measurement of Magnetic Bubble Mobility in Epitaxial Garnet Films," Appl. Phys. Lett., *21*, No. 1 (July 1972), pp. 7–8.
25. R. C. LeCraw and R. D. Pierce, "Temperature Dependence of Growth-Induced Magnetic Anisotropy in Epitaxial Garnet Films by Resonance Techniques," AIP Conf. Proc., No. 5, (1971), pp. 200–204.
26. A. H. Bobeck, P. I. Bonyhard, and J. E. Geusic, "Magnetic Bubbles—An Emerging New Memory Technology," Proc. IEEE, *63*, No. 8 (August 1975), pp. 1176–1195.
27. S. L. Blank, R. Wolfe, L. C. Luther, R. C. LeCraw, T. J. Nelson, and W. A. Biolsi, "Design and Development of Single-Layer, Ion-Implantable Small Bubble Materials for Magnetic Bubble Devices," Proc. 24th Annual Conf. on Mag. and Mag. Matl., J. Appl. Phys., March, 1979.
28. M. Kestigian, A. B. Smith, and W. R. Bekebrede, "$(YSmLu)_3(FeGa)_5O_{12}$ for 1 to 3 μm-Diameter Bubble Devices," J. Appl. Phys., *49*, No. 3 (March 1978), pp. 1873–1875.
29. G. P. Vella-Coleiro, F. B. Hagedorn, S. L. Blank, and L. C. Luther, "Coercivity in 1.7-μm Bubble Garnet Films," Proc. 24th Annual Conf. on Mag. and Mag. Matl., J. Appl. Phys., March, 1979.
30. E. R. Czerlinsky and W. G. Field, "Magnetic Properties of Ferromagnetic Garnet Single Crystals," Solid State Phys. Electronics Telecommuns., Proc. Intern. Conf., Brussels, *3* (1958) (Pub. 1960), pp. 488–499.
31. W. A. Johnson, private communication.
32. A. K. Sinha, and T. T. Sheng, "The Temperature Dependence of Stresses in Aluminum Films on Oxidized Silicon Substrates," Thin Solid Films, *48*, No. 2 (February 1978), pp. 117–126.
33. B. J. Roman, private communication.
34. D. K. Rose, "Planar Processing for Magnetic Bubble Devices," IEEE Trans. on Magnetics, *MAG-12*, No. 6 (November 1976), pp. 618–621.
35. C. J. Mogab, and W. R. Harshbarger, "Plasma Processes Set to Etch Finer Lines with Less Undercutting," Electronics (August 31, 1978), pp. 117–121.
36. C. M. Melliar-Smith and C. J. Mogab, in *Thin Film Processes*, J. L. Vossen and W. Kern, eds., New York: Academic Press, 1978, pp. 497–555.
37. H. J. Levinstein, D. N. Wang, Patent Pending.
38. C. J. Mogab and F. B. Alexander, private communication.
39. R. M. Goldstein and J. A. Copeland, "Permalloy Rail-Cylindrical Magnetic Domain Systems," J. Appl. Phys. *42*, No. 6 (May 1971), pp. 2361–2367.
40. R. M. Goldstein, M. Shoji, and J. A. Copeland, "Bubble Forces in Cylindrical Magnetic Domain Systems," J. Appl. Phys., *44*, No. 11 (November 1973), pp. 5090–5095.
41. D. E. Gray, Ed., *American Institute of Physics Handbook*, New York: MacMillan, 1963, p. 5–26.
42. H. B. Dwight, *Tables of Integrals and Other Mathematical Data*, fourth ed., New York: MacMillan, 1961, pp. 12–13.

43. L. M. Milne-Thomson, *Theoretical Hydrodynamics*, fifth ed., New York: MacMillan, 1968, p. 158.
44. I. S. Gradshteyn and I. M. Ryzhik, *Table of Integrals, Series, and Products*, New York: Academic Press, 1965, pp. 81–85.
45. J. L. Blue, "Automatic Numerical Quadrature," B.S.T.J., *56*, No. 9 (November 1977), pp. 1651–1678.
46. H. W. Richmond, "On the Electrostatic Field of a Plane or Circular Grating Formed of Thick Rounded Bars," Proc. London Math. Soc., *22* (April 1923), pp. 389–403.
47. A. A. Thiele, "Device Implications of the Theory of Cylindrical Magnetic Domains," B.S.T.J., *50*, No. 3 (March 1971), pp. 725–773.
48. T. Hsu, "Control of Domain Wall States for Bubble Lattice Devices," AIP Conf. Proc. No. 24, 1974, pp. 624–626.
49. Yoichi Okabe, "A Model to Predict the Upper Cap-Switch Field of Various Capping Layers," IEEE Trans. on Magnetics, *MAG-14*, No. 5 (September 1978), pp. 602–604.